Numerical Simulation of CO$_2$ Sequestration in Geological Formations

Von der Fakultät Bau- und Umweltingenieurwissenschaften der Universität Stuttgart
zur Erlangung der Würde eines Doktors der
Ingenieurwissenschaften (Dr.-Ing.) genehmigte Abhandlung

Vorgelegt von

Andreas Bielinski

aus Burgdorf

Hauptberichter:	Prof. Dr.-Ing. R. Helmig
Mitberichter:	Prof. Dr.-Ing. H. Hasse
	Prof. A. Cunningham
Tag der mündlichen Prüfung:	20.2.2006

Institut für Wasserbau der Universität Stuttgart

2007

Heft 155   Numerical Simulation
of CO_2 Sequestration
in Geological Formations

von
Dr.-Ing.
Andreas Bielinski

D93   **Numerical Simulation of CO$_2$ Sequestration in Geological Formations**

Danksagung

An dieser Stelle möchte ich mich bei zahlreichen Personen bedanken, die bei der Entstehung dieser Arbeit mitgewirkt haben. Zuerst gebührt mein Dank meinem Hauptberichter Prof. Rainer Helmig, der mir große Freiheiten gegeben hat und der immer zur Stelle war, wenn es schwierig wurde. Er hatte großen Anteil daran, dass ich immer gerne zur Arbeit ging und mit Freude bei der Sache war.

Für die Übernahme des Mitberichts möchte ich Herrn Prof. Hasse danken. Gemeinsam mit Herrn Dr. Vrabec war er das "thermodynamische Gewissen" dieser Arbeit und beeindruckte mich sowohl durch viele praktische Hilfestellungen als auch durch den offenen und freundlichen Umgang, der mir die vielen Fragen erleichterte. Vielen Dank an Prof. Al Cunningham für den zweiten Mitbericht und für die Einladung nach Montana im November 2005.

Herrn Prof. Wagner von der Universität Bochum danke ich für die Software zur Berechnung der CO_2 Stoffeigenschaften und Herrn Dr. Spindler von der Universität Stuttgart für seine Unterstützung bei der Erarbeitung der thermodynamischen Grundlagen, die ich für die Erfassung jener Eigenschaften benötigte. Diese beiden stehen stellvertretend für die vielen positiven Erfahrungen, die ich im deutschen Universitätssystem machen konnte.

Bei Prof. Helge Dahle möchte ich mich für die Einladung nach Bergen bedanken. Die 4 Wochen, die ich im Frühjahr 2004 dort verbringen durfte, sollten der Anfang einer längerfristigen Beziehung zu Norwegen werden.

Herzlicher Dank geht an meine Kollegen am Institut für Wasserbau. Es war jeden Tag schön, so viele nette Menschen um sich zu haben. Besonders erwähnen möchte ich hier die Kollegen, zu denen mein Verhältnis weit über das Berufliche hinausging: Steffen Ochs (Kaffee?), Holger Class (Fahrer mit Daimler), Ulrich Ölmann (Langelsheim!), Sabine Manthey (Projekt Promotion), Pru Lawday (Frühstück um 7?) sowie die Laufgruppe (Volker Schrenk, Jürgen Brommundt, Jenny Niessner). Spezieller Dank geht auch an meine Nachfolger im CO_2-Business, Anozie Ebigbo (Doppelzimmer mit TV!) und Andreas "Lybke" Kopp.

Gern möchte ich mich bei meinen ehemaligen Mitbewohnern Chris Walther und Oscar Pozos bedanken, mit denen ich zwei tolle WG-Jahre verbrachte und die mich immer auf andere Gedanken brachten, wenn es mit der Promo mal nicht lief. Meinem guten Studienfreund Jens Warsen vielen Dank für die tägliche Aufmunterung per E-Mail.

Vielen herzlichen Dank an meine Eltern, Ihr habt mich immer toll unterstützt und ohne Euch hätte ich es keinesfalls so weit geschafft.

Schließlich geht noch ein besonderer Dank an Jantje Samtleben: danke, dass Du Ina mit zu meiner Promofeier gebracht hast.

Contents

List of Figures

VIII

List of Tables

Nomenclature

symbol	meaning	dimension
A	surface area	[m^2]
B_i	box that belongs to node i	
D	diffusion coefficient	[m^2/s]
E_{sys}	extensive fluid property	
$\mathbf{F}$	flux term	
$\mathbf{F(x)}$	set of equations with vector of primary variables $\mathbf{x}$	
$\mathbf{J}$	Jacobian matrix	
J	diffusive flux	[kg/(m^2 s)]
$\mathbf{K}$	tensor of absolute (intrinsic) permeability	[m^2]
$\mathbf{K_f}$	tensor of hydraulic conductivity	[m/s]
H	Henry coefficient	[Pa]
M	molecular weight	[kg/mol]
N_j	basis function at node j	
Q	heat	[J]
$\dot{Q}$	heat flux	[J/s]
R	universal gas constant, $R = 8.314$	[J/(mol K)]
S_α	saturation of phase α	[-]
S	salinity (mass fraction of salt in the brine phase)	[kg/kg]
T	temperature	[K]
T^C	temperature in degrees Celsius	[°C]
V	volume	[m^3]
W	work	[J]
$\dot{W}$	work per time unit (power)	[J/s]
W_i	weighting function at node i	
X	mass fraction	[kg/kg]
Z	real gas factor	[-]
a	parameter for cubic equation of state	[-]
b	parameter for cubic equation of state	[m^3/mol]
c_s	specific heat capacity of the porous medium	[J/(kg K)]
f	fugacity	[Pa]
$\mathbf{g}$	gravitational acceleration vector $(0,0,\text{-g})^{\mathrm{T}}$	[m/s^2]
g	gravity constant (g=9.81)	[m/s^2]
h	specific enthalpy	[J/kg]

Δh_L	heat of dissolution, enthalpy change due to dissolution	[J/kg]
$k_{r\alpha}$	relative permeability of phase α	[-]
m	mass	[kg]
n	number of moles	[mol]
n_{VG}	Van-Genuchten parameter	[-]
$\mathbf{p}$	momentum	[kg m/s]
p	pressure	[Pa]
p_α	pressure of phase α	[Pa]
p_α^K	partial pressure of component K in phase α	[Pa]
p_{wsat}	saturation vapor pressure of water	[Pa]
q	source/sink	[kg/s, J/s]
q_{CO2}	CO_2 mass flux	[kg/s]
$\dot{q}_{\mathrm{h}}$	heat flux density	[J/(m^2 s)]
$\dot{q}_{\mathrm{CO2}}$	CO_2 mass flux density	[kg/(m^2 s)]
r	radius	[m]
s	length	[m]
t	time	[s]
u	specific internal energy	[J/mol, J/kg]
u	unknown variable	
$\mathbf{v}$	Darcy velocity vector	[m/s]
$\mathbf{v_a}$	seepage velocity vector	[m/s]
v	typical flow velocity	[m/s]
v	molar volume	[m^3/mol]
x	mole fraction	[mol/mol]
z	z-coordinate, depth	[m]
Ψ_α	total potential of phase α	[Pa]
α_{VG}	Van-Genuchten parameter α	[Pa^{-1}]
ε	intensive fluid property	
λ	heat conductivity	[J/(m s K)]
μ	dynamic viscosity	[Pa s]
ν	kinematic viscosity	[m^2/s]
ϕ	porosity	[-]
ϱ	mass density	[kg/m^3]
ϱ^{mol}	molar density	[mol/m^3]
σ	surface tension	[N/m]
τ	tortuosity	[-]
ω	acentric factor	[-]

subscripts

CO2	CO_2-rich phase
b	brine phase
crit	critical, at critical point
mix	referring to a mixture of substances
pm	porous medium
r	reduced dimension
s	solid phase
w	water-rich phase
α, β	refering to phases α, β

superscripts

CO2	CO_2 component
w	water component
i	component i
C	component

Abstract

CO_2 sequestration in geological formations is regarded as a measure for reducing the emissions of this greenhouse gas into the atmosphere. With this method, carbon dioxide is captured at large point sources, e.g. coal-fired power plants, and injected into subsurface reservoirs for long-term storage. Such formations can be exploited gas or oil reservoirs or saline aquifers. The latter have the advantage that they are abundant in many places and provide large storage volumes.

In this study, the topic of CO_2 sequestration in saline aquifers is addressed using numerical methods. A model concept is developed, taking into account a CO_2-rich phase, a brine phase and the rock matrix as a rigid porous medium. The focus is on the correct description of the fluid properties including super- and subcritical properties of the CO_2-rich phase. Mutual dissolution of the components in the phases and the effect of the salt content in the aqueous phase on dissolution behavior and fluid properties are considered. Non-isothermal effects are taken into account. Advective and diffusive flow processes are included into the model concept. Multi-phase behavior is considered using relative permeability and capillary pressure functions. The set-up of the mathematical model and its numerical implementation in the numerical simulator MUFTE-UG are described in detail.

Various simulations show the capability of the developed model and give insight into principle processes that occur during CO_2 sequestration in geological formations. The short-term carbon dioxide plume propagation during the injection process is investigated. The long-term behavior is studied in another example considering the dissolution of a CO_2 plume in the subsurface over a period of 100 years. Furthermore, non-isothermal processes are investigated in a simulation example.

This work provides a tool which is capable of reproducing and predicting many of the processes that occur during CO_2 sequestration in geological formations. It can be used for principle studies as well as for the field cases that this technology is going to be applied to. It provides the foundation for further extensive research into many open questions to be addressed in the future.

Deutsche Zusammenfassung

Die Erwärmung des Weltklimas aufgrund der Emission verschiedener Treibhausgase ist ein Thema, das zur Zeit in Wissenschaft und Politik stark diskutiert wird. Eine große Mehrheit der Wissenschaftler, die auf diesem Gebiet arbeiten, ist der Ansicht, dass eine anthropogene Beeinflussung des globalen Klimas zu beobachten ist. Obwohl die Vorhersagen für den mittleren Temperaturanstieg stark variieren, ist eine Zunahme von lokalen Extremereignissen wie Dürren oder Stürmen sehr wahrscheinlich. Darüberhinaus würden höhere Temperaturen zu einem Abschmelzen der Gletscher und Polkappen und damit zu einem Anstieg des Meeresspiegels führen. Die damit verbundenen Schwierigkeiten für viele Küstengebiete und Länder, die teilweise unter dem Meeresspiegel liegen, sind offensichtlich. Aus diesen Gründen wird nach Mitteln und Wegen gesucht, die Emission von Treibhausgasen in die Atmosphäre zu reduzieren und damit dem Treibhauseffekt entgegenzuwirken.

Die wichtigsten Treibhausgase, die durch menschliche Aktivitäten entstehen, sind Kohlendioxid (CO_2), Methan (CH_4) und Lachgas (N_2O). Das CO_2 spielt dabei die wichtigste Rolle, da es bei jedem Verbrennungsprozess entsteht und in den mit Abstand größten Mengen in die Atmosphäre entlassen wird. Eine Möglichkeit, die zur Zeit zur Reduzierung der CO_2-Emissionen in Betracht gezogen wird, ist dessen langfristige Speicherung in geologischen Formationen. Die Idee ist eine Abtrennung des Kohlendioxids aus den Abgasen großer Emittenten (z.B. Kohlekraftwerke) und die Verbringung in geeigneten geologischen Schichten in großer Tiefe. Solche Formationen können ausgeförderte Erdöl- und Erdgasfelder sowie tiefgelegene wasserführende Schichten mit großem Hohlraumanteil (Aquifere) sein.

Das Prinzip der CO_2-Verbringung in geologischen Formationen (englisch: CO_2 sequestration) kann wie folgt beschrieben werden (vgl. Abb. 1.3): das Kohlendioxid wird nach der Abtrennung aus den Abgasen durch eine Rohrleitung in einer Bohrung in eine Tiefe von zirka 1000 m unter der Erdoberfläche gepumpt. Dort wird es in die Formation injiziert und beginnt sich auszubreiten. Obwohl sich das CO_2 unter den gegebenen Drücken und Temperaturen im überkritischen Zustand befindet und damit eine hohe Dichte aufweist, ist es leichter als das die Poren des Gesteins füllende salzhaltige Formationswasser und steigt auf. Aus diesem Grund muss oberhalb der Speicherformation eine gering durchlässige Schicht liegen, die für das CO_2 eine Migrationsbarriere darstellt (Cap-Rock). Sollte die niederpermeable Schicht versagen, kann das Kohlendioxid diese passieren und bis in geringere Tiefen aufsteigen. Dort wird es aufgrund abnehmender Druck- und Temperaturverhältnisse möglicherweise in den flüssigen, schließlich jedoch in den gasförmigen Zustand übergehen. Die damit verbundene Volumenzunahme (Dichteabnahme) führt zu einer erhöhten Aufstiegsgeschwindigkeit und letztlich dem Erreichen der Erdoberfläche und damit der Atmosphäre.

Wenn eine intakte Migrationsbarriere den vertikalen CO_2-Aufstieg behindert, kommt es zu einer Ausbreitung des Kohlendioxids innerhalb der Speicherformation. Verschiedene Speichermechanismen sorgen für einen langfristigen Verbleib des Treibhausgases in der geologischen Schicht. Wichtig ist dabei zum Beispiel die Unterscheidung zwischen der kurzfristigen Ausbreitung des Kohlendioxids als eigene Phase und der langfristigen Lösung des CO_2 im Formationswasser des Speichergesteins.

Ziel dieser Arbeit

In dieser Arbeit soll ein physikalisch-mathematisches Modell erstellt werden, das die bei der CO_2-Speicherung in geologischen Formationen ablaufenden Strömungs- und Transportprozesse beschreibt. Aufgrund der hohen Komplexität der auftretenden Prozesse ist die numerische Umsetzung des Modellkonzeptes erforderlich. Ein wichtiges Teilziel ist die Berücksichtigung der Bedingungen in Tiefen möglicher Speicherformationen bis hinauf zur Erdoberfläche.

Physikalisch-mathematisches Modellkonzept

Das in dieser Arbeit entwickelte Modellkonzept berücksichtigt die Strömungs- und Transportprozesse einer CO_2-reichen und einer wässrigen Phase mit hohem Salzgehalt (Formationswasser). Die beiden Phasen bewegen sich in einem porösen Medium, dem Gestein, das über seine Porosität und Permeabilität erfasst wird. Die Gesteinsmatrix ist starr, ihre Eigenschaften verändern sich nicht aufgrund von Druck-, Temperatur- oder Sättigungsänderungen. Die Interaktion zwischen dem porösen Medium und den Fluiden wird über Kapillardruck-Sättigungsbeziehungen sowie über Relative Permeabilität-Sättigungsbeziehungen berücksichtigt.

Die beiden Fluidphasen setzen sich jeweils aus den Komponenten CO_2 und Wasser sowie aus einem Salzanteil in der wässrigen Phase zusammen. Die Anteile der Komponenten in den Phasen werden über eine Gleichgewichtsbetrachtung mit Hilfe einer Zustandsgleichung ermittelt. Druck und Temperatur sind für die gelösten Konzentrationen entscheidend. Darüberhinaus wird die Reduzierung des gelösten Kohlendioxids aufgrund des Salzgehalts im Formationswasser erfasst. Bei Unterschreiten der maximalen Löslichkeit einer Komponente kommt es zur Auflösung einer Phase und damit zu der Betrachtung eines Einphasen Strömungs- und Transportproblems.

Die für die Berechnung der Phasenbewegung im porösen Medium notwendigen Eigenschaften sind die Dichte und die Viskosität der Fluide. Darüberhinaus wird für die Betrachtung der nicht-isothermen Prozesse die Enthalpie erforderlich. Diese Fluideigenschaften hängen

wesentlich von den Druck- und Temperaturbedingungen im Untergrund ab. Während die CO_2-reiche Phase als Reinstoff betrachtet wird, hängen die Eigenschaften der wässrigen Phase auch von dem Anteil des gelösten Kohlendioxids sowie von der Salzkonzentration ab. Dies ist wichtig, da die Formationswässer in großen Tiefen häufig sehr große Salzgehalte aufweisen, so dass vor allem die Dichte stark von der reinen Wassers abweicht.

Mathematisches Modell und numerische Implementierung

Das mathematische Modell beinhaltet die Speicherung von Masse im porösen Medium und die advektiven Strömungsprozesse der Phasen aufgrund von Druck- und Auftriebskräften. Sie werden über das für Mehrphasenflüsse erweiterte Darcygesetz beschrieben. Diffusiver Transport von gelöstem CO_2 wird über einen Fickschen Ansatz berücksichtigt. Energie wird sowohl in den Fluidphasen als auch in der Gesteinsmatrix gespeichert und fließt durch Wärmeleitung oder mit den sich bewegenden Phasen.

Die Formulierung des mathematischen Problems erfolgt über zwei Massenbilanzgleichungen für die Komponenten CO_2 und Wasser sowie über eine Energiebilanzgleichung. Die Gleichungen ergeben ein stark nichtlineares System von gekoppelten Differentialgleichungen.

Die Lösung dieses mathematischen Problems erfordert die Anwendung numerischer Methoden. Eine vollimplizite Zeitdiskretisierung wird verwendet. Für die räumliche Diskretisierung wird das BOX-Verfahren angewendet, das die Vorteile einer Finite Volumen-Methode (lokale Massenkonservativität) mit der eines Finite Elemente-Verfahrens (unstrukturierte Gitter) verbindet. Eine Newton-Raphson-Methode wird für die Linearisierung des resultierenden nichtlinearen Gleichungssystems verwendet, die Lösung des anschließenden linearen Problems erfolgt meist mit einem iterativen Löser. Für die numerische Umsetzung der beschriebenen Gleichungen wird das numerische Simulationsprogramm MUFTE-UG (**MU**ltiphase **F**low **T**ransport and **E**nergy Model on **U**nstructured **G**rids) genutzt.

Prinzipbeispiele und Simulationsergebnisse

Die Leistungsfähigkeit des vorliegenden Simulationsprogramms wird anhand mehrerer Prinzipbeispiele demonstriert. Die radialsymmetrische Ausbreitung der CO_2-reichen Phase in der Speicherformation und der Einfluss niederdurchlässiger Schichten auf den Aufstieg des Kohlendioxids werden in einem Simulationsbeispiel untersucht. Der hier betrachtete Zeitrahmen bezieht sich auf die ungefähre Dauer der CO_2-Injektion in die Formation, d.h. auf eine Dauer von Monaten bis Jahren.

Ein anderes Beispiel bezieht sich auf die langfristige Speicherung des CO_2 im Untergrund: wenige Jahre nach dem Ende der Injektion in die Formation kommt die Bewegung der

kohlendioxid-reichen Phase an den meisten Stellen des Reservoirs zum Stillstand. Das CO_2 kann dann nur noch durch Lösung im Formationswasser und Diffusion transportiert werden, so dass sich das Kohlendioxid als Phase langsam auflöst. Da gelöstes CO_2 die Dichte einer wässrigen Lösung erhöht, kommt es zu einem Absinken des CO_2-gesättigten Formationswassers. Dieses Absinken erfolgt in Fingern, deren Bildung von mehreren Faktoren abhängen. So beeinflusst im Modell auch die räumliche Diskretisierung des Problemgebietes die Bildung von Fingern und damit das Absinken und den Auflösungsprozess des CO_2 in Phase. Ein weiteres Prinzipbeispiel verdeutlicht diese Abhängigkeit der Fingerbildung von der Diskretisierung.

Die nicht-isothermen Effekte aufgrund von Expansion (Joule-Thomson Effekt) und Verdampfung des CO_2 werden in einem weiteren Beispiel gezeigt. Es wird deutlich, dass für das gewählte Beispiel diese Effekte innerhalb eines Reservoirs keine besonders große Rolle spielen, sondern nur eine Veränderung der Temperaturen von wenigen Grad Celsius bewirken.

Zusammenfassende Schlussfolgerungen

In der vorliegenden Arbeit wird ein physikalisch-mathematisches Modellkonzept zur Beschreibung von CO_2-Speicherung in tiefen geologischen Formationen entwickelt und in einem numerischen Simulationsprogramm umgesetzt. Der gewählte Zweiphasen-Zweikomponenten-Ansatz ermöglicht die Beschreibung nicht-isothermer Strömungs- und Transportprozesse der CO_2-reichen Phase und des salzhaltigen Formationswassers in dem Gestein der Speicherformation. Ausgewählte Beispiele zeigen die Leistungsfähigkeit des Programms bezüglich der CO_2-Speicherung auf unterschiedlich langen Zeitskalen sowie nicht-isothermer Effekte.

Das vorgestellte Programm ermöglicht eine umfassende Betrachtung der Strömungs- und Transportprozesse von CO_2 in einer Speicherformation. Es stellt die Grundlage für weitergehende Untersuchungen bezüglich des Verhaltens von Kohlendioxids im Untergrund dar. Offene Fragen sind in diesem Zusammenhang Themen wie viskoses Fingering während des CO_2-Injektionsprozesses, das Eintrittsverhalten in eine niederpermeable Deckschicht oder nicht-isotherme Effekte bei einem weitreichenden Aufstieg durch eine Kluft. Darüberhinaus ist das Programm für praktische Fragestellungen hinsichtlich CO_2-Speicherung in Gesteinen anwendbar. Langfristige Speicherkapazitäten spezieller Reservoire, die Temperaturänderungen in der Speicherformation bei unterschiedlichen Temperaturen des CO_2 am Injektionspunkt (und das Nutzen der Temperatur im Reservoir zum Monitoring) oder der Einfluss unterschiedlicher Permeabilitätsverteilungen auf die Ausbreitung des Kohlendioxids stellen solche Fragestellungen dar.

Chapter 1

Introduction

The global climate is a highly complex system that depends on many parameters and has been subject to various changes within geological times. During the last decades, a trend of rising average global temperature has been observed. Increasingly scientists are connecting rising temperatures with increasing amounts of greenhouse gases in the atmosphere. These gases absorb part of the long-wave heat radiation emitted from the surface of the earth and can therefore cause a heating-up of the atmosphere (e.g. HOUGHTON (1997) [54]).

Greenhouse gases, mainly water vapor, carbon dioxide (CO_2), methane (CH_4), and laughing gas (N_2O), reside naturally in the atmosphere. Due to human activities, the amounts of the latter three have been increasing since the beginning of the industrial revolution. Table 1.1 lists the most important anthropogenic greenhouse gases, their estimated annual emissions, and their global warming potential (GWP). The GWP takes into account the climate efficacy of greenhouse gases and their residence time in the atmosphere with respect to CO_2.

Table 1.1: Annual emissions of greenhouse gases (data taken from BUNDESUMWELTAMT (2001) [99]).

gas	annual emissions [Mt/a]	GWP
CO_2	22,000	1
CH_4	375	21
N_2O	4.7-12.6	310

Carbon dioxide is the most important greenhouse gas, because it is emitted into the atmosphere in large quantities. Figure 1.1 shows the global carbon cycle containing the various sub-systems where carbon can be stored:

- atmosphere,

- ocean,

- soil, vegetation,

- fossil fuels.

The fluxes between the sub-systems are also indicated, e.g. CO_2 take-up by vegetation from the atmosphere or carbon dioxide emissions from the combustion of fossil fuels. Summing up the fluxes results in an accumulation of carbon in the atmosphere. The fluxes between the sub-systems are variable, e.g. a higher atmospheric CO_2 concentration yields higher take-up by oceans and plants. However, a net CO_2 accumulation in the atmosphere is observed.

Masses in Gt, fluxes in Gt/a; after J. Houghton, "Global warming" (1997)
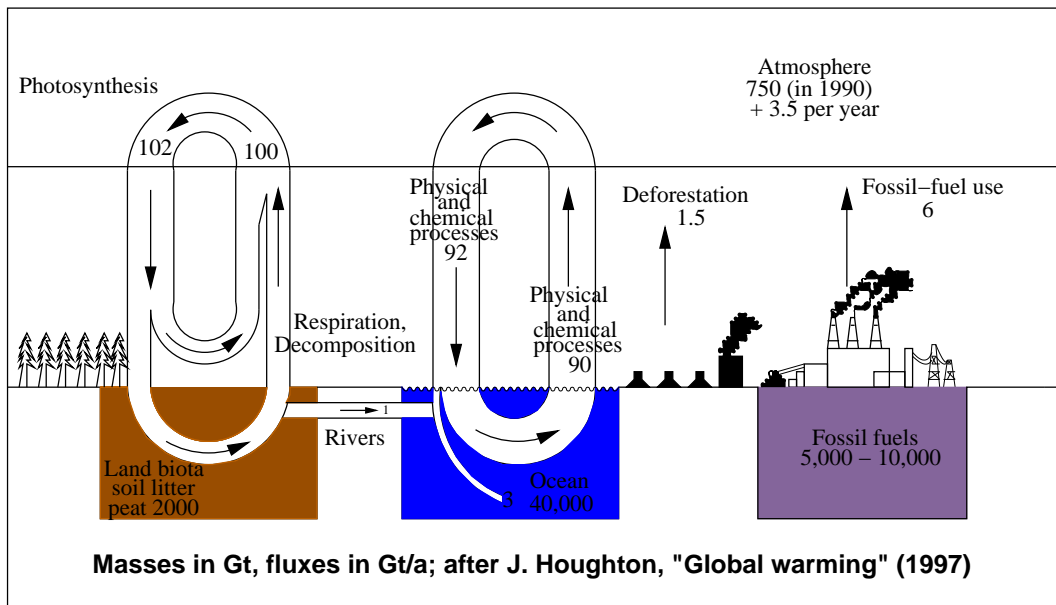
Figure 1.1: Global carbon cycle. Carbon is distributed in the compartments atmosphere, land, ocean, and fossil fuels. Various processes lead to mass fluxes between the compartments. Masses are given in Gt carbon and mass fluxes in Gt carbon/year.

Before the beginning of industrialization, the average global concentration of CO_2 in the atmosphere was 280 ppm (parts per million, μmol CO_2/mol air). In the year 2000, the concentration reached about 370 ppm. The steadily increasing amount of CO_2 in the atmosphere is illustrated in Figure 1.2 [63]. It shows the carbon dioxide concentrations measured in Mauna Loa, Hawaii, from 1958 to 2005. Apart from seasonal changes, the long-term trend of increasing CO_2 concentration can be clearly seen.
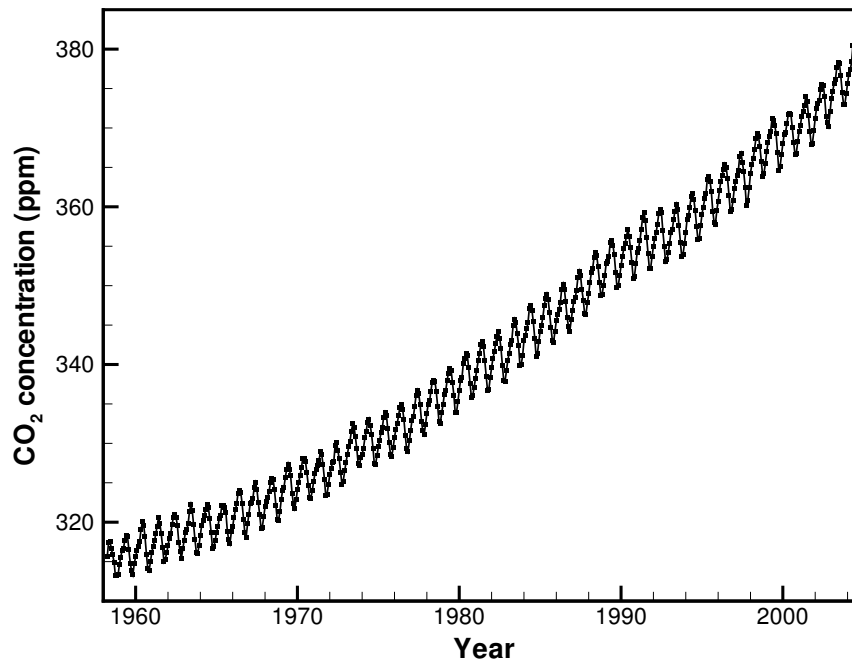
Figure 1.2: Monthly average carbon dioxide concentration at Mauna Loa Observatory, Hawaii, from 1958 to 2005 [63].

Several scenarios describing the emission of greenhouse gases and models for the estimation of their influence on the global climate have been examined by the members of the Intergovernmental Panel on Climate Change (IPCC). Depending on the assumptions and the climate model global temperature increases between 1 and 6 °C were predicted by the year 2100 (IPCC (2001) [59]). While some regions might benefit from higher temperatures (e.g. a longer growing season), it is very likely that others could face dramatic problems as a result of changed local climate. A rise in sea level (with obvious problems for countries lying partly below sea level such as Bangladesh or the Netherlands) and greater frequency of extreme local weather events (storms, floods, droughts) are two major effects mentioned here. For these reasons, a reduction of greenhouse gas emissions is highly desirable.

As mentioned above, CO_2 is the most important climate-effective gas as it is emitted in large amounts. Another reason for considering the reduction of this particular gas is the advantage that CO_2 is mainly emitted by point sources (power plants, industrial sites). In contrast to this, methane and laughing gas are mostly produced in agriculture (paddy-fields, cattle breeding, nitrogen fertilization) and therefore reach the atmosphere very diffusely.

Some possible ways of decreasing CO_2 emissions are the following:

- Improving the energy efficiency of existing technologies: the use of less energy (fossil

3

fuel) for the same output diminishes emitted CO_2 (e.g. cars, power plants).

- Using alternative energy sources: wind, solar and hydropower do not produce CO_2 emissions. Biomass/wood as a fuel emits only the amount of carbon dioxide that was extracted from the atmosphere in the first place; it is emission neutral.

- Capturing CO_2 and storing it for long periods of time (hundreds of years) in geological formations.

This work addresses the latter possibility, the long-term storage of CO_2 in geological formations (CO_2 sequestration), in particular aquifers.

1.1 Principle of CO_2 sequestration

Figure 1.3 illustrates the possible behavior of injected CO_2 in a brine aquifer. Carbon dioxide is captured from a point source, e.g., a power plant, and piped into a depth of approximately 1000 m below the surface of the earth. The CO_2 injection should take place at a depth of at least 750-800 m to ensure that the carbon dioxide enters the formation in supercritical or liquid state of aggregation. The maximum injection depth is usually dictated by economic considerations: the deeper the injection, the higher the drilling costs. The CO_2 enters the storage formation. At pressure and temperature conditions there, the carbon dioxide is supercritical, i.e. it has a very high density compared with gaseous CO_2. Nevertheless, the density of the saline formation fluid (brine) is higher, causing the CO_2 to migrate upwards. For this reason, it is necessary to have a confining layer above the storage formation to stop the CO_2 from this upward migration. This layer, usually called cap-rock, needs to have a significantly lower permeability than the storage formation. Moreover, it should not have open fractures or faults which might provide vertical pathways for the carbon dioxide.

If the CO_2 migrates through the cap-rock it will rise further towards the surface and finally encounter conditions in which it will turn into gaseous CO_2 (cf. Figure 1.3). Then, the density difference to the resident brine is much higher and the gaseous CO_2 will reach the surface of the earth quickly.

The storage formation for long-term CO_2 sequestration should have a large amount of available pore space and, as mentioned above, a sealing cap-rock. Geological formations that may fulfill these prerequisites are:

- exploited oil or gas reservoirs,
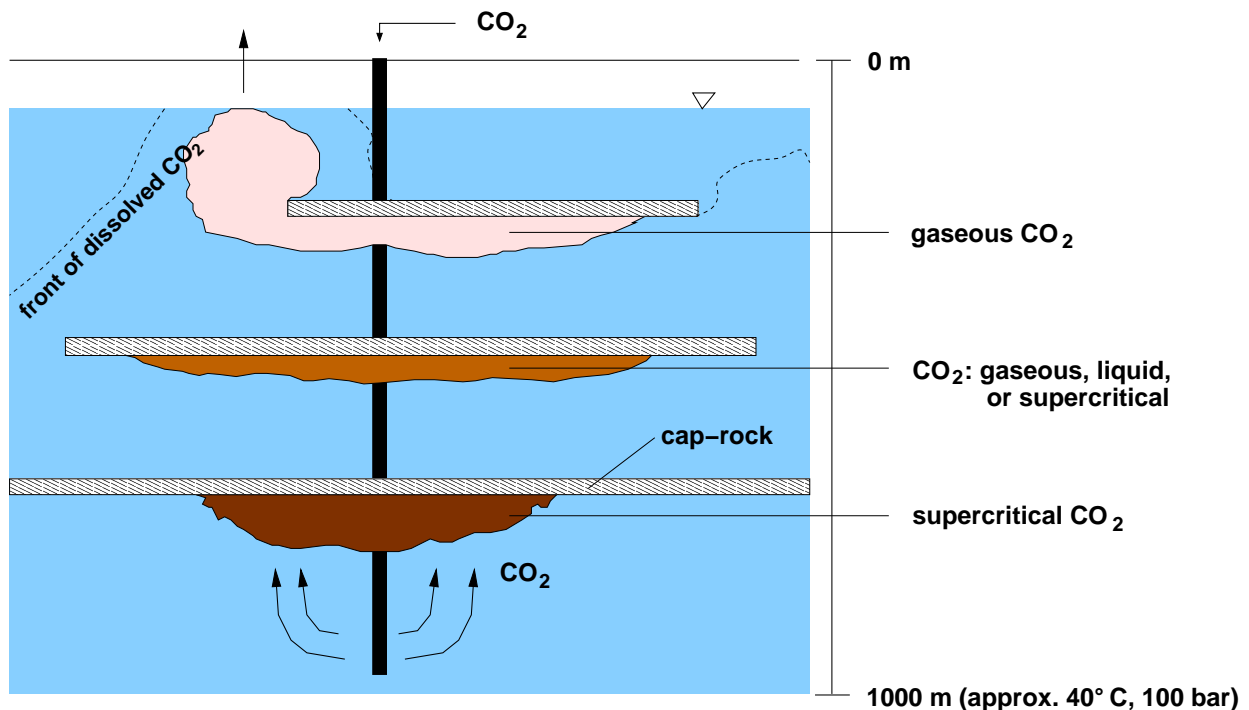
Figure 1.3: Principle of CO_2 sequestration in geological formations. Carbon dioxide is injected into the storage formation at a depth of approximately $1000\,$m. Here, the CO_2 has a lower density than the surrounding brine and rises until it hits a low-permeable layer (cap-rock). If it passes through the cap-rock, the CO_2 will migrate further upwards and reach the atmosphere.

- brine aquifers.

Oil and gas reservoirs are favorable, because they have proven to store fluids for very long periods of time due to their geological structure. Furthermore, CO_2 injection can help to recover remaining oil and gas from the reservoir (EOR/EGR: Enhanced Oil/Gas Recovery).

Deep brine aquifers with a confining layer that serves as a cap-rock exist in many places. Their storage capacities are significantly higher than those of oil and gas reservoirs and they are more likely to be found close to large CO_2 point sources. However, aquifers are usually less well-known and thus, the risk of encountering unknown faults or fractures is higher than in oil and gas reservoirs that have been previously exploited.

When carbon dioxide is sequestered in a geological formation, various trapping mechanisms may lead to a secure long-term storage:

- **Hydrodynamic trapping:** as explained above, the cap-rock prevents the CO_2 from rising upwards, because it is of low permeability. This leads to the storage mechanism

5

called hydrodynamic trapping. Note that the cap-rock should lie horizontally or even form a dome to ensure that the CO_2 cannot escape laterally.

- **Residual fluid trapping:** Migrating in the subsurface, the CO_2 plume leaves a trace of residual saturation, i.e. a certain part of the pore volume is filled with CO_2 that no longer moves (cf. Section 2.6.4). Therefore, CO_2 that is stored by residual fluid trapping will stay in the formation for long periods of time.

- **Solubility trapping:** As the carbon dioxide flows in the subsurface, it dissolves in the brine which initially fills the pores of the storage formation. Dissolved CO_2 mass does not flow upwards because of density differences. It can stay in the formation fluid for long periods of time.

- **Mineral trapping:** Depending on the properties of brine and rock, the CO_2 reacts with the formation and forms minerals. Most of these geochemical reactions take place slowly within a time frame of decades and centuries. If minerals have formed and the system CO_2-brine-rock has equilibrated, CO_2 is bound for long periods of time in mineral trapping.

Figure 1.4 gives a quantitative idea of the trapping mechanisms and their predominance at various times of the sequestration process. Hydrodynamic trapping is the most important trapping mechanism while CO_2 is being injected into the formation and as long as the plume is moving in the subsurface. With time the plume stagnates and residual and solubility trapping become the predominant CO_2 traps. After at least several hundreds of years, mineral trapping may become the most important trapping mechanism. Note that the length of the bars in Figure 1.4 strongly depends on the injected amount of CO_2 in the formation, the injection time, the geological structure, and the geochemical characteristics of the storage formation.

1.2 State of the art

Numerical simulation of multi-phase flow in porous media: The first numerical simulators for the computation of multi-phase flow in porous media were developed in the petroleum industry in the 1960s (AZIZ & SETTARI (1979) [11], PEACEMAN (1977) [82]). Since the 1980s numerical multi-phase models are also applied to environmental problems, e.g. the simulation of groundwater remediation technologies in the unsaturated zone (e.g. FALTA ET AL. (1992) [37, 38], PANDAY ET AL. (1995) [81], HELMIG (1997) [52], CLASS ET AL. (2002) [28, 29]).
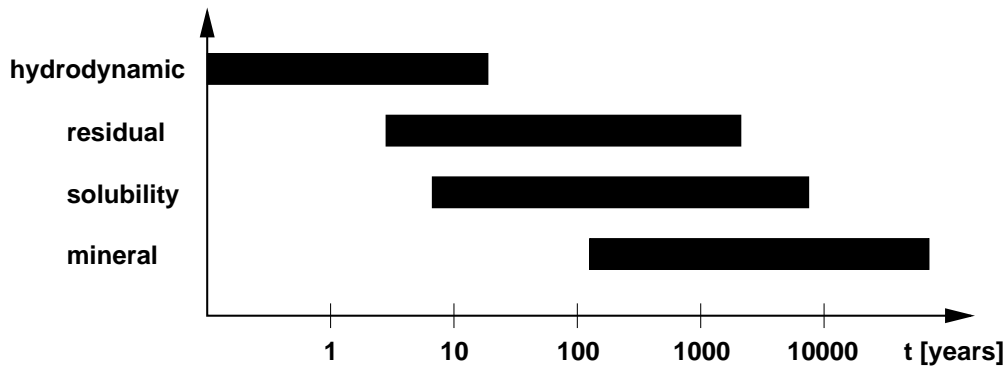
Figure 1.4: Predominant trapping mechanisms and their estimated time scales in CO_2 sequestration.

The numerical simulation of CO_2 sequestration in geological formations is a fairly new research area and has been addressed by e.g. LINDEBERG (1997) [66], PRUESS & GARCIA (2002) [88], and GARCIA (2003) [42]. Code comparison studies have been conducted to compare the model approaches of various work groups (PRUESS ET AL. (2002) [87]).

CO_2 injection into geological formations as a means of enhancing oil or gas recovery has been investigated by e.g. HATTENBACH ET AL. (1998) [47], JESSEN ET AL. (2001) [61], OLDENBURG & BENSON (2002) [80], AGUSTSSON & GRINESTAFF (2004) [9]. Comprehensive reviews about the research on this topic conducted in the petroleum industry can be found in SPE REPRINT SERIES (1999) [93], SPE MONOGRAPH SERIES (2002) [94].

Analytical solutions for CO_2 sequestration: NORDBOTTEN ET AL. [77, 78, 79] have published semi-analytical approaches to the problem of CO_2 propagation in the subsurface taking leaky wells into account.

Modeling of chemical reactions during CO_2 sequestration: The chemical reactions that occur when storing CO_2 in geological formations mostly take place on a much longer time scale than flow and transport (e.g. KASZUBA ET AL. (2003) [62]). Therefore, separate models for the treatment of geochemical reactions have been set up (e.g. the model SHEMAT developed by CLAUSER (2003) [30]). XU ET AL. (2002) [104] have developed the numerical simulator TOUGHREACT, which is capable of coupling geochemical reactions with multiphase flow.

Modeling of non-isothermal effects during CO_2 sequestration: PRUESS (2004) [86] investigated the non-isothermal effects of CO_2 in the subsurface focusing on its leakage in faults, fractures, or abandoned wells.

Geomechanical effects: The injection of the carbon dioxide into a storage reservoir can

7

change the geomechanical conditions in the subsurface and lead to fracturing of the storage formation or the cap-rock. STREIT & HILLIS (2004) [98] have addressed this topic estimating the stability of faults in rocks.

Experimental work in the laboratory: So far, only few publications exist on laboratory experiments on CO_2-brine systems in porous media. BENNION & BACHU (2005) [19] have carried out experimental work on relative permeability-saturation relationships for the system of interest in sandstones and carbonatic rocks.

Natural analogues: The investigation of natural analogues can provide insight into CO_2 migration in geological formations. The NASCENT project considered these issues at several locations in Europe [3]. In Australia, WATSON ET AL. (2003) [102] investigated natural analogues to study possible geomechanical effects of CO_2 sequestration.

Field experiments: The presently best-known field experiment is the Sleipner project. Here, the Norwegian oil company Statoil started injecting CO_2 off-shore into a big sandstone reservoir (the Utsira formation) in 1997 [5]. Since then, 1 million tons of CO_2 per year have been pumped into the aquifer. Several research projects have accompanied this operation scientifically [4].

At the Weyburn site in Canada, an EOR project is being carried out, investigating CO_2 sequestration issues in particular. With high oil prices, this is a very profitable research project [6].

In the CO2SINK project it is planned to sequester CO_2 underneath a former gas storage site. One interesting feature of this field experiment is that carbon dioxide will be stored near to a densely populated area close to Berlin in Germany. Apart from the technical issues, this makes the project interesting with respect to authorization procedures and public outreach [1].

Others: The GESTCO project has investigated possible carbon dioxide storage sites all over Europe [2]. It provides an overview over available storage capacities (CHRISTENSEN & HOLLOWAY (2003) [24]) and a database to link point sources with storage sites (source-sink-matching).

Research work conducted by GASDA ET AL. (2004) [43] investigates the distribution of active and abandoned wells in Texas, U.S.A., and Alberta, Canada. Especially old abandoned wells can be a high risk for CO_2 leakage from its reservoir.

1.3 The numerical simulator MUFTE-UG

MUFTE-UG stands for **MU**ltiphase **F**low **T**ransport and **E**nergy Model on **U**nstructured **G**rids. It has been developed in a cooperation between workgroups at the University of Stuttgart (e.g. HELMIG ET AL. (1998) [51]) and at the University of Heidelberg (e.g. BASTIAN ET AL. (1997) [15]).

Figure 1.5 shows the program package MUFTE-UG. UG is a numerical platform which can be used to solve any kind of partial differential equation. It provides data structures, solvers, grid refinement techniques, and the possibility of parallel computation. The MUFTE part of the simulator is programmed on top of UG and specifies the discretized equations needed for non-isothermal multi-phase multi-component flow. Thus, various discretization methods, problem descriptions, and constitutive relationships can be implemented in MUFTE.
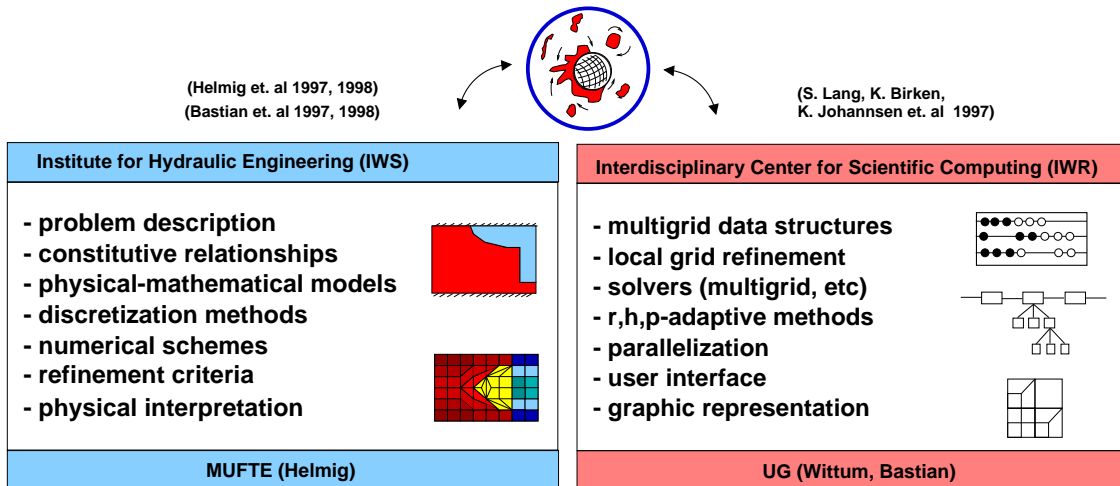
Figure 1.5: The numerical simulator MUFTE-UG.

Modules for several different problem classes have been implemented into MUFTE-UG; some of them are:

- Isothermal two-phase flow, e.g. gas-water systems (e.g. HELMIG & HUBER (1996) [53]).

- Non-isothermal two-phase two-component flow for gas-water systems (e.g. JAKOBS (2004) [60]).

- Isothermal three-phase three-component flow for water-NAPL-gas systems (e.g. HUBER (1999) [56]).

- Non-isothermal three-phase three-component flow for water-NAPL-gas systems (CLASS ET AL. (2002) [28, 29]).

In this work, MUFTE-UG is used to implement the equations and the fluid properties needed for the description of non-isothermal flow of CO_2 and brine in geological formations.

1.4 Structure of this work

Chapter 2 gives definitions and explains thermodynamic and hydrodynamic fundamentals needed for this study. In Chapter 3, this knowledge is applied to the developed model which describes the multi-phase flow of CO_2 and brine in rock formations. A two-phase two-component model concept is chosen which takes into account a water-rich liquid phase and a CO_2-rich phase that can be gaseous, liquid, or supercritical. The constitutive equations for the description of the fluid properties including the compositions of the phases are explained. This conceptual model is put into a mathematical and numerical context in Chapter 4. There, the balance equations for mass and energy are formulated, including advective and diffusive transport processes. The numerical scheme for the solution of the system of non-linear partial differential equations is explained in detail.

Chapter 5 gives example simulations that study the carbon dioxide flow in the subsurface. The various trapping mechanisms which can be addressed by the model are treated in separate examples to point out the model capabilities. Special emphasis is put on the formation of fingers resulting from density differences and the dependence of this phenomenon on the discretization of the numerical model.

Finally, Chapter 6 concludes with a summary of this work and suggestions for future research.

Chapter 2

Fundamentals

2.1 Fundamental terms

2.1.1 Phases, components

A *phase* is a well-defined region where there are no discontinuities in material properties. Two phases are separated by an interface; it is therefore possible to observe several solid or liquid phases at the same time while only one gas phase can be present.

A phase can contain several *components* that relate to chemical substances and can be transferred between the phases.

2.1.2 State variables

The state of a system is characterized by its physical properties. A state variable describes the condition (state) of the system under consideration and is path-independent, i.e. the value of the state variable is independent of how the system has reached its state. State variables often used are temperature and pressure, because they are easily accessible by measurements (e.g. LÜDECKE & LÜDECKE [68]).

In thermodynamics, there is a distinction between extensive and intensive state variables. *Extensive state variables* depend on the size of the system considered, e.g. volume increases with expanding system size. In contrast to this, an *intensive state variable* is independent of the system size, e.g. the temperature. If an extensive state variable is divided by another extensive variable, a specific state variable which is also intensive is obtained. For example, relating volume to mass results in the specific volume which does not depend on the size of the system.

2.1.3 State of aggregation

Any substance can occur in different states of aggregation, namely solid, liquid, and gaseous. Figure 2.1 shows an example of a phase diagram with the states of aggregation depending on temperature T and pressure p conditions. The lines that separate the different states of aggregation are called phase-coexistence lines. They mark the temperatures and pressures where the substance forms two stable phases at the same time, e.g. a gaseous and a liquid phase (vapor pressure curve). The phase diagram also shows two characteristic points that are important for characterizing the behavior of a substance's thermal properties. At the triple point a solid, a liquid and a gaseous phase occur at the same time. The critical point is the upper end of the vapor pressure curve. If temperature and pressure are above the critical point the fluid is in a *supercritical state*.

Note that if only one state variable of temperature or pressure exceeds the critical point it is not possible to pass the vapor pressure curve by varying another state variable. Thus, in this case the substance will stay in the one-phase region, e.g. changing from supercritical to gaseous or to liquid. No discrete changes in fluid properties occur. The closer pressure and temperature conditions get to the critical point, the greater changes in fluid properties will be when state variables vary.

The p, T-diagram in Figure 2.1 shows a projection from the pressure-volume-temperature (p, V, T) surface depicted in Figure 2.2 (page 14). It illustrates the different states of aggregation of a pure substance at any given pressure, volume and temperature; the coexistence lines and the two-phase regions. The two-dimensional diagrams of pressure versus temperature (p, T), pressure versus volume (p, V), and volume versus temperature (V, T) are projections of Figure 2.2 onto the corresponding variable plane. The p, V, T-behavior of a pure substance can be represented appropriately by a thermal equation of state (cf. Section 2.1.5).

2.1.4 Phase state

Different states of aggregation are also present in mixtures, e.g. in a multi-component system. In this case, the phases are characterized by their state of aggregation and by their main component, resulting in various possible *phase states*. For a CO_2-water system, possible phase states are 'liquid water-rich and gaseous CO_2-rich phase' or 'liquid water-rich, gaseous CO_2-rich and liquid CO_2-rich phase'.
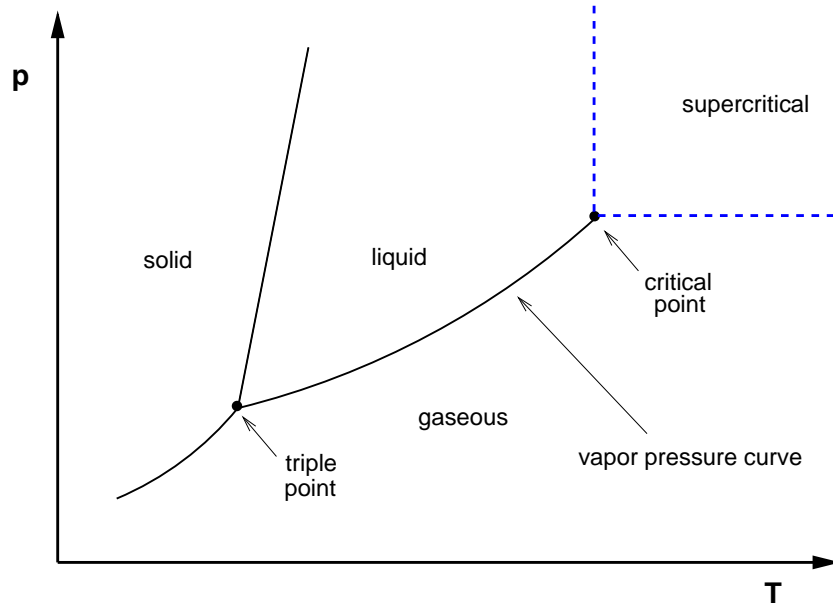
Figure 2.1: p, T-diagram of a pure substance. The coexistence lines of the liquid and the gas (vapor pressure curve), the liquid and the solid, and the gas and the solid are shown. Triple point and critical point characterize the behavior of the substance. If thermal conditions exceed the critical point the substance is in supercritical state.

2.1.5 Equation of state

An equation of state (EOS) is a mathematical representation of the relationship between pressure, volume, and temperature (p, V, T) of a pure substance for the entire fluid region including phase-coexistence curves. The Van-der-Waals cubic equation of state (VAN DER WAALS (1873) [100]) is the simplest form, where vapor-liquid coexistence can be qualitatively described. It is given by the following equation:

$$Z = \frac{pv}{RT} = \underbrace{\frac{v}{v-b}}_{\text{repulsive forces}} - \underbrace{\frac{a}{RTv}}_{\text{attractive forces}} \tag{2.1}$$

or

$$p = \frac{RT}{v-b} - \frac{a}{v^2} \tag{2.2}$$

where Z denotes the real gas factor and v the molar volume ($v = V/n$). a and b are the Van-der-Waals parameters and R is the universal gas constant ($R = 8.314 \, \text{J}/(\text{mol K})$). The first term accounts for the repulsive forces (on the right-hand side). The parameter b can be interpreted as the minimum volume that one mole of CO_2 molecules can occupy at infinitely high pressure. Attractive forces are considered by the second term including the parameter

13
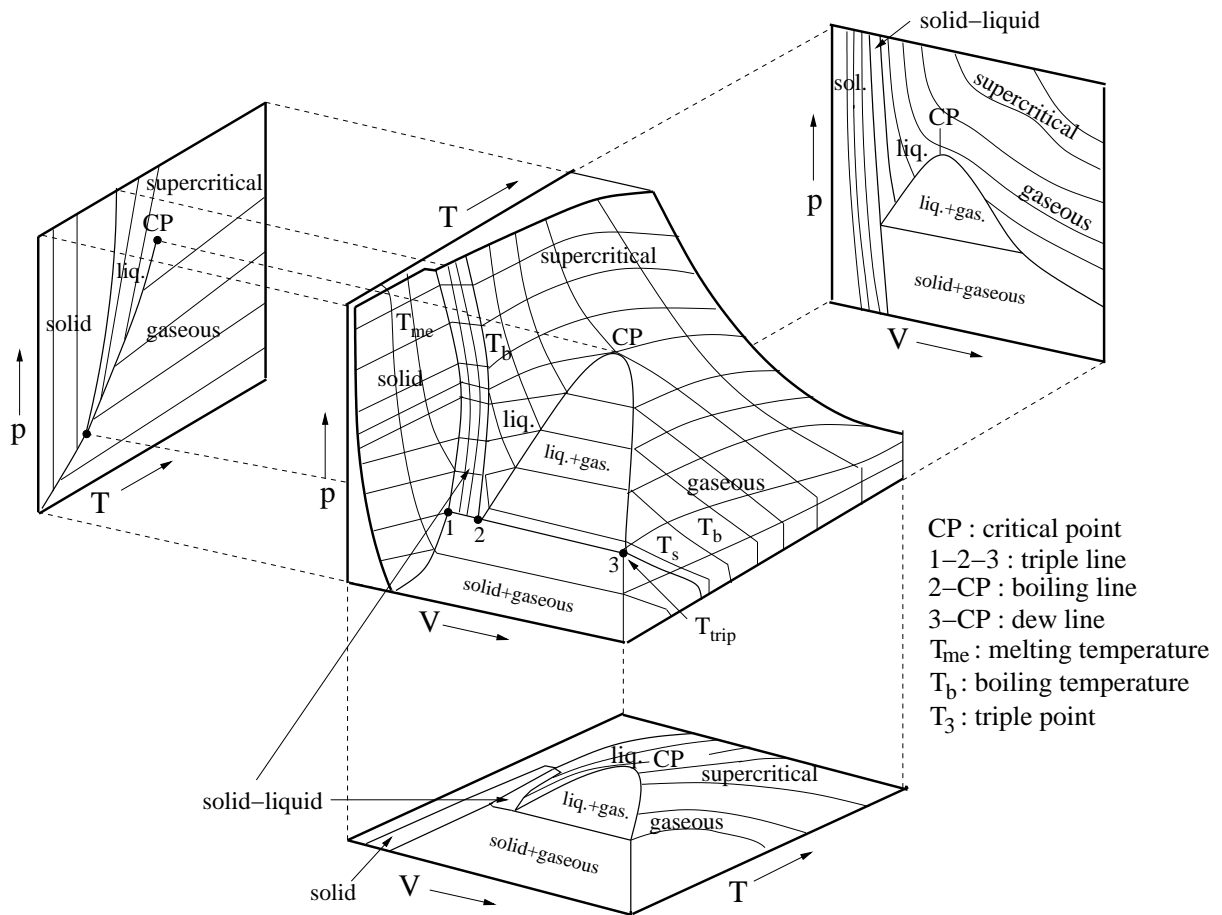
Figure 2.2: p, V, T-surface of a pure substance and projections into the p, T-diagram (showing isochors), the p, V-diagram (isotherms), and the T, V-diagram (isobars). Regions of different phase states and phase-coexistence lines are displayed.

a. Van der Waals proposed a constant parameter, but many extensions of his approach take into account the temperature dependence of the parameter *a*; this will be shown below. If both parameters *a* and *b* are set to zero, the Van-der-Waals equation reduces into the Ideal Gas Law that neglects any interactions between the molecules (e.g. ATKINS (2001) [10]).

The Van-der-Waals equation was the first approach to describe the gaseous, liquid, and supercritical p, V, T-behavior of fluids within one single equation. As this equation is a polynomial of third order, it is called a *cubic equation of state*.

The Van-der-Waals equation has been extended and improved by many authors (an overview can be found in POLING ET AL. (2001) [85]), one variation was proposed by PENG &

$$Z = \frac{pv}{RT} = \frac{v}{v-b} - \frac{a(T)v}{RT[v(v+b)+b(v-b)]} \tag{2.3}$$

or

$$p = \frac{RT}{v-b} - \frac{a(T)}{v(v+b)+b(v-b)}. \tag{2.4}$$

It is used for many technical applications with good success. Appendix B.1 describes the Peng-Robinson equation of state and its application to CO_2. Figure 2.3 depicts the results of equation (2.4) as isotherms in the p, v-plane, where v is the molar volume. For supercritical temperatures, the volume decreases monotonically with increasing pressure. At subcritical temperatures, there is a region where certain pressures yield three solutions for the volume. This is the vapor pressure curve where gaseous and liquid CO_2 coexist as two stable phases. The lowest and highest volumes represent the liquid and gaseous volumes, respectively, while a third solution is in the unstable two-phase region and is without technical relevance. With increasing subcritical temperatures, gaseous and liquid volumes approach each other until they meet at the critical point. The isotherm at the critical temperature shows the monotonic behavior of decreasing volume. At the critical pressure, the isotherm exhibits a saddle point.

As described in Appendix B.1, the parameters of the Peng-Robinson equation of state can be derived from the critical values of a substance. However, it is more exact to use parameters obtained from experimental results.

Equation of state for mixtures

To describe mixtures, the *one-fluid theory* is applied, i.e. the mixture is considered as one fluid with parameters that depend on the parameters of the pure substance and the composition of the mixture (PFENNIG (2004) [84]).

Mixing rules have to be set up to obtain mixture parameters. These rules have to take into account the properties of the pure components as well as the interactions between molecules of the various components. In the following, Van-der-Waals mixing rules are applied to determine the parameters for the mixture:

$$a_{\mathrm{mix}} = \sum_{i=1}^{N} \sum_{j=1}^{N} x_i x_j a_{i,j}, \tag{2.5}$$

$$b_{\mathrm{mix}} = \sum_{i=1}^{N} x_i b_i. \tag{2.6}$$

a_{mix} is found using a quadratic mixing rule (equation (2.5)), and b_{mix} is obtained with a linear mixing rule (equation (2.6)). N is the number of components, b_i corresponds to the
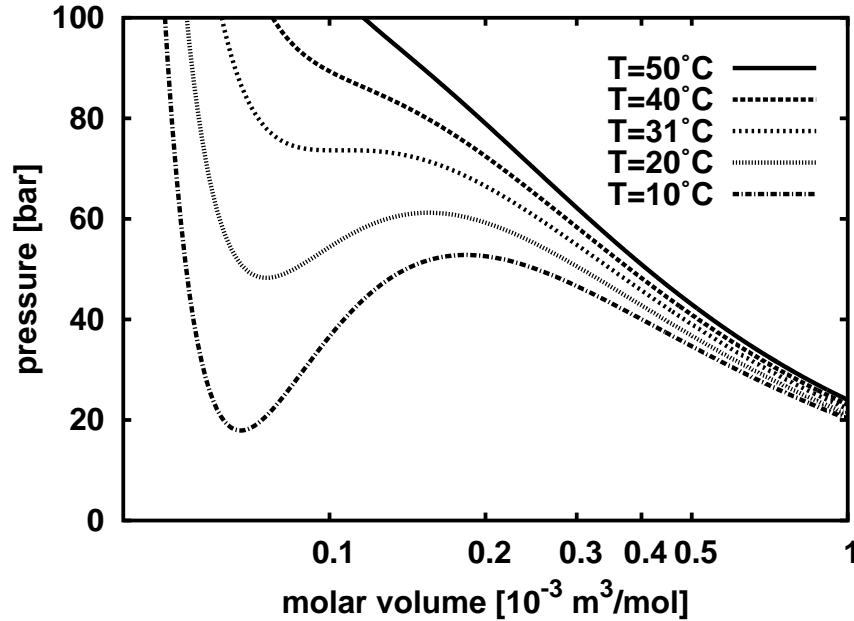
Figure 2.3: Pressure-volume diagram of CO_2 obtained using the Peng-Robinson EOS. At subcritical temperatures (10 and 20 °C), the vapor-liquid coexistence is characterized by a high volume for the gas phase and a second solution for the liquid phase (low volume) at constant pressure. At supercritical temperatures (40 and 50 °C) the volume decreases monotonically with increasing pressure. For the critical temperature (31 °C), a saddle point can be observed at the critical point.

pure components, and x_i is the mole fraction of component i in the mixture. $a_{i,j}$ refers to the pure substances if $i = j$ and to the interaction between molecules of different components if $i \neq j$ where $a_{i,j} = a_{j,i}$.

A mixing rule for the Peng-Robinson EOS and its application to the system CO_2-water using parameters of ADRIAN ET AL. (1998) [8] is explained in Appendix B.2.

Figure 2.4 depicts qualitatively a phase diagram for the system carbon dioxide-water as it can be obtained using the Peng-Robinson EOS (figure after SPYCHER ET AL. (2003) [97]). It shows the pressure over the total water mole fraction in the system (water within all occurring phases) at a constant temperature of 25 °C. To read this diagram, it is useful to start on the right-hand side at a mole fraction of 1 (only pure water is present) and at a pressure of e.g. 100 bar. If CO_2 is added to the system, the water mole fraction decreases and, at constant pressure, only a water-rich phase with some dissolved CO_2 exists. After the addition of more CO_2 to the system, the maximum solubility of CO_2 in water is reached and a second phase appears. At this point, the two-phase region consisting of a water-rich

liquid phase (with some dissolved CO_2) and a CO_2-rich liquid phase (with some dissolved water) is entered. If much more CO_2 is injected into the system and displaces the water-rich phase, the mole fraction of the total water content reaches very low values. If the maximum solubility of water in CO_2 is reached and the water mole fraction is reduced further, the water dissolves completely in the CO_2. Now, only one CO_2-rich phase is left. Note that only very high and very low water mole fractions are illustrated in Figure 2.4; the horizontal axis is interrupted, because both phases exist for most compositions.

In Figure 2.4, depending on the pressure conditions, CO_2 can be gaseous or liquid, because the temperature is subcritical for CO_2. Under the conditions described, water is far from its critical point and clearly above its vapor pressure curve. Therefore, it will mainly stay in the liquid phase. However, water can dissolve into the liquid or evaporate into the gaseous CO_2-rich phase.

The temperature also has a significant effect and changes the occurrence of the different phases. Under certain T, p, x-conditions, three phases can occur at the same time, namely a gaseous CO_2-rich phase, a liquid CO_2-rich phase and a water-rich liquid phase. As this is only a very small region, it is not shown in Figure 2.4.
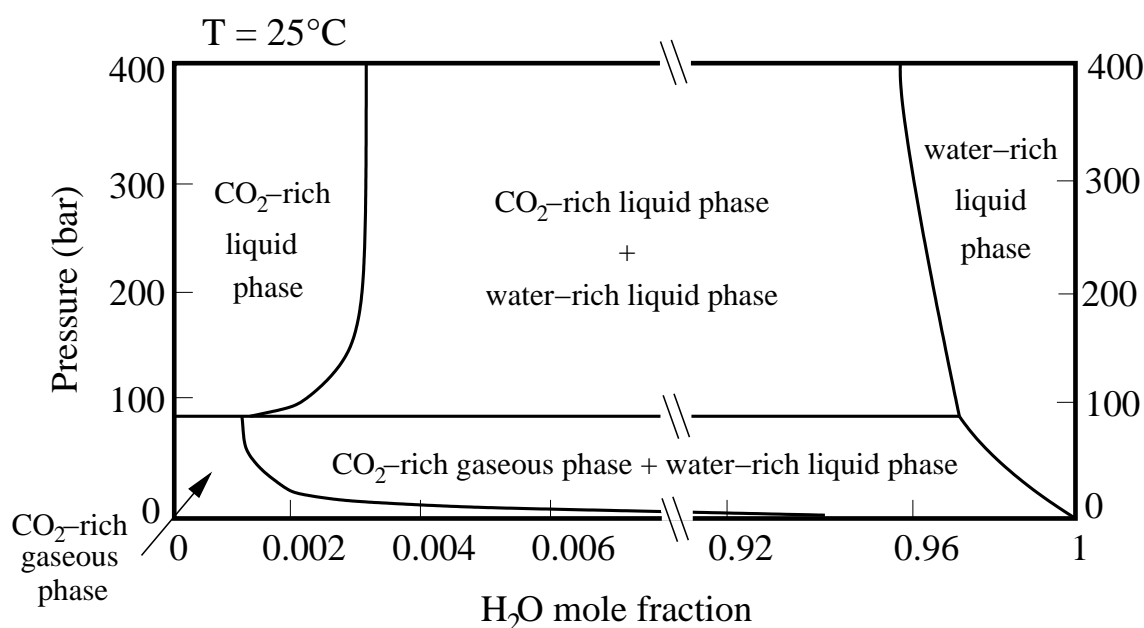
Figure 2.4: Phase diagram of the system CO_2-water at a constant temperature of $25\,°C$ (after SPYCHER ET AL. (2003) [97]).

2.1.6 Mole and mass fraction

Mole and mass fractions can be used to describe compositions of phases. Mole fractions x_α^{C} are defined as the ratio of the number of moles of a component C to the total number of moles in the system within phase α:

$$x_\alpha^{\mathrm{C}} = \frac{n_\alpha^{\mathrm{C}}}{\sum\limits_{\mathrm{C}} n_\alpha^{\mathrm{C}}}. \tag{2.7}$$

In analogy, the mass fraction X_α^{C} is defined by:

$$X_\alpha^{\mathrm{C}} = \frac{m_\alpha^{\mathrm{C}}}{\sum\limits_{\mathrm{C}} m_\alpha^{\mathrm{C}}}. \tag{2.8}$$

The sum of the mole fractions within a phase and the mass fractions within a phase are unity:

$$\sum\limits_{\mathrm{C}} x_\alpha^{\mathrm{C}} = \sum\limits_{\mathrm{C}} X_\alpha^{\mathrm{C}} = 1. \tag{2.9}$$

To quantify compositions in this work, predominantly mass fractions are used.

2.2 Fluid properties

The fluid properties density, enthalpy, and viscosity are essential for describing non-isothermal flow in porous media. They are explained in this section.

2.2.1 Density

Density is defined as mass per volume (mass density) or the number of moles per volume (molar density). In this work, mostly mass density is used:

$$\varrho = \frac{m}{V}. \tag{2.10}$$

The density of a pure substance depends on pressure and temperature; it usually increases with increasing pressure and decreasing temperature. In the case of mixtures, the density depends additionally on the composition. One example is formation water in deep geological formations that contains high salt concentrations. Its density is significantly higher than that of pure water (cf. Section 3.3.1).

2.2.2 Enthalpy

To take non-isothermal processes into account, it is necessary to consider caloric state variables. These are, for example, enthalpy and internal energy, which are explained in this section.

The extensive enthalpy H of a system includes its extensive internal energy U and its volume changing work pV:

$$H = U + pV. \tag{2.11}$$

Division by the mass of the system yields the specific enthalpy h:

$$h = u + pv = u + \frac{p}{\varrho}. \tag{2.12}$$

The specific internal energy u is the energy stored within one kilogram of the substance considered. With increasing temperature, the specific internal energy also increases. The derivative of specific internal energy with respect to temperature at constant volume yields the specific isochoric heat capacity at constant volume:

$$c_v = \left(\frac{\partial u}{\partial T} \right)_v. \tag{2.13}$$

If the volume of the system does not stay constant, the change of thermal energy does not necessarily correspond to the change in internal energy. Then, the difference between energy that has been added to the system and the internal energy gained is the change in volume, or the *volume changing work*.

The volume changing work plays an important role for gases, where density is strongly influenced by pressure variations. Liquids are only slightly compressible, therefore volume changing work has only a minor effect there.

Figure 2.5 gives an example to illustrate the dependence of specific enthalpy and specific internal energy on temperature and pressure. While there is no notable difference between enthalpy and internal energy for liquid water, the volume changing work makes a significant difference for the gas phase.

In the case of a multi-phase multi-component system, the enthalpy of the different components in the phases must be considered. Furthermore, it is necessary to take into account the heat of dissolution of the substances in the phases, i.e. the enthalpy change due to dissolution processes (cf. Section 3.3.2).
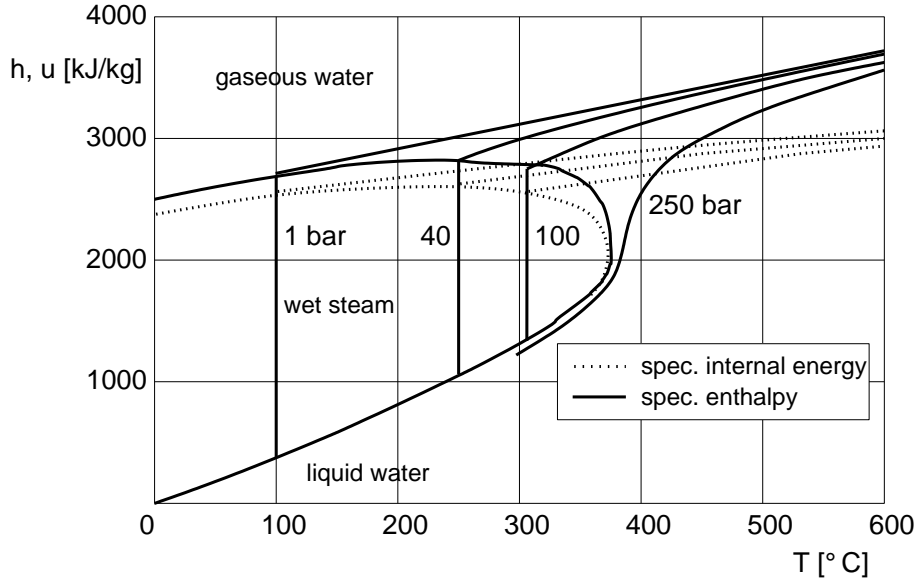
Figure 2.5: Specific enthalpy and specific internal energy of water at varying pressures and temperatures. For liquid water, enthalpy and internal energy are almost the same, because the volume hardly changes with pressure (low compressibility). Gaseous water (vapor) has a significantly higher enthalpy. Here, enthalpy and internal energy differ, because gas compressibility is high.

2.2.3 Viscosity

Dynamic viscosity μ is the proportionality factor of the relation between the fluid's shear tension τ and the velocity gradient:

$$\mu = \frac{\tau}{\partial v_x / \partial y}. \tag{2.14}$$

The viscosity of a liquid usually increases with increasing pressure and decreasing temperature. In a gaseous fluid, viscosity increases with pressure, but decreases with decreasing temperature. As for the density, it is necessary to take into account pressure and temperature effects on viscosity, as well as its dependence of composition in mixtures in some cases.

In this study, dynamic viscosity is referred to when mentioning viscosity. Nevertheless, for some purposes, it may be necessary to use the kinematic viscosity ν:

$$\nu = \frac{\mu}{\varrho}. \tag{2.15}$$

2.3 Properties of the porous medium

In this section, the properties of the porous medium needed for the mathematical description of multi-phase flow in the subsurface are explained.

2.3.1 Porosity

The porosity ϕ is a measure of the pore volume in a porous medium. It is defined by the ratio between the volume of the pores and the total volume:

$$\phi = \frac{V_{\text{pores}}}{V_{\text{total}}}. \tag{2.16}$$

In some cases, it is necessary to distinguish between porosity and effective porosity, i.e. the pore volume that is accessible for fluid flow.

The effects of temperature and pressure on the porosity are neglected in this work.

2.3.2 Saturation

In the case of several phases flowing in a porous medium, it is necessary to have a measure of the fraction of the pores filled with a fluid phase. This is given by the saturation S that is defined as the ratio between the volume of the pores filled with phase α and the total pore volume:

$$S_\alpha = \frac{V_\alpha}{V_{\text{pores}}}. \tag{2.17}$$

Following this definition, it is clear that the phase saturations have to sum up to unity:

$$\sum_\alpha S_\alpha = 1. \tag{2.18}$$

2.3.3 Permeability

The absolute (intrinsic) permeability $\mathbf{K}$ is a measure of the resistance of a particular porous medium towards flow of a fluid in its pores. It is a material property of the porous medium and assumed to be independent of the fluid. The absolute permeability is linked to the hydraulic conductivity $\mathbf{K}_{\text{f}}$ by taking into account the viscosity μ and density ϱ of the fluid:

$$\mathbf{K} = \mathbf{K}_{\text{f}} \frac{\mu}{\varrho \cdot g} \tag{2.19}$$

where g is the gravitational constant. In most cases, the $\mathbf{K}_f$-values refer to pure water as the pore-filling fluid.

Permeability is dependent on the porosity and the grain-size distribution of the porous medium (e.g. Hazen [48]). However, large porosities do not necessarily mean high permeabilities, e.g. clays have high porosities but very low permeabilities (e.g. Scheffer & Schachtschabel (1992) [89]).

The unit for permeability used in reservoir engineering is Darcy [D] (or Millidarcy [mD]). 1 D refers to the permeability that leads to a specific discharge of 1 cm/s for a fluid with a viscosity of 1 cp (1 cp = 1 Centipoise = $1 \cdot 10^{-3}$ Pa s) and a density of $1000\,\mathrm{kg/m^3}$ at a hydraulic gradient of 1000 m/m. One Darcy corresponds to a permeability of $1 \cdot 10^{-12}\,\mathrm{m^2}$.

2.4   Scales, REV

When fluid flow in porous media is modeled, it is necessary to choose an adequate scale for the subjects to be investigated. The following scales can be distinguished:

- molecular scale [$\sim 10^{-10}\,\mathrm{m}$],

- microscale (pore scale) [$\sim 10^{-3}\,\mathrm{m}$],

- macroscale [$\sim 10^{-1}\,\mathrm{m}$], and

- field scale [$\sim 10^{2}\,\mathrm{m}$].

It is also necessary to consider the relevant processes before setting up the model. In this way, it is possible to choose an adequate scale for the subjects to be investigated.

On the *molecular scale*, all the molecules of the different components and of the grains of the porous medium have to be taken into account. Such an approach allows to obtain extremely detailed information on flow considering all molecular interactions within flow and between the fluids and the matrix. But the derivation of macroscopic properties from these calculations is only feasible for very small model setups (e.g. Mader (2004) [69]). Considering the fact that one mole (18 g) of water consists of $6.022 \cdot 10^{23}$ molecules, it is obvious that only small systems are feasible on this scale.

To describe large systems, the *continuum approach* has to be used. Here, as a result of an averaging process over a sufficiently large number of molecules, the substance can be considered continuously distributed in space. In this way, it is possible to obtain macroscopic state variables, e.g. pressure and temperature, and fluid properties, e.g. density and viscosity.

Using them allows to describe flow on the continuum scale, which comprises the micro-, macro-, and field scales.

On the *microscale* or *pore scale*, the fluids flow through the small paths formed by interconnected pores within the matrix of the porous medium. It is possible to simulate the flow paths of different fluids in the pore channels by solving the *Navier-Stokes equations*. The problem on the microscale is that it is difficult to get information on the geometry of the pores and flow paths for realistic problems. Even if detailed data on the geometry are available, it is not feasible so far to solve the Navier-Stokes equations for these structures for large problem sizes.

To move to the *macroscale*, it is necessary to conduct another averaging procedure that leads to new variables not known on the microscale. For the averaging, it is first necessary to find a *Representative Elementary Volume* (REV) that gives realistic information on the porous medium (BEAR (1972) [18]). Figure 2.6 shows the search for a REV using porosity as an example. If a very small volume is chosen for the REV, the porosity fluctuates between zero and one depending on whether a pore or a grain is being looked at. When the volume is enlarged, an increasing number of pores and grains are included and the porosity variations decrease until V_0 is reached. Here, a further extension of the volume does not change the porosity anymore; it is the minimum value for the REV. If the volume is increased to values that are too large, heterogeneities on the macroscale of the porous medium start to have an effect on the value of the averaged porosity.

With a suitable REV, it is possible to conduct the averaging process for this volume. Note the assumption that it is possible to use one single REV for the averaging of various parameters. Apart from the averaged material parameters like porosity and permeability, new variables appear due to the averaging procedure, e.g. the phase saturations. Figure 2.7 (page 25) illustrates the transition from the micro- to the macroscale. An averaging procedure is applied resulting in saturations of the phases distributed over the domain. New equations, e.g. Darcy's Law, only hold on this macroscale.

2.5 Processes in porous media

This section gives an overview of the various processes that can take place when non-isothermal fluid flow in porous media is investigated.
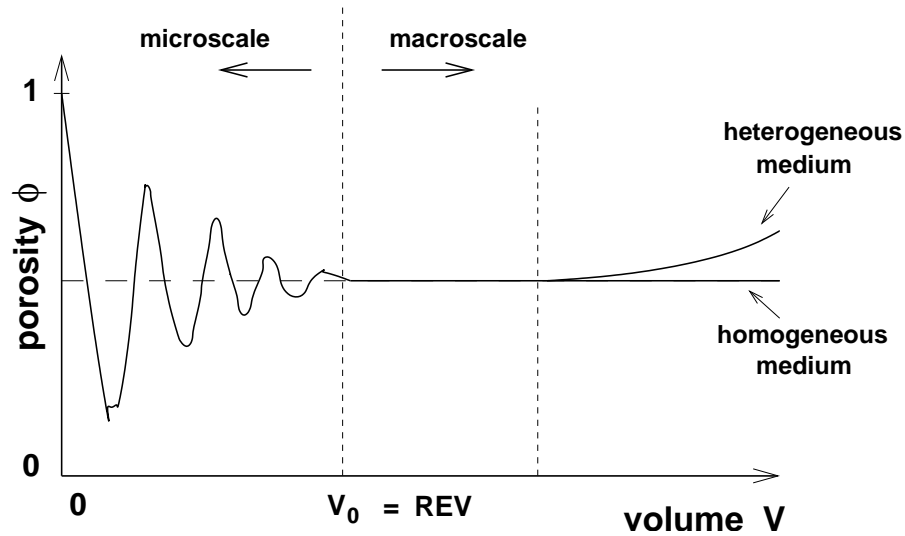
Figure 2.6: Definition of a Representative Elementary Volume (REV) after BEAR (1972) [18]. The REV is found if the variable (in this case porosity) stays constant when volume is changed slightly.

2.5.1 Advection

Advection is the fluid movement due to pressure gradients. Figure 2.8 illustrates the advection process for an immiscible two-phase system. Fluid A flows from left to right, because its pressure decreases in the same direction, $p_1 > p_2$. At the same time fluid B is displaced towards the right.

As pressure may have gradients in all spacial directions advective flow can go into all directions as well. For example, when fluid A is injected into a porous medium fully saturated with fluid B, the additional external pressure required will cause fluid A to flow in all directions, away from the injection point.

2.5.2 Buoyancy

Buoyancy flow is caused by density differences within a phase (e.g. salt-/freshwater) or between two phases (e.g. CO_2 and water). Both processes are described for one-phase water flow in porous media by Darcy's Law and for multi-phase flow by the extended Darcy's Law. The equations are explained in Section 2.6.1.

On the right-hand side of Figure 2.8, the process of buoyancy in a two-phase system is depicted. Initially, fluid B forms a layer on top of fluid A. As fluid A is of lower density than
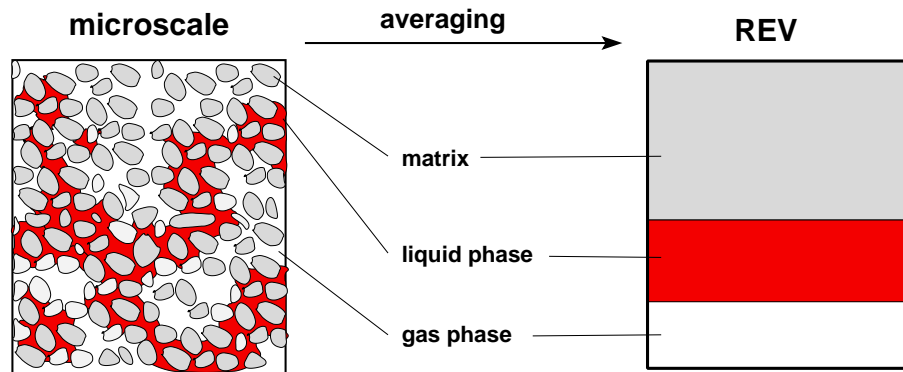
Figure 2.7: Transition from micro- to macroscale (after CLASS (2000) [27]). Averaging the volume fractions within the REV occupied by matrix, pore space, and fluids results in macroscale parameters, e.g. porosity and fluid saturation.

fluid B, buoyancy causes fluid A to rise to the top. At the same time, fluid B has to migrate downwards for continuity reasons in a closed system.
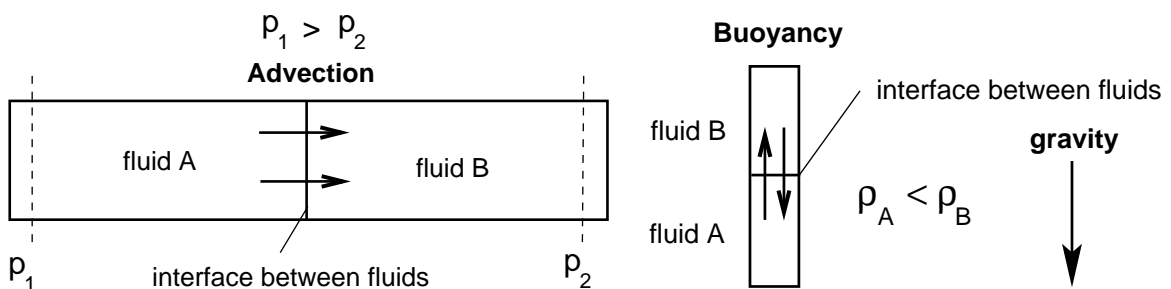
Figure 2.8: Advection and buoyancy in multi-phase flow. Advection is caused by pressure gradients. In this example, fluids A and B are displaced from left to right. Density differences cause buoyancy flow. Here, fluid A flows upwards, because it has a lower density than fluid B.

2.5.3 Diffusion

Diffusion is the equilibration of differences in density or velocity of molecules due to Brownian molecular movement (e.g. MESCHEDE (2004) [73]). Thus, diffusive fluxes are driven by concentration gradients or temperature gradients. In contrast to advection and buoyancy, diffusion is independent of orientation, i.e. it behaves the same in all spatial directions. A Fickian approach can be used to describe the mass flux $\mathbf{j}_\alpha^C$ of a dissolved substance C in the

solvent phase α (e.g. ATKINS (2001) [10]):

$$\mathbf{j}_\alpha^C = -\varrho_\alpha \, \mathbf{D}_{pm}^C \, \nabla X_\alpha^C \qquad (2.20)$$

where ∇X_α^C is the composition gradient in terms of mass fraction. The diffusion coefficient of component C in the porous medium $\mathbf{D}_{pm}^C$ depends on the binary diffusion coefficient of the substance in water $\mathbf{D}_\alpha^C$ and the accessible pathways (e.g. CLASS (2000) [27]):

$$\mathbf{D}_{pm}^C = \tau \phi S_\alpha \mathbf{D}_\alpha^C. \qquad (2.21)$$

Here, S_α stands for the saturation of phase α, and tortuosity τ is a measure of the irregularity of the flow paths. Values for τ can be found using an approach suggested by MILLINGTON & QUIRK (1961) [75]:

$$\tau = \frac{(\phi S_\alpha)^{7/3}}{\phi^2}. \qquad (2.22)$$

2.5.4   Dispersion

Mechanical dispersion contains two processes, namely *micro-dispersion* and *macro-dispersion*. Micro-dispersion takes place on the pore scale (cf. Section 2.4) and is caused by the parabolic velocity profile between the soil grains and velocity fluctuations due to the flow paths. Macro-dispersion occurs on the macroscale due to heterogeneities of the soil or rock. Both, micro- and macro-dispersion, depend on the flow velocity of the moving fluid.

Mechanical dispersion has been investigated thoroughly for one-phase systems (e.g. KINZEL-BACH (1987) [64] or CIRPKA & KITANIDIS (2000)[26]). For multi-phase systems, only few approaches to quantifying mechanical dispersion are available (e.g. MILLINGTON & QUIRK [75]). It is neglected in the model concept presented in this work. Since molecular diffusion and mechanical dispersion can be described mathematically in a similar way, it is easy to implement the latter into the model concept. However, mechanical dispersion is neglected in this study, because no parameters are available for the considered system.

2.5.5   Heat conduction

Heat conduction is the process of the transmission of heat from regions of higher to those of lower temperatures in any kind of matter. It is driven by temperature gradients ∇T and depends on the heat conductivity λ, which is a material property. *Fourier's Law* describes heat conduction with

$$\dot{q} = -\lambda \nabla T \qquad (2.23)$$

where $\dot{q}$ is the heat flux density (e.g. BAEHR & STEPHAN (1998) [12]).

The heat conductivity λ is the factor of proportionality in Fourier's Law and quantifies the ability of a material to transport heat. Values of λ can vary significantly between bad heat conductors (e.g. air at ambient conditions, $\lambda \approx 0.03$ W/mK) and good ones (e.g. aluminum at ambient conditions, $\lambda \approx 238$ W/mK).

In the case of multi-phase flow in a porous medium, it is possible to describe heat conduction for the different phases separately. Often it makes sense to assume local thermal equilibrium and to define an integral heat conductivity λ_{pm} and temperature for all phases including the porous medium at one point of the investigated domain (cf. Section 2.6.2 and 3.4).

2.5.6 Capillarity on the pore scale

Capillarity plays an important role in porous media. It is caused by intermolecular forces resulting in cohesion and adhesion.

Cohesion is due to interactions between molecules of the same type. It causes the *surface tension* of liquids at the interface to another fluid. Due to the surface tension, a liquid tends to form an interface to the other fluid which has a minimum surface area (spherical surface). The force caused by the surface tension with respect to an area yields the cohesion pressure

$$p_{\mathrm{cohesion}} = \frac{2\sigma}{r_{\mathrm{int}}} \tag{2.24}$$

where σ is the surface tension and r_{int} the radius of the interface. The cohesion pressure increases with increasing surface tension and decreasing radius of the surface.

Adhesion is the interaction between molecules of different type, e.g. a solid surface and a liquid.

Cohesion and adhesion cause capillarity; this becomes clear in Figure 2.9, where a single capillary and the interface between two fluids, a liquid at the bottom and a gas above, is shown. Here, also the vectors of the cohesive force F_{coh} and the adhesive force F_{adh} are depicted. The resulting force vector F_{R} bends the interface to be perpendicular to it. Therefore, cohesion and adhesion cause a rise of the liquid in the capillary. The angle between the fluid interface and the solid wall of the capillary is called the *contact angle θ*. Neglecting interactions between fluid and solid explicitly, it defines the wettability of a fluid:

$$
\begin{array}{rcccl}
0° & \leq \theta < & 90° & \text{wetting fluid,} \\
90° & < \theta \leq & 180° & \text{non-wetting fluid,} \\
& \theta = & 90° & \text{no capillary forces.}
\end{array}
$$

27
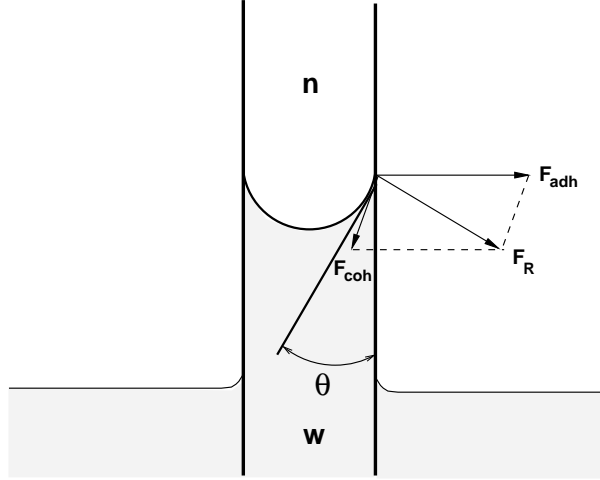
Figure 2.9: Cohesive and adhesive forces causing capillarity.

In Figure 2.9, the wetting fluid (w) is the liquid in the lower part and the non-wetting fluid (n) the gas in the upper part of the capillary.

If r is the radius of the capillary and r_{int} the radius of the interface, it can be stated that $\cos\theta = r/r_{\mathrm{int}}$. Insertion of this into equation (2.24) and on the assumptions that the cohesion pressure is in equilibrium with gravity forces ($p_{\mathrm{grav}} = \varrho_{\mathrm{fl}}gh$), it is possible to obtain the capillary height h_{cap}:

$$h_{\mathrm{cap}} = \frac{2\sigma\,\cos\theta}{\varrho_{\mathrm{fl}}gr}. \tag{2.25}$$

Expressing this as a pressure yields the *capillary pressure* on the microscale:

$$p_{\mathrm{cap}} = \frac{2\sigma\,\cos\theta}{r}. \tag{2.26}$$

2.6 Modeling of flow in porous media

2.6.1 Darcy's Law

Darcy's Law describes fluid flow in a porous medium on the macroscale. It states

$$\mathbf{v} = -\mathbf{K}_{\mathrm{f}}\nabla h \tag{2.27}$$

where $\mathbf{v}$ is the Darcy velocity, $\mathbf{K}_{\mathrm{f}}$ the hydraulic conductivity for water and h the piezometric head. Darcy's Law is valid for seeping flow with Reynold's numbers of $Re < 1$. For the

dimensionless Reynold's number (Re) in a porous medium, the mean pore diameter d, a typical flow velocity v, and the kinematic viscosity of the fluid ν are used:

$$Re = \frac{d\,v}{\nu}. \tag{2.28}$$

For multi-phase flow, Darcy's Law is commonly extended by introducing relative permeability k_r (cf. Section 2.6.5) and referring to phase pressures p_α (e.g. HELMIG (1997) [52]):

$$\mathbf{v}_\alpha = -\frac{k_{\mathrm{r}\alpha}}{\mu_\alpha}\,\mathbf{K}\,(\nabla p_\alpha - \varrho_\alpha \mathbf{g}). \tag{2.29}$$

Intrinsic permeability $\mathbf{K}$ (cf. equation (2.19)) and the piezometric head $h = p/(\varrho g) + z$ are used. The extended version of Darcy's Law includes fluid flow due to viscous forces (advection) and buoyancy forces (cf. Section 2.5.1 and 2.5.2).

The Darcy velocity $\mathbf{v}_\alpha$ refers to the flow through the total cross-section of the porous medium. To calculate the actual particle speed, the seepage velocity $\mathbf{v}_{\mathbf{a},\alpha}$ is introduced:

$$\mathbf{v}_{\mathbf{a},\alpha} = \frac{\mathbf{v}_\alpha}{\phi}. \tag{2.30}$$

With the porosity the seepage velocity takes into account only the space that is accessible to fluid flow; thus, the seepage velocity is always greater than the Darcy velocity.

2.6.2 Equilibrium assumptions

Thermodynamic equilibrium comprises three conditions (e.g. PFENNIG (2004) [84]):

- thermal equilibrium,
- mechanical equilibrium,
- chemical equilibrium.

Thermal equilibrium is given when the temperature is constant in the entire system. In the present work, *local thermal equilibrium* is assumed, i.e. the temperature of all phases including the matrix are the same at a finite volume in space. Therefore, local temperature differences, e.g. as a result of slow heat transfer from the fluid to the matrix, are neglected. If flow velocities are slow, this is a reasonable assumption.

Mechanical equilibrium is given if pressures are constant in a system. If pressures are the same locally in all the phases present, *local mechanical equilibrium* is maintained. Therefore, the pressures at an interface have to be the same on both sides. In a porous medium,

capillary effects have to be taken into account to obtain equal pressures on both sides of an interface between the fluid phases (cf. Section 2.6.4). Then, the assumption of local mechanical equilibrium holds.

Chemical equilibrium exists if the chemical potential of every component is the same throughout all phases in the entire system under consideration. In this study, *local chemical equilibrium* is assumed, i.e. the chemical potential is the same for a component within all phases locally. No kinetics are taken into account; instantaneous phase equilibrium of the distribution of the components in the phases is assumed. Slow flow velocities justify this assumption.

Thermal, mechanical, and chemical equilibrium are fulfilled locally; it is therefore valid to state *local thermodynamic equilibrium* for this study.

2.6.3 Gibbs' phase rule

Any thermodynamic system can be described unambiguously by a set of state variables which are independent of each other. To determine the number of state variables required to describe a system, *Gibbs' phase rule* is applied. It states that the number of degrees of freedom (F) of a system depends on the number of components (C) and phases (P) in the system:

$$F = C - P + 2. \tag{2.31}$$

For example, a system containing two components and two phases has two degrees of freedom, i.e. two independent state variables are needed to specify the state point of the system. They determine all values of the secondary state variables of the system, e.g. density and viscosity.

With a macroscopic consideration for the modeling of fluid flow in a porous medium, one degree of freedom has to be added to Gibbs' phase rule. This is, a different phase saturation can be present at any location of the considered domain. Thus, the degree of freedom increases by the maximum number of phases that occurs. As the sum of all phase saturations adds up to unity, this number can be reduced by one and Gibbs' phase rule can be reformulated for macroscopic consideration:

$$F = C - P + 2 + (P - 1) = C + 1. \tag{2.32}$$

For a two-component system, where two phases are present, three independent state variables are needed to consider varying saturations.

2.6.4 Capillary pressure

Capillarity on the microscale is discussed in Section 2.5.6. These fluid-matrix interactions are modeled on the macroscale by formulating a capillary pressure curve as a function of

fluid saturation [52]. In the case of two phases, well-known empirical functions have been set up by Brooks & Corey (1964) [20] (equations (2.33) and (2.35)) and van Genuchten (1980) [44] (equations (2.34), (2.35), and (2.36)):

$$p_{\mathrm{c}} = p_{\mathrm{d}}\, S_{\mathrm{e}}^{-1/\lambda}, \tag{2.33}$$

$$p_{\mathrm{c}} = \frac{1}{\alpha}(S_{\mathrm{e}}^{-1/m} - 1)^{1/n}, \tag{2.34}$$

$$\text{with} \quad S_{\mathrm{e}} = \frac{S_{\mathrm{w}} - S_{\mathrm{wr}}}{1 - S_{\mathrm{wr}}}, \tag{2.35}$$

$$m = 1 - \frac{1}{n}. \tag{2.36}$$

Here, S_{e} is the effective saturation and S_{wr} the residual saturation of the wetting phase. The Brooks-Corey correlation uses the parameters p_{d} and λ, where p_{d} is the pore entry pressure, which is the pressure necessary for the non-wetting fluid to enter the largest pore of the porous medium. λ can be interpreted as a shape parameter for the curve. It assumes small values for heterogeneous material and a wide range of grain sizes (e.g. $\lambda = 0.2$) and larger values for homogeneous material (e.g. $\lambda = 3.0$). The Van-Genuchten correlation uses the parameters α, m, and n. Here, α expresses the inverse capillary pressure $(1/p_{\mathrm{c}})$ at an effective saturation of $S_{\mathrm{e}} = 0.5$ for given parameters m and n. The parameters for these capillary pressure-saturation relationships can be found by fitting the approaches to experimental data. Lenhard et al. (1989) [65] give a relation between the Brooks-Corey and the Van-Genuchten parameters.

An example of capillary pressure-saturation relationships after Brooks-Corey and Van-Genuchten is depicted in Figure 2.10 (page 33). Both curves are plotted for the same material using the parameters given in Table 2.1. Note that the curves show a similar behavior except in the region of high saturations of the wetting phase. Here, the Brooks-Corey approach yields a pressure discontinuity at full water saturation, representing the entry pressure p_{d}. The Van-Genuchten function starts at zero capillary pressure for full wetting phase saturation and increases continuously during a drainage process (displacement of the wetting by a non-wetting phase).

The approach of the capillary pressure-saturation relationship does not account for the following phenomena:

- **Hysteresis:** hysteresis describes the phenomenon that a value for capillary pressure can be matched to more than one saturation, depending on whether a drainage or an imbibition process is taking place. Furthermore, several changes between drainage and imbibition result in different capillary pressures at any time a particular saturation is reached. Thus, the history of the saturation changes has to be taken into account if

Table 2.1: Brooks-Corey and Van-Genuchten parameters for the same material.

Brooks-Corey	p_d	$2 \cdot 10^5$ Pa
Brooks-Corey	λ	2.0
Van-Genuchten	α	$3.3 \cdot 10^{-6}$ Pa^{-1}
Van-Genuchten	n	4.367
	S_wr	0.1
	S_nr	0.0

the processes are to be modeled properly. A detailed description of hysteresis and its modeling can be found in SHETA (1999) [92].

- **Dynamic effects:** for the application of the capillary pressure-saturation relationship, it is assumed that the difference of the phase pressures equals the equilibrium capillary pressure at a particular saturation under all flow conditions that satisfy the Reynolds number criterion. However, it has been shown in laboratory experiments that the capillary pressure under transient flow conditions can differ distinctly from the equilibrium p_c at a given saturation. Theoretical as well as laboratory investigations have suggested that the difference in the pressures of the non-wetting and the wetting phase, usually called the dynamic capillary pressure, to the capillary pressure is a function of the rate of change of saturation. The examination of these extended capillary pressure-saturation relationships is currently a field of intensive research (e.g. DAHLE ET AL. (2005) [31] MANTHEY ET AL. (2005) [70]).

- **Surface tensions:** The surface tension of the fluids changes with temperature and composition. This has an effect on the capillary pressure-saturation relationship that has been investigated e.g. by SHE & SLEEP (1998) [91].

Furthermore, heterogeneities of the porous medium, composition of the fluids, and the distribution of phase interfaces are only taken into account within the averaging framework that has been discussed in Section 2.4.

All these problems are not taken into account in this work. Nevertheless, it has been shown that it is useful to use capillary pressure-saturation relationships to describe the interactions between the fluids and the matrix. Especially when heterogeneous domains are under consideration it is important to consider entry pressure effects etc. to model multi-phase flow in a porous medium properly.
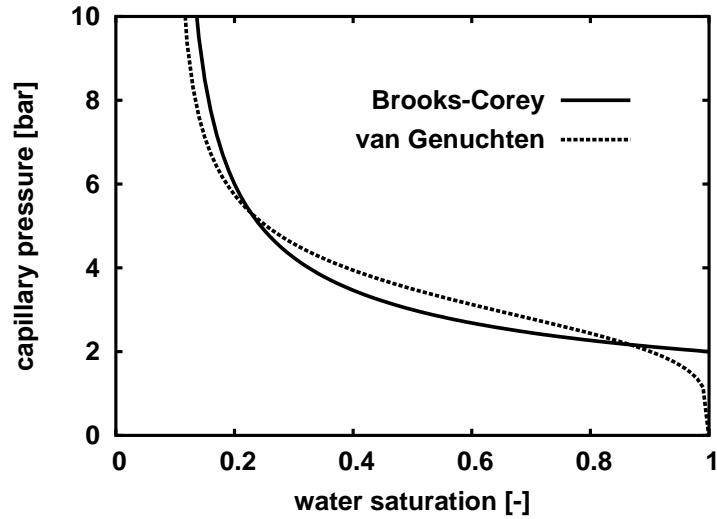
Figure 2.10: Capillary pressure-saturation curves of Brooks & Corey (1964) [20] and van Genuchten (1980) [44] for the same material. The curves differ significantly only at high water saturations: while the Brooks-Corey approach takes the entry pressure p_d into account, the Van-Genuchten curve yields zero capillary pressure for full water saturation.

Residual saturation

The residual saturation $S_{\alpha r}$ is the saturation of a phase in a multi-phase flow system which cannot be displaced by viscous forces. For the wetting phase this saturation is caused by capillary forces (cf. Section 2.5.6); it is also called irreducible saturation. The non-wetting phase residual saturation is caused by zero relative permeability (cf. Section 2.6.5) of the surrounding pores. Often it is called entrapped non-wetting phase saturation.

Note that the phase saturation can fall below the residual saturation due to diffusive processes or phase transition (e.g. evaporation). The residual saturation depends strongly on the composition of the porous medium, e.g. in clay, the residual saturations are much higher than in sandy material.

2.6.5 Relative permeability

If two phases flow in a porous medium, they disturb each other by occupying part of the pore space and thus blocking the other fluid. Consequently, the higher the saturation of a fluid, the larger the cross-section of its flow paths in the pores and the easier it is for the fluid to flow. This fact is taken into account by scaling the intrinsic permeability $\mathbf{K}$ by the saturation-dependent function k_r, called relative permeability, to get an effective

permeability $\mathbf{K}_{\mathrm{e}}$:

$$\mathbf{K}_{\mathrm{e}} = k_{\mathrm{r}} \cdot \mathbf{K}. \tag{2.37}$$

The relative permeability of phase α runs from zero for residual saturation to one for full saturation of the corresponding phase:

$$0 \leq k_{\mathrm{r}\alpha}(S_{\alpha}) \leq 1. \tag{2.38}$$

Relative permeabilities as functions of the saturations can be derived from capillary pressure-saturation relationships by applying the theory of BURDINE (1953) [21] or MUALEM (1976) [76]. They used capillary tube models to find the relationships for the wetting phase (subscript w) and for the non-wetting phase (subscript n). The Brooks-Corey approach yields:

$$k_{\mathrm{rw}} = S_{\mathrm{e}}^{\frac{2+3\lambda}{\lambda}}, \tag{2.39}$$

$$k_{\mathrm{rn}} = (1 - S_{\mathrm{e}})^2 \left(1 - S_{\mathrm{e}}^{\frac{2+\lambda}{\lambda}}\right). \tag{2.40}$$

For the Van-Genuchten functions, relative permeabilities are given by:

$$k_{\mathrm{rw}} = \sqrt{S_{\mathrm{e}}}[1 - (1 - S_{\mathrm{e}}^{1/m})^m]^2, \tag{2.41}$$

$$k_{\mathrm{rn}} = (1 - S_{\mathrm{e}})^{\frac{1}{3}}[1 - S_{\mathrm{e}}^{1/m}]^{2m}. \tag{2.42}$$

Figure 2.11 shows the relative permeability-saturation relationships for the approaches of Brooks and Corey and van Genuchten with the parameters given in Table 2.1. At low saturations wetting phase relative permeabilities are lower than those of the non-wetting phase. The reason for this is the fact that the wetting phase predominantly fills the small pores. Note that the relative permeabilities reach zero for the residual saturations of the respective phases.
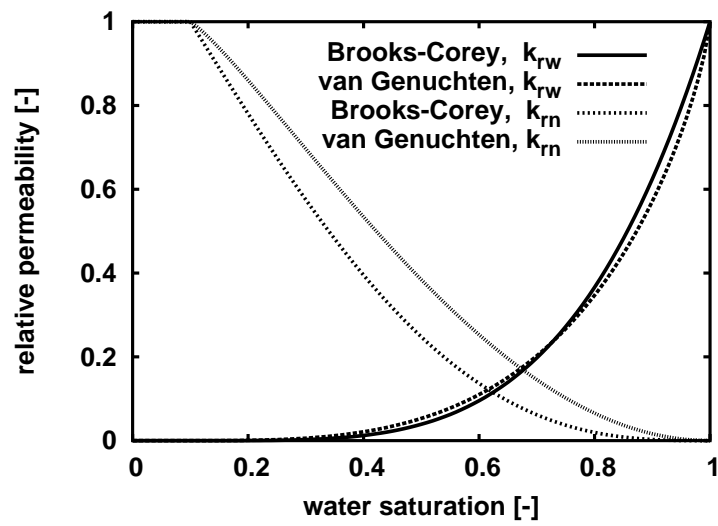
Figure 2.11: Relative permeability-saturation curves of Brooks & Corey (1964) [20] and van Genuchten (1980) [44] for the same material.

Chapter 3

Conceptual model

In this chapter, the fundamentals explained in Section 2.1 are applied to the problem of CO_2 sequestration. First, the multi-phase multi-component approach including salinity is discussed. After a description of mass transfer between the phases, the properties of the fluid phases water (brine) and CO_2 are explained, including the influence of the dissolved components. Furthermore, the processes that are taken into account by the introduced model are described in detail.

The present model is applicable to conditions of CO_2 injection into geological formations at depths between 1000 and 1500 m. Pressures, temperatures and salinities need to cover the range from the surface of the earth down to the storage reservoir and below so that all possible CO_2 migration paths can be modeled. Table 3.1 shows the expected ranges (cf. Section 5.1).

Table 3.1: Temperature, pressure, and salinity range of the model.

state variable	minimum value	maximum value
temperature	10 °C	80 °C
pressure	1 bar	200 bar
salinity	0 kg/kg	0.3 kg/kg

3.1 The multi-phase multi-component approach

The main substances to be taken into account when describing flow and transport during CO_2 sequestration are CO_2, formation water and, of course, the rock matrix that forms the

porous medium. For this, a two-phase two-component model concept is chosen, as depicted in Figure 3.1: we distinguish between a CO_2-rich phase (subscript CO2) and a water-rich phase (w). They each contain the components CO_2 (superscript CO2) and water (w) that are transferred between the phases, i.e. the water-rich phase consists of water and some dissolved CO_2 and the CO_2-rich phase contains CO_2 and a relatively small amount of water. Note that Figure 3.1 refers to the water-rich phase as a liquid and the CO_2-rich phase as a gas; therefore, CO_2 dissolves in the water while water evaporates into the CO_2 phase. When CO_2 is supercritical (cf. Section 3.2.1) its density can be liquid-like. In this case, it is more appropriate to talk of dissolution of water in the CO_2-rich phase. Therefore, in this study the more general terms *mutual dissolution* or *mass transfer between phases* are applied. The transfer of the components between the phases is influenced by pressure, temperature, and salinity (cf. 3.1.1).

The rock matrix is considered to be rigid, its effects on fluid flow are taken into account by porosity, permeability, capillary pressures and relative permeabilities. These properties and functions are assumed to be time-independent.
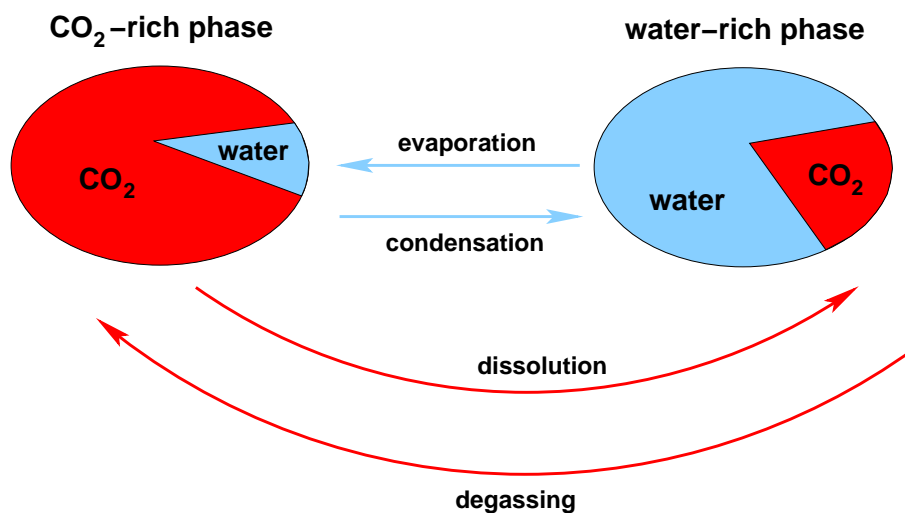
Figure 3.1: Two-phase two-component model concept for the system CO_2-water. A CO_2-rich and a water-rich phase exist, both containing carbon dioxide and water.

3.1.1 Salinity

At depths of 1000 m or more, aquifers often carry formation water with high salinities. As its properties differ significantly from pure water, the formation fluid is often referred to as *brine* (e.g. FYFE ET AL. (1978) [40]). The salt content strongly affects the solubility of CO_2.

Different measures are used to express the salt content of brine that can reach values of up to $0.3\,\mathrm{kg}$ salt/kg solution (Bachu & Adams (2002) [7]). Table 3.2 gives an overview of various measures for describing salinity. Composition definitions are given in Appendix A. Note that in this work the mass fraction S is always used to express salinity.

Table 3.2: Salt contents in formation water using different composition measures.

molality $\left[\mathrm{mol\ salt}/\mathrm{kg\ solvent}\right]$	S: mass fraction $\left[\mathrm{kg\ salt}/\mathrm{kg\ solution}\right]$	s: salinity $\left[\mathrm{kg\ salt}/\mathrm{kg\ solvent} \cdot 1000\right] = [\permil]$	c: salt concentration $\left[\mathrm{kg\ salt}/\mathrm{m^3\ solution}\right]$
1.90	0.1	111.1	106.54
4.28	0.2	250.0	228.18
6.28	0.3	428.6	366.73

In this model, the salinity S is not treated as a third component but as a parameter that can vary in space but not in time:

$$S = f(x, y, z). \tag{3.1}$$

In this way, it is possible to take into account changes in brine fluid properties due to its salt content. Furthermore, the *salting-out effect*, i.e. the reduction of CO_2 solubility in brine with increasing salinity, can be considered.

With this approach, local salinity changes, e.g. due to brine movement, and salt precipitation are neglected. In this way, one more mass balance equation for the salt component can be avoided and computational effort therefore reduced. However, it is assumed that the first order effects of the salinity on the flow and transport behavior of CO_2 in the subsurface are captured by this approach.

3.1.2   Mass transfer between the phases

The mass transfer between the phases includes the dissolution of CO_2 in water and of water in the CO_2 phase.

Dissolution of CO_2 in water: CO_2 dissolves in water, forming carbonic acid (H_2CO_3), hydrogen carbonate (HCO_3^-), and carbonate (CO_3^{2-}) in accordance with the reaction equation

$$
\begin{aligned}
CO_2 + H_2O &\rightarrow H_2CO_3, \\
H_2CO_3 + H_2O &\rightarrow HCO_3^- + H^+ + H_2O, \\
HCO_3^- + H_2O &\rightarrow CO_3^{2-} + H^+ + H_2O.
\end{aligned} \tag{3.2}
$$
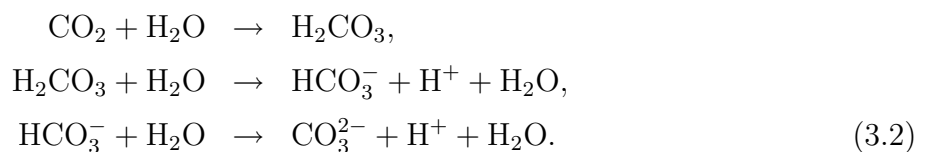
During the reaction, protons (H^+) are released into the solution causing a lowering of the pH-value. This change in pH and the resulting chemical reactions with the rock matrix are not addressed here. The equilibrium of reaction equation (3.2) and the resulting amount of dissolved CO_2 are influenced by the thermodynamic conditions of the system, namely by pressure and temperature. The salt content also plays an important role, because the salt ions affect the molecular interactions between the water and the CO_2 molecules. In general, increasing pressure causes more CO_2 to be dissolved while increasing temperature and salinity reduce CO_2 solubility in water.

The amount of dissolved carbon dioxide can be quantified by combining experimental and theoretical knowledge into an EOS for the system CO_2 - brine. Here, various approaches from literature are compared. In addition, an EOS for the system CO_2 - water is used as a reference.

- **Henry approach:** BATTISTELLI ET AL. (1997) [16] suggest an extension of Henry's Law to calculate the amount of CO_2 dissolved in the water phase. Henry's Law is given in its basic form by

$$x_w^a = \frac{p_g^a}{H} \tag{3.3}$$

where x_w^a is the mole fraction of component a in the water phase and p_g^a the partial pressure of component a in the gas phase. In this approach the Henry coefficient H is a function of temperature and salinity:

$$H = f(T, S). \tag{3.4}$$

Henry's Law is valid for the dissolution of a gas in a liquid phase only at low solute mole fractions (e.g. ATKINS (2001) [10]). As CO_2 sequestration takes place at relatively high pressures this approach leads to errors that are discussed below.

- **Approach by Duan & Sun:** DUAN & SUN (2003) [33] proposed a model for the description of the mutual solubilities of CO_2 and water. Their equations are based on a specific particle interaction theory for the water and an equation of state for the CO_2 phase where they include salinity effects on the dissolution behavior. A large data set taken from the literature is used for the parameterization. The model is compared to these data to prove its validity at temperatures between 273 and 533 K, pressures of up to 2000 bar, and salinities of a molality of up to 4.3 mol/kg (this corresponds to a salt mass fraction of approximately $S = 0.2$ kg/kg).

- **Equation of State:** Following the work of WENDLAND (1994) [103] and ADRIAN ET AL. (1998) [8] a cubic equation of state for the system CO_2-water is used. A modified

Peng-Robinson equation of state after MELHEM ET AL. (1989) [72] with the mixing rule of HURON & VIDAL (1979) [57] is used (cf. Appendix B.1 and B.2). With this equation of state it is possible to describe phase equilibria and therefore the dissolution of carbon dioxide in pure water. This is considered to be a very exact description of the solubility because the parameters required for the equation of state are directly fitted to experimental data and represent them very well. Therefore, the EOS is considered as the reference for the solubilities.

Figure 3.2 shows the different approaches to describing CO_2 solubility in pure water at a temperature of $34\,°C$ and a pressures range from 0 to $200\,bar$. It is obvious from a comparison of the curves that the Henry approach overestimates CO_2 solubilities significantly at pressures higher than $30\,bar$. The equations proposed by DUAN & SUN almost coincide with the reference EOS given by WENDLAND. As DUAN & SUN also include the influence of salinity on CO_2 dissolution, their approach is used in the further course of this study.

Figure 3.2: Comparison of different models for the computation of CO_2 solubility in pure water depending on pressure at a temperature of T=34 °C. The approaches by BATTISTELLI ET AL. (1997) [16], DUAN & SUN (2003) [33], and ADRIAN ET AL. (1998) [8] (EOS) are depicted. The graphs resulting from the latter two lie on top of each other.

Figures 3.3 and 3.4 (pages 41 and 42) show the dissolution of CO_2 in the water phase at different temperatures, pressures, and salinities. As mentioned before, the amount of dissolved CO_2 increases with increasing pressure and decreasing temperature and salinity. Note the strong influence of salinity on CO_2 dissolution. This effect has to be taken into account explicitly as the formation fluids in deep aquifers are often highly saline.
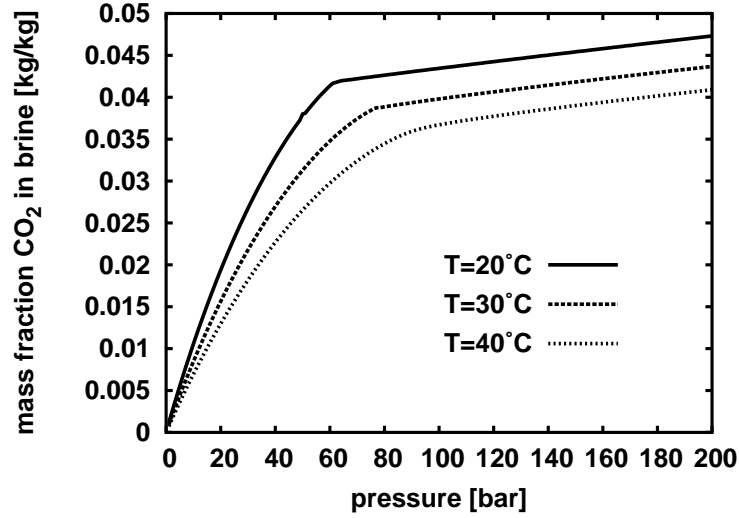
Figure 3.3: Solubility of CO_2 in brine depending on pressure at different temperatures and a constant salinity of S=0.1 kg/kg (DUAN & SUN (2003) [33]).

Table 3.3 (page 41) shows characteristic values of dissolved carbon dioxide in water and brine at different pressures, temperatures, and salinities. These values are maximum concentrations at given pressure, temperature, and salinity if sufficient CO_2 is present, i.e. a CO_2 phase can be observed.

Table 3.3: Characteristic values for CO_2 solubility and fluid properties of CO_2 and brine.

Case	T	p	S	X_w^{CO2}	c_{CO2}	ϱ_{CO2}	μ_{CO2}	ϱ_b	μ_b
	[°C]	[bar]	[-]	[kg/kg]	[kg/m³]	[kg/m³]	[Pa s]	[kg/m³]	[Pa s]
1	10	1	0	0.002	2.2	1.88	$1.42 \cdot 10^{-5}$	999.7	$1.31 \cdot 10^{-3}$
2	40	100	0.25	0.020	23.5	628.61	$7.58 \cdot 10^{-5}$	1180.9	$1.25 \cdot 10^{-3}$
3	70	100	0.25	0.016	19.2	247.77	$2.77 \cdot 10^{-5}$	1159.8	$0.77 \cdot 10^{-3}$
4	70	200	0.25	0.021	24.6	659.05	$8.30 \cdot 10^{-5}$	1162.9	$0.77 \cdot 10^{-3}$

Case 1: groundwater, close to surface,
Case 2: saline aquifer, 1000 m,
Case 3: saline hot aquifer, 1000 m,
Case 4: very deep injection, 2000 m.

Dissolution of water in CO_2: DUAN & SUN proposed Dalton's Law for describing water
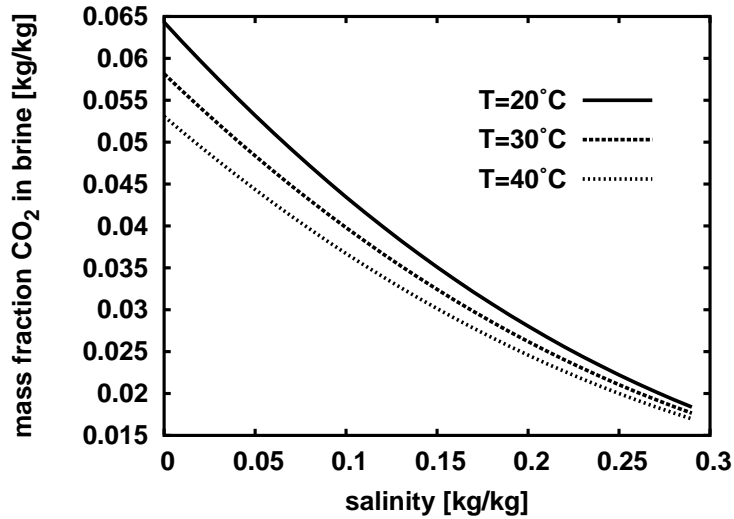
Figure 3.4: Solubilities of CO_2 in brine depending on salinity at different temperatures and a constant pressure of $p=100\,$bar (DUAN & SUN (2003) [33]).

contents in the CO_2 phase:

$$x^{\mathrm{w}}_{\mathrm{CO2}} = \frac{p_{\mathrm{wsat}}}{p_{\mathrm{CO2}}}. \tag{3.5}$$

Here, the mole fraction of water in the CO_2-rich phase $x^{\mathrm{w}}_{\mathrm{CO2}}$ is equal to the ratio of the saturation vapor pressure of water p_{wsat} and the pressure of the CO_2-rich phase p_{CO2}. The equilibrium vapor pressure of the one-component system water is denoted by p_{wsat}. It depends only on temperature and is assumed to be equal to the partial pressure of water vapor in a multi-component system if a liquid water phase is present. The components are considered to be ideal, i.e. there are no interactions between the molecules of the different components. This assumption is only valid at low pressures.

Figure 3.5 (page 43) shows the effect of increasing pressure on the dissolution of water in the CO_2-rich phase where the approach discussed above and the reference equation of state given by ADRIAN ET AL. (1998) [8] are compared. At relatively low pressures of up to 50 bar, the results from equation (3.5) match fairly well, at higher pressures mass contents are underestimated significantly. Therefore, using the equation of state to describe the dissolution of water in the CO_2-rich phase properly is recommended.

With the EOS given by ADRIAN ET AL. (1998) [8], it is possible to describe the amount of water dissolved in the CO_2-rich phase correctly. For simplicity's sake, however, the solubility of water in CO_2 is neglected in the further course of this study. This can be done on the basis of the following arguments:
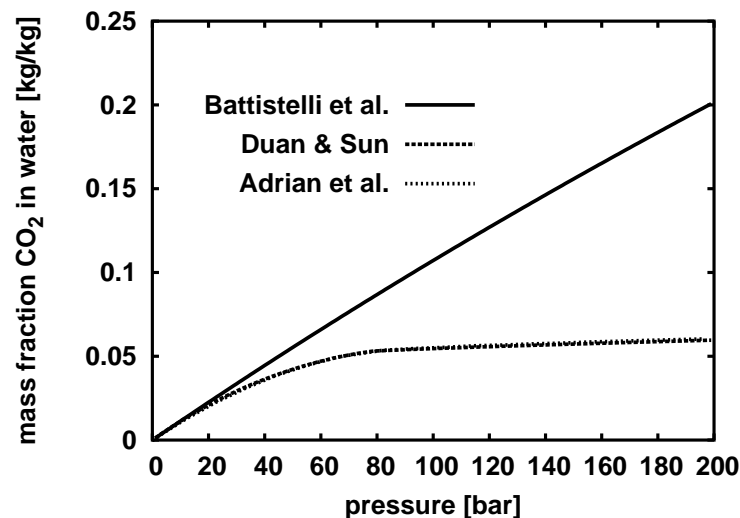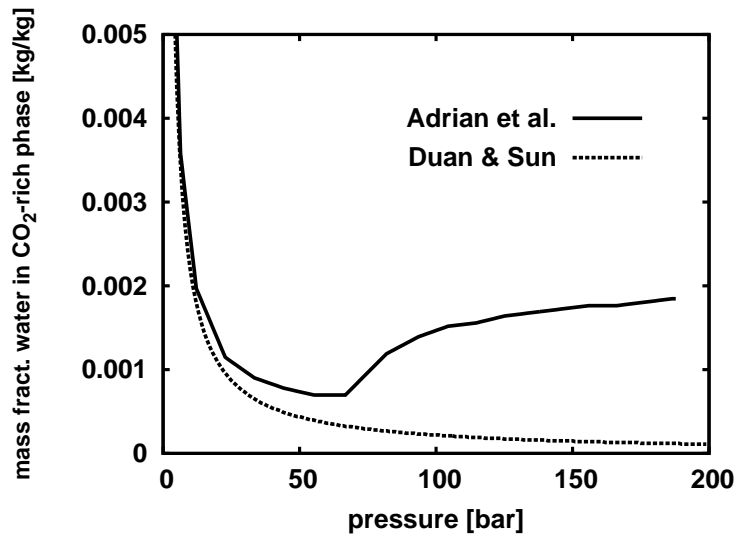
Figure 3.5: Comparison of different models for the computation of water solubility in CO_2 depending on pressure at a temperature of $T=34\,°C$. Approaches proposed by DUAN & SUN (2003) [33] and ADRIAN ET AL. (1998) [8] (EOS) are shown.

- Figure 3.5 shows that the water mole fraction in the CO_2-rich phase is lower than 0.2 mass percent even at high pressures. These very low concentrations are at least one order of magnitude smaller than the amount of CO_2 in the water-rich phase and are therefore assumed to be negligible.

- A small amount of water in the CO_2-rich phase does not necessarily imply small impact on CO_2 fluid properties. However, only few approaches to the change of CO_2 properties due to dissolved water can be found in literature. The development and implementation of such descriptions are beyond the scope of this work.

Therefore, in this study, water contents in the CO_2-rich phase is set to zero:

$$X_{CO2}^{w} = x_{CO2}^{w} = 0. \tag{3.6}$$

3.2 CO_2 fluid properties

Figure 3.6 (page 45) shows the phase diagram of pure CO_2 as a pure fluid and depicts the different states of aggregation as a function of temperature and pressure. The temperature and pressure conditions expected for CO_2 sequestration range between 10 and $80\,°C$ and 1 and $200\,bar$, respectively. Therefore, gaseous, liquid, and supercritical CO_2 can occur at different depths.

Here, the supercritical state is defined when pressure and temperature both exceed the critical values. The dashed lines in Figure 3.6 separating the supercritical from the gaseous and liquid states does not indicate any physical discontinuities. Thermodynamic properties, e.g. density and viscosity, change continuously when crossing from the liquid or gaseous to the supercritical state. For example, the density of liquid CO_2 reduces with increasing temperature at constant pressure. If, in this case, pressure is supercritical and temperature changes from sub- to supercritical, the carbon dioxide density will continuously decrease; only the state of aggregation changes from liquid to supercritical.

Variations in temperature or pressure crossing the vapor pressure curve (liquid-gas coexistence line) lead to discontinuities in fluid properties, because the state of aggregation changes from liquid to gaseous or vice versa and properties can therefore change by orders of magnitude. Thus, T, p-changes close to the critical point result in strong property differences as well.

The critical data of CO_2 given by SPAN & WAGNER (1996) [96] are presented in Table 3.4. Characteristic CO_2 densities and viscosities at conditions relevant for CO_2 sequestration are displayed in Table 3.3. Note that CO_2 densities reach liquid-like values when conditions change from low pressures and temperatures to supercritical values. In contrast, CO_2 viscosities, even though increasing with pressure, remain gas-like. In geological formations deeper than approximately 800 m, carbon dioxide will behave as a dense liquid with gas-like viscosity.

Table 3.4: Critical properties of CO_2 (SPAN & WAGNER (1996) [96]) and of water (WAGNER & PRUSS (2002) [101]).

		CO_2	water
critical pressure	p_{crit}	73.8 bar	220.64 bar
critical temperature	T_{crit}	304.1 K = 30.95 °C	647.1 K = 373.95 °C
critical density	ϱ_{crit}	467.6 kg/m³	322.0 kg/m³

3.2.1   Density

The high precision EOS of SPAN & WAGNER (1996) [96] is used for the CO_2 density. Figure 3.7 (page 46) shows how CO_2 density varies with pressure and temperature. Note the sudden density increase as gaseous CO_2 changes into the liquid or supercritical state.

At 20 °C, the vertical line represents a discontinuous density change at the corresponding vapor pressure. A small pressure increase from slightly below to slightly above vapor pressure
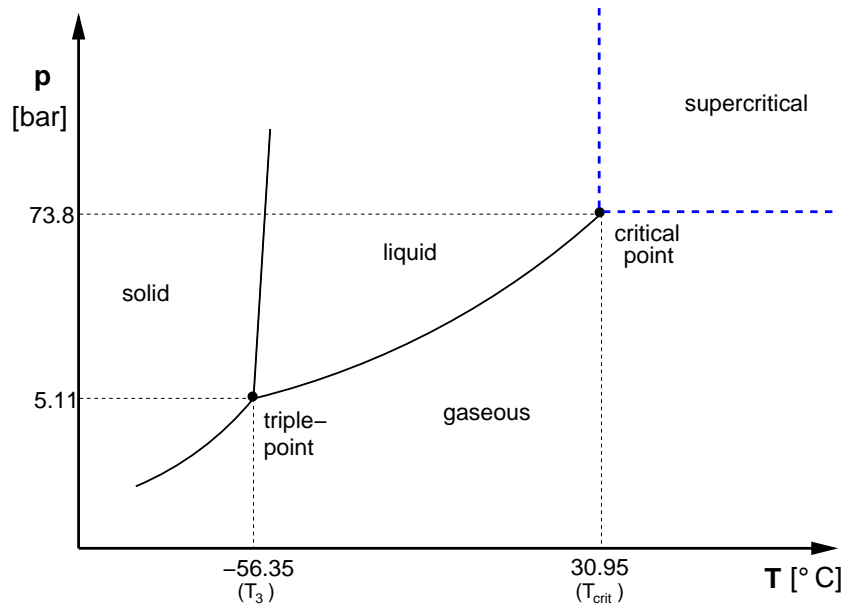
Figure 3.6: Phase diagram of CO_2.

(in this case 57.33 bar) will change the CO_2 state from gaseous to liquid. At 40 °C, the temperature is supercritical and density increases continuously with increasing pressure with larger gradients around the critical pressure. At higher temperatures, the influence of the critical point diminishes and the density changes with respect to a certain pressure difference become smaller.

3.2.2 Enthalpy

CO_2 enthalpy is obtained using the approach suggested by SPAN & WAGNER (1996) [96]. Figure 3.8 (page 46) shows the enthalpy as a function of pressure for different temperatures. The picture illustrates the enthalpy change relative to a reference state of $h = 0 \, \text{kJ/kg}$ at $p_{CO2} = 1.013 \, \text{bar}$ (1 atmosphere) and $T = 0 \, °C$. It is necessary to add an enthalpy difference of 21.91 kJ/kg to obtain the results of the SPAN & WAGNER equation, because they use a different reference state. This causes a constant offset of the enthalpy curves, enthalpy differences are unaffected. The CO_2 reference state has to be the same as the one used for brine enthalpy (cf. Section 3.3.2) in order to quantify the enthalpy change due to dissolved CO_2 correctly.

The 10 °C and 20 °C curves of Figure 3.8 show gaseous and liquid CO_2 for low and high pressures, respectively. As the volume change from gaseous to liquid is large, a jump in specific enthalpy can be observed, which is the specific enthalpy of evaporation. Above
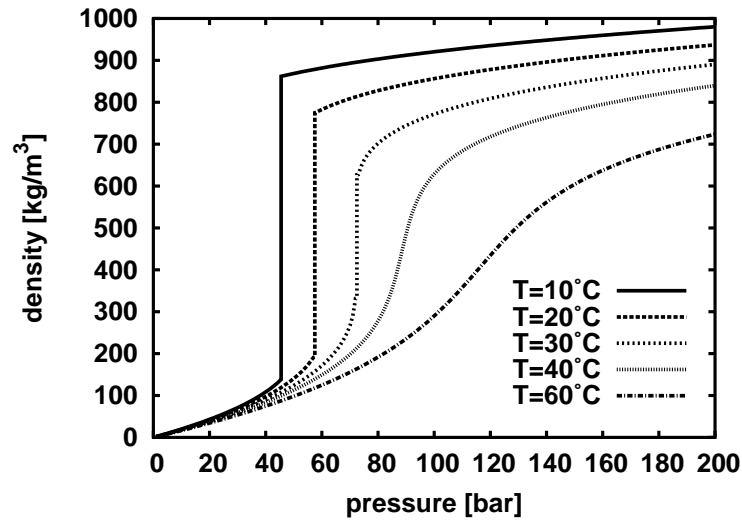
Figure 3.7: Density of CO_2 as a function of pressure at various temperatures using the correlations of SPAN & WAGNER (1996) [96].

critical temperature ($T_{\text{crit}} = 30.95\,°C$), no enthalpy discontinuity can be observed, because no phase change takes place. Here, the enthalpy continuously decreases as density rises at constant temperature and increasing pressure.
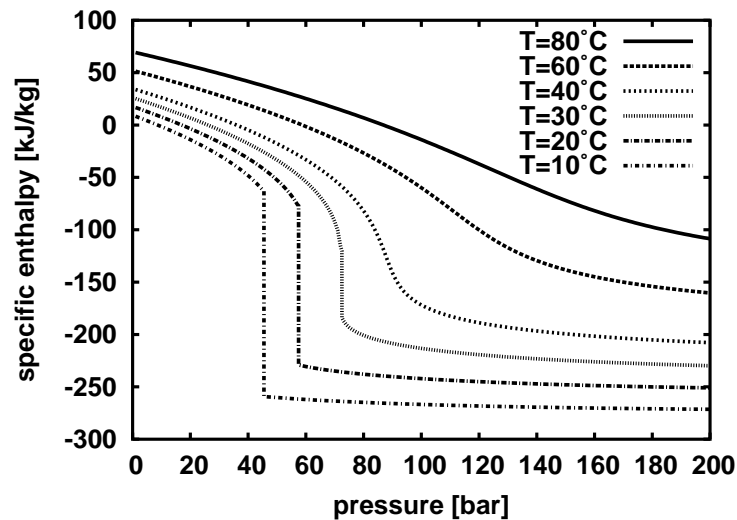
Figure 3.8: Specific enthalpy of CO_2 applying the the correlations given by SPAN & WAGNER (1996) [96].

3.2.3 Viscosity

Figure 3.9 (page 47) shows the dynamic viscosity from an equation by FENGHOUR ET AL. (1998) [39]. The typical curves observed for the density can also be seen with significant changes around the critical point and when the vapor pressure curve is crossed. The viscosity of a gas increases with temperature while that of a liquid and a supercritical fluid decreases with rising temperature. Consequently, the viscosity isotherms in Figure 3.9 cross.
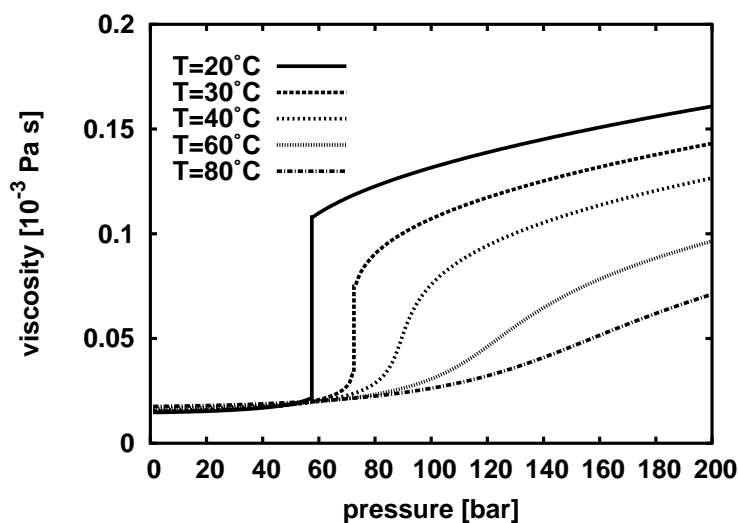
Figure 3.9: Viscosity of CO_2 as a function of pressure at various temperatures using the correlations proposed by FENGHOUR ET AL. (1998) [39].

3.3 Water and brine fluid properties

Critical properties of pure water are shown in Table 3.4 (page 44). The critical temperature is almost $300\,°C$ higher and the critical pressure is somewhat higher than the underlying model assumptions (cf. Table 3.1) which are to be expected during CO_2 sequestration. Therefore, pure water is always in the liquid state here. As described in Section 3.1.2, mass transfer of water into the CO_2 phase is also neglected; thus, all water mass is confined to the liquid phase in the present model. Characteristic properties of water and brine at the conditions prevailing during CO_2 sequestration are compiled in Table 3.3 (page 41).

3.3.1 Density

Brine density (ϱ_b) is described as the sum of pure water density (ϱ_w) which is a function of temperature and pressure as well as the contributions of salinity and dissolved CO_2:

$$\varrho_\mathrm{b} = \varrho_\mathrm{w}(T,p) + \Delta\varrho(S) + \Delta\varrho(T,p,X_\mathrm{b}^{\mathrm{CO2}}). \tag{3.7}$$

The IAPWS formulation (1997) [58] is used for pure water density which is a very high precision representation. Following the recommendations of ADAMS & BACHU (2002) [7], an approach suggested by BATZLE & WANG (1992) [17] is chosen to take into account the effect of salinity on brine density. GARCIA (2001) [41] proposed a correlation which includes the effect of dissolved CO_2 on brine density. Note that brine density increases with increasing amount of dissolved CO_2.

Figure 3.10 (page 49) shows the density of pure water, brine (S=0.25), and brine with dissolved CO_2 ($X_\mathrm{b}^{\mathrm{CO2}}$=0.02) as a function of temperature. Increasing temperature leads to decreasing density for all liquids here. Furthermore, there is a more significant salinity effect as the salt content can increase the brine density by more than 20 %. This is illustrated in Figure 3.11 (page 50) where brine density as a function of salt content is depicted at different temperatures. Dissolved carbon dioxide increases brine density by only 1-2 %.

Liquid water and brine are almost incompressible (cf. values in Table 3.3, page 41); the pressure effect on density is therefore weak, but is considered in the equations.

3.3.2 Enthalpy

Brine enthalpy is calculated by taking into account pressure and temperature effects as well as the influence of salinity and dissolved CO_2. The enthalpy of brine can be calculated from the weighted contributions of the three components pure water, salt, and CO_2 in accordance with equation (3.8). Here, the enthalpy of dissolution ($\Delta_L h$, heat of dissolution) of salt and CO_2 in water is considered.

$$
\begin{aligned}
h_\mathrm{brine} = \quad & \underbrace{(1 - X_\mathrm{b}^{\mathrm{NaCl}} - X_\mathrm{b}^{\mathrm{CO2}}) \cdot h_\mathrm{w}(T,p)}_{\text{pure water enthalpy}} \\
+ \quad & \underbrace{X_\mathrm{b}^{\mathrm{NaCl}} \cdot h_\mathrm{NaCl}(T) + X_\mathrm{b}^{\mathrm{NaCl}} \cdot (\Delta h_L(T))_\mathrm{NaCl}}_{\text{salt contribution}} \\
+ \quad & \underbrace{X_\mathrm{b}^{\mathrm{CO2}} \cdot h_\mathrm{CO2}(T,p) + X_\mathrm{b}^{\mathrm{CO2}} \cdot (\Delta h_L(T))_\mathrm{CO2}}_{\text{CO}_2 \text{ contribution}} .
\end{aligned} \tag{3.8}
$$

Pure water enthalpy is described using the IAPWS formulation (1997) [58] as a function of temperature and pressure. The effect of dissolved salt on brine enthalpy (including heat
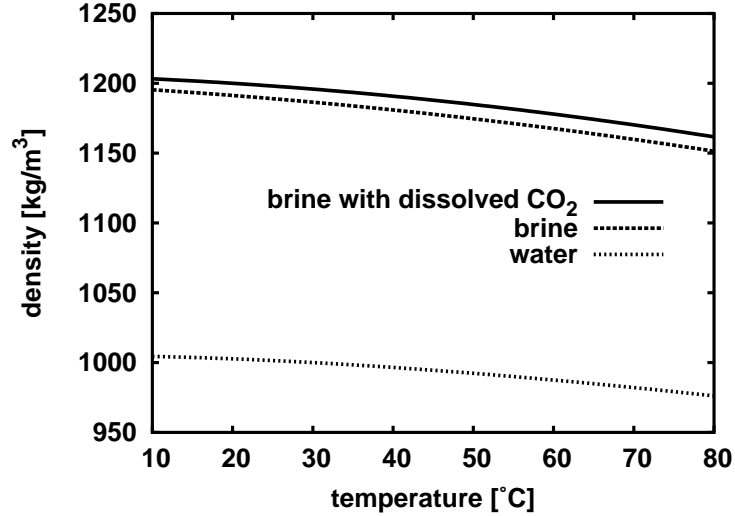
Figure 3.10: Water and brine density as a function of temperature at a pressure of 100 bar. Dotted line: pure water density (IAPWS (1997) [58]). Dashed line: brine density at a salinity of $S = 0.25$ kg/kg (BATZLE & WANG (1992) [17]). Solid line: brine of same salinity with dissolved CO_2 (GARCIA (2001) [41] ($X_b^{CO2} = 0.02$ kg/kg)).

of dissolution) is taken into account using the approach of MICHAELIDES (1981) [74]. The specific enthalpy of salt is calculated from its specific heat capacity c with $0\,°C$ as the reference temperature:

$$h = u = \int_T c(T)dT. \tag{3.9}$$

An assumption for equation (3.9) is that $pV = 0$ and specific enthalpy is thus equal to specific internal energy u, which is also reasonable for the phase change from solid to liquid. Correlations for the heat capacity of salt are taken from DAUBERT & DANNER (1989) [32].

Salt enthalpy changes are smaller than water enthalpy changes and salt dissolution in water is an endothermic reaction (the dissolution process causes a cooling of the fluid). Therefore, both terms that correspond to the salt effect in equation (3.8) reduce brine enthalpy. Figure 3.12 (page 50) shows that a salt mass fraction of $S = 0.25$ kg/kg yields a considerably lower enthalpy for brine than for pure water.

Brine enthalpy change caused by dissolved CO_2 is considered by computing the energy content of the CO_2 in the water phase using the approaches described in Section 3.2.2. The dissolution of CO_2 in water is an exothermic reaction at the relevant temperatures (10-80 $°C$), i.e. CO_2 dissolution causes a warming of the solution and brine enthalpy rises. The enthalpy change (heat of dissolution) is taken into account following the suggestions of DUAN & SUN (2003) [33].
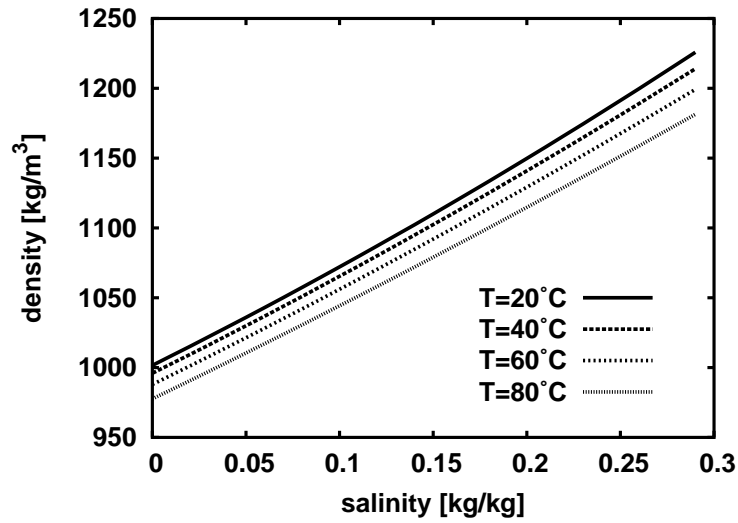
Figure 3.11: Brine density as a function of salinity at different temperatures and at a pressure of $p = 100\,\text{bar}$.

Figure 3.12 shows the small influence of dissolved CO_2 on brine enthalpy even for a relatively high carbon dioxide content. For this reason, the CO_2 effect on brine enthalpy is neglected here.
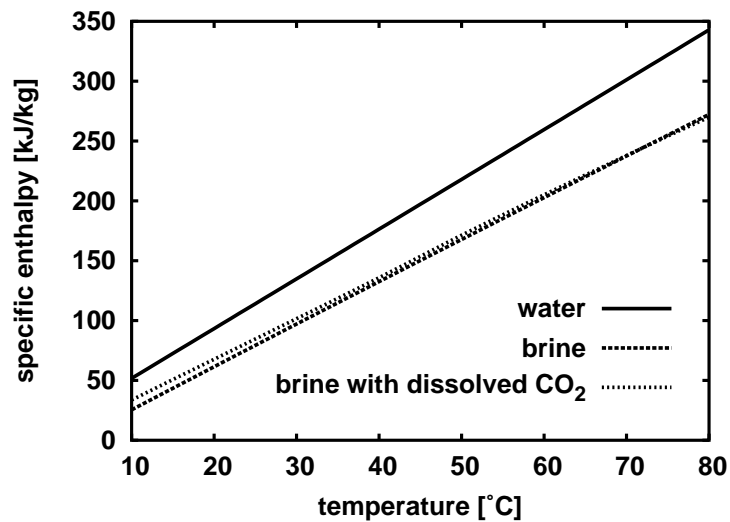
Figure 3.12: Brine enthalpy as a function of temperature at a pressure of $p = 100\,\text{bar}$, a salinity of $S = 0.25\,\text{kg/kg}$, and an amount of dissolved CO_2 of $X_{\text{b}}^{\text{CO2}} = 0.05\,\text{kg/kg}$.

3.3.3 Viscosity

Brine viscosity is calculated with the equations given by BATZLE & WANG (1992) [17]. Dynamic viscosity is expressed as a function of temperature and salinity, the pressure influence is small and assumed to be negligible. Figure 3.13 (page 51) shows the temperature dependence for water and brine with a salinity of $S = 0.25\,\mathrm{kg/kg}$ at a pressure of $100\,\mathrm{bar}$. Increasing salinity leads to a more viscous fluid while increasing temperature reduces viscosity. Pure water viscosity in Figure 3.13 is obtained from the IAPWS formulation (1997) [58].
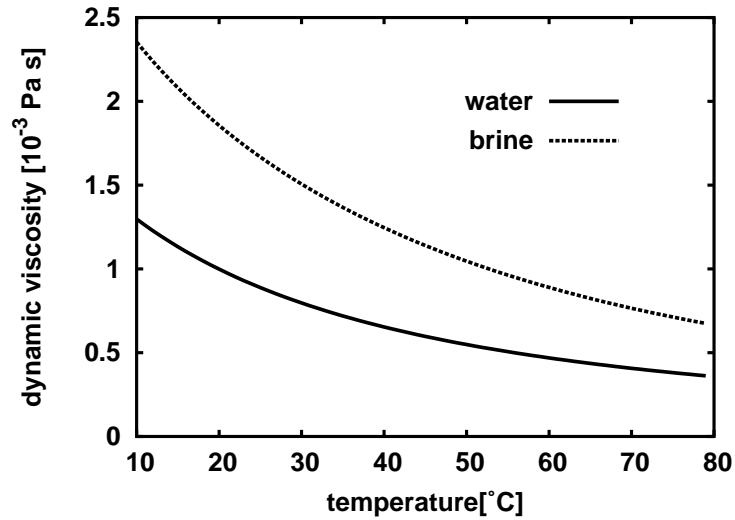
Figure 3.13: Water and brine viscosity as a function of temperature at a pressure of $p = 100\,\mathrm{bar}$ and a salinity of $S = 0.25\,\mathrm{kg/kg}$.

Table 3.5: Fluid properties of brine and CO_2.

Section	Fluid property	Function of	Literature
3.2.1	CO_2 density ϱ_{CO2}	$f(T, p)$	[96]
3.2.2	CO_2 enthalpy h_{CO2}	$f(T, p)$	[96]
3.2.3	CO_2 viscosity μ_{CO2}	$f(T, p)$	[39]
3.3.1	Brine density ϱ_b	$f(T, p, S, X_w^{CO2})$	[58, 17, 41]
3.3.2	Brine enthalpy h_b	$f(T, p, S, X_w^{CO2})$	[58, 74, 32, 33]
3.3.3	Brine viscosity μ_b	$f(T, S)$	[17]

3.4 Relevant flow and transport processes

In this section, the main driving forces for the relevant flow and transport of CO_2 in the subsurface are discussed and put into the context of the model concept used in this study. Figure 3.14 (page 53) illustrates the main processes that take place during CO_2 sequestration in geological formations, namely advection, buoyancy, and diffusion. Moreover, heat conduction and capillary effects play an important role.

Advective flow caused by viscous forces takes place mainly close to the injection well where pressure is exerted and hence pressure gradients cause relatively high fluid velocities. Natural groundwater flow is advective and influences the long-term CO_2 plume propagation in the subsurface.

Buoyancy due to gravitational forces plays an important role when CO_2 is injected into the subsurface because carbon dioxide has a lower density than formation brine under all thermodynamically relevant conditions. Therefore, an upward migration of CO_2 takes place.

Both advection and buoyancy are considered in the model presented here using Darcy's Law as described in Section 2.6.1. Thermal energy that is transported with the flowing phases is also taken into account in the model; this is called *thermal convection.*

Diffusion is a much slower process than advection and buoyancy, but has to be taken into account when considering the long-term behavior of the CO_2 in the subsurface. For example, one key question is how long the CO_2 plume will stay in the formation as a separate phase until it is entirely dissolved in the formation water. This can only be answered by taking dissolution and diffusive transport into consideration. In this model, carbon dioxide dissolves in brine and is then transported due to diffusion. For this, a Fickian approach described in Section 2.5.3 is used.

Simple back-of-the-envelope calculations for relevant velocities and time scales of advection, buoyancy, and diffusion are given in Appendix C.

Heat conduction (Section 2.5.5) depends linearly on the heat conductivity of the material. On the assumption of local thermal equilibrium (cf. Section 2.6.2), it is possible to derive a local heat conductivity of the porous medium λ_{pm} depending on CO_2 and water (brine) saturation. Following the investigations of EBIGBO (2005) [34], the approach proposed by SOMERTON ET AL. (1974) [95] is used:

$$\lambda_{pm} = \lambda_{pm}^{S_w=0} + \sqrt{S_w}(\lambda_{pm}^{S_w=1} - \lambda_{pm}^{S_w=0}). \tag{3.10}$$

Figure 3.15 (page 54) depicts the strong increase of the heat conductivity at small water saturations.
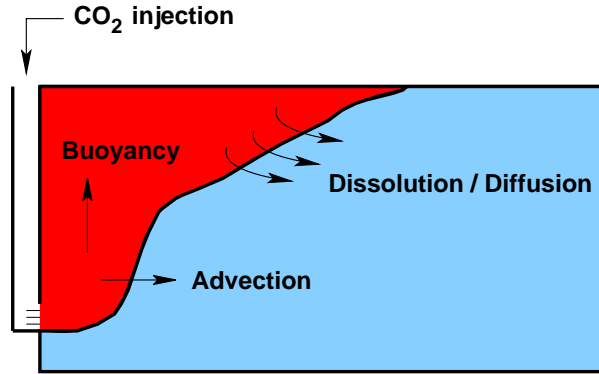
Figure 3.14: Relevant transport processes of CO_2.

Capillary forces: In Sections 2.5.6 and 2.6.4, capillarity phenomena and the macroscale inclusion of capillary pressures into a multi-phase model concept are described. The practical relevance of capillary pressures becomes clear when considering Figure 3.16 (page 54). Here, the interface between two geological layers of different properties is shown. Ω^I and Ω^{II} can be interpreted as the CO_2 storage reservoir and cap-rock, respectively. The capillary pressure-saturation relationships of the two different materials are depicted and the cap-rock with its low permeability yields significantly higher capillary pressures than the reservoir. If CO_2 reaches the interface between Ω^I and Ω^{II}, it has to pool up because, before it can enter the less permeable layer, the entry pressure has to be overcome. A saturation of S_1 must be reached in the reservoir before the CO_2 can enter the largest pore of the cap-rock. Thus, when the advective and buoyancy flow of CO_2 are calculated, considering the capillary pressures rather than just the different permeabilities and porosities of the geological layers makes a difference. This is a reduction of the carbon dioxide entering the cap-rock, because the capillary entry pressure has to be exceeded.

The model concept includes the consideration of capillary pressure-saturation relationships. It is possible to use different approaches for the dependence of p_c on S_w, e.g. those suggested by BROOKS & COREY (1964) [20] and VAN GENUCHTEN (1980) [44]. Note that when these functions are applied, one assumption is always that CO_2 is the non-wetting and brine the wetting phase.

Other processes: Dispersion as described in Section 2.5.4 is not considered in the model concept of the present work. The reason for neglecting this process is that no appropriate way of quantifying mechanical dispersion for the multi-phase system CO_2 water is available.

Another important process, especially with respect to the long-term processes caused by CO_2 sequestration, is the chemical reactions with the matrix, i.e. the reservoir rock. This would lead to a different research field and is not aim of this work.
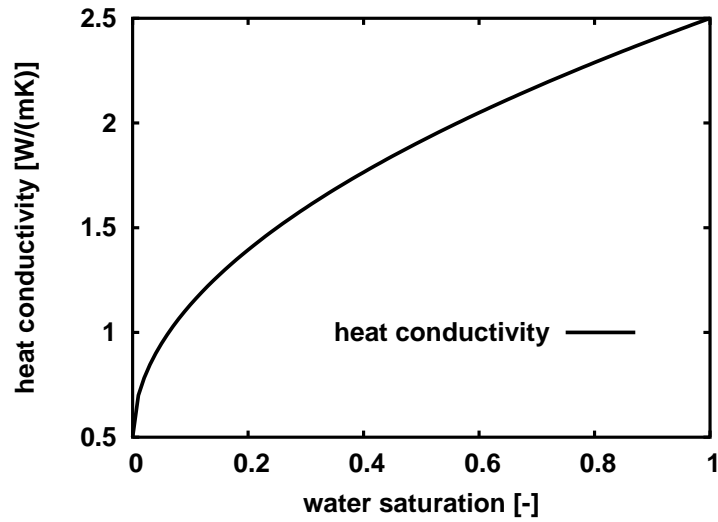
Figure 3.15: Heat conductivity of the porous medium changing with water saturation (SOMERTON ET AL. (1974) [95]).
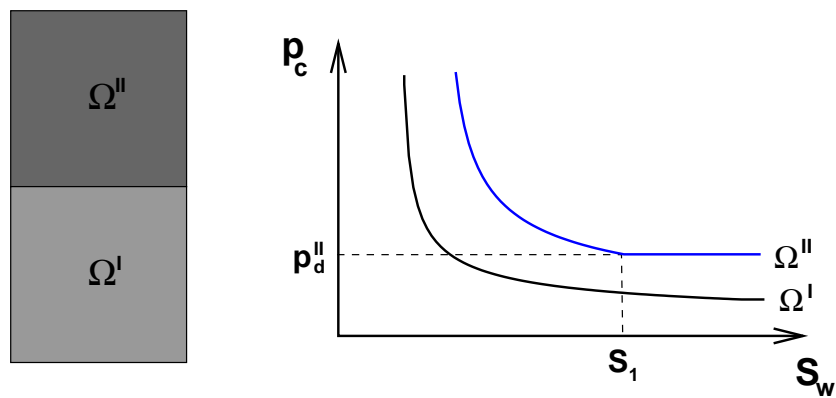
Figure 3.16: Capillary pressure at the interface between two geological layers. In Ω^I the saturation S_1 has to be reached for a non-wetting phase to enter Ω^{II} from below (the entry pressure p_d^{II} has to be overcome).

Chapter 4

Mathematical and numerical model

4.1 Mathematical Model

4.1.1 Conservation of mass, momentum and energy

To describe non-isothermal multi-phase multi-component flow and transport processes in porous media comprehensively, it is necessary to formulate balance equations for mass, momentum, and energy. An elegant approach to this problem is to introduce *Reynold's transport theorem*, which considers the change of a system depending on any kind of extensive fluid property (cf. Section 2.1.2). In this section, the theorem will be explained and applied to the quantities mass, momentum, and energy.

Reynold's transport theorem

In a system with volume G, the total amount of any extensive fluid property E_{sys} is

$$E_{\mathrm{sys}} = \int_G \varrho\, \varepsilon\, dG \tag{4.1}$$

where ε is the appropriate intensive property (per unit mass (m))

$$\varepsilon = \frac{d(E_{\mathrm{sys}})}{dm}. \tag{4.2}$$

To describe flow in the system G, a Eulerian approach is chosen and an integral conservation equation which is valid for any control volume V is formulated. V corresponds to the mentioned system of constant size ($dV/dt = 0$). The temporal change of the extensive fluid property is described by Reynold's transport theorem (e.g. HELMIG & CLASS (2005) [50]

or SHAUGHNESSY ET AL. (2005) [90]):

$$\frac{dE_{\text{sys}}}{dt} = \int\limits_{V} \frac{\partial}{\partial t}(\varrho\,\varepsilon)\,dV + \oint\limits_{\partial V} (\varrho\,\varepsilon)(\mathbf{v}\cdot\mathbf{n})\,d\partial V. \tag{4.3}$$

Here, the first term is a volume integral that includes the changes of the property in the control volume with time. This part of the equation accounts for the storage or accumulation of quantity ε and it is thus called *storage* or *accumulation* term. The second term takes into account the fluxes over the surface of the control volume ∂V.

Conservation of mass

To apply Reynold's transport theorem to mass, $E_{\text{sys}} = m$ is chosen and the intensive property is $\varepsilon = 1$. Furthermore, mass is conserved[1] such that

$$\frac{dE_{\text{sys}}}{dt} \overset{!}{=} 0. \tag{4.4}$$

This yields the integral form of the mass balance equation without the consideration of sources or sinks:

$$\int\limits_{V} \frac{\partial\varrho}{\partial t}\,dV + \oint\limits_{\partial V} \varrho\,(\mathbf{v}\cdot\mathbf{n})\,d\partial V = 0. \tag{4.5}$$

After the Green-Gaussian integral rule is applied to the flux term $\mathbf{F} = \varrho\mathbf{v}$

$$\int\limits_{V} \nabla\cdot\mathbf{F}\,dV = \oint\limits_{\partial V} \mathbf{F}\cdot\mathbf{n}\,d\partial V \tag{4.6}$$

the surface integral is replaced by a volume integral and equation (4.5) is rewritten as

$$\int\limits_{V} \frac{\partial\varrho}{\partial t}\,dV + \int\limits_{V} \nabla\cdot(\varrho\mathbf{v})\,dV = 0. \tag{4.7}$$

On the assumption that the integrands are continuous, the mass balance equation can be written in differential form:

$$\frac{\partial\varrho}{\partial t} + \nabla\cdot(\varrho\mathbf{v}) = 0. \tag{4.8}$$

Conservation of momentum

If momentum ($\mathbf{p} = m\cdot\mathbf{v}$) is selected as the extensive system variable E_{sys}, the corresponding intensive variable is $\varepsilon = \mathbf{v}$. According to Newton's Second Law, the change of momentum in a system is caused by external forces:

$$\frac{dE_{\text{sys}}}{dt} = \frac{d\,\mathbf{p}_{\text{sys}}}{dt} = \sum \mathbf{f}_{\text{ext}}. \tag{4.9}$$

---

[1]Conservation of mass applies since nuclear or relativistic processes are not considered.

Inserting this in Reynold's transport theorem yields

$$\int_V \frac{\partial}{\partial t}(\varrho \mathbf{v}) \, dV + \oint_{\partial V} (\varrho \mathbf{v})(\mathbf{v} \cdot \mathbf{n}) \, d\partial V = \sum \mathbf{f}_{\text{ext}}. \tag{4.10}$$

Applying the Green-Gaussian integral rule, writing the equation in differential form and assuming that the only external force acting is gravity, yields

$$\frac{\partial(\varrho \mathbf{v})}{\partial t} + \nabla \cdot (\varrho \mathbf{v} \cdot \mathbf{v}) = \varrho \mathbf{g}. \tag{4.11}$$

Equation (4.11) describes the momentum balance of any fluid on the microscale under the given assumptions. When fluid flow in a porous medium on the macroscale is considered, it is valid to use Darcy's Law (equation (2.27)) for the momentum balance (under the conditions mentioned in Section 2.6.1). It gives an expression for the flow velocity of the fluid. This is advantageous, because the Darcy velocity is given explicitly and can be inserted into the mass balance equation (cf. equation (4.1.2)).

Conservation of energy

The first law of thermodynamics states that energy is conserved, i.e. energy can be transformed from one form to another, but it cannot be destroyed. In a closed system[2], this means that the change of internal energy U within a certain time dt results from the in- or outflux of heat Q or from work W that has been done:

$$dU = \partial Q + \partial W. \tag{4.12}$$

According to Reynold's transport theorem, internal energy is the extensive system variable $E_{\text{sys}} = U$. The corresponding intensive quantity is $\varepsilon = u$, i.e. specific internal energy. Applying this to Reynold's transport theorem leads to

$$\frac{dU}{dt} = \int_V \frac{\partial(u\varrho)}{\partial t} \, dV + \oint_{\partial V} (u\varrho)(\mathbf{v} \cdot \mathbf{n}) \, d\partial V = \dot{Q} + \dot{W} \tag{4.13}$$

where $\dot{Q}$ is the heat flux per time unit and $\dot{W}$ the work per time unit (power). Heat fluxes over the system's boundaries can take place due to radiation Q_{rad}, which can be neglected in the subsurface due to small temperature gradients, and heat conduction Q_{cond}:

$$\frac{dQ}{dt} = \dot{Q}_{\text{cond}} = - \oint_{\partial V} (\dot{q} \, \mathbf{n}) \, d\partial V, \tag{4.14}$$

where $\dot{q}$ is the heat flux density. By definition, the normal vector $\mathbf{n}$ points outwards of the boundaries of the control volume under consideration, but an influx of heat adds internal

---

[2]A closed system permits energy flow but no mass transfer over its boundaries.

energy. Therefore, the minus sign has to be included. Heat flux density can be described by Fourier's Law, which is explained in Section 2.5.5 (equation (2.23)):

$$\dot{q} = -\lambda \, \nabla T.$$

The internal energy of the system can be changed due to volume changing work W_{vol} and dissipative work W_{diss}. As flow velocities are small, dissipation can be neglected and only volume changing work is considered. Thus, the power (i.e. work per time) can be expressed as

$$\dot{W}_{\text{vol}} = \frac{dW}{dt} = - \oint_{\partial V} (\dot{\omega} \, \mathbf{n}) \, d\partial V \tag{4.15}$$

where $\dot{\omega}$ is the power density. Power density is considered the work per time unit with respect to the surface of the control volume. The volume changing work describes the work carried out on the system by the change of its volume at constant pressure (e.g. LÜDECKE & LÜDECKE (2000) [68]) and is given by

$$W_{\text{vol}} = -p \, dV. \tag{4.16}$$

The power density is

$$\dot{\omega} = pv. \tag{4.17}$$

This becomes obvious when the problem is reduced to one dimension; the volume changing work with respect to time is then

$$\dot{W}_{\text{vol}} = \frac{d}{dt}(-p \, dV) = -pA\frac{ds}{dt} = -pvA \tag{4.18}$$

where A is the surface area, s the length that describes the volume change and v the velocity with which the volume change takes place. The right-hand side of the equation is negative to notify that a negative volume change (compression) adds internal energy to the system.

Inserting equations (4.14) and (4.15) into (4.13) and applying the Green-Gaussian integral rule yields an integral form of the energy balance equation:

$$\frac{dU}{dt} = \int_V \frac{\partial(u\varrho)}{\partial t} \, dV + \int_V \nabla \cdot (u\varrho\mathbf{v}) \, dV = \int_V \nabla \cdot (\lambda\nabla T) \, dV - \int_V \nabla \cdot (p\mathbf{v}) \, dV. \tag{4.19}$$

The terms can be rearranged and written in differential form. Furthermore, the specific enthalpy $h = u + p/\varrho$ is introduced (cf. Section 2.2.2).

$$\frac{\partial(u\varrho)}{\partial t} + \nabla \cdot (u\varrho\mathbf{v}) + \nabla \cdot (p\mathbf{v}) - \nabla \cdot (\lambda\nabla T)$$

$$= \underbrace{\frac{\partial(u\varrho)}{\partial t}}_{I} + \underbrace{\nabla \cdot (\varrho h\mathbf{v})}_{II} - \underbrace{\nabla \cdot (\lambda\nabla T)}_{III} = 0. \tag{4.20}$$

58

The energy balance equation 4.20 for any control volume neglects sources and sinks within the system. Term I describes the energy storage in the control volume. Convection (heat transport into the volume under consideration together with mass) is taken into account in term II. Finally, heat conduction is included in term III.

Detailed derivations of the energy balance equation can also be found in BEAR & STEPHAN (1998) [12] or SHAUGHNESSY ET AL. (2005) [90].

4.1.2 Mass balance equations

To formulate the mass balance equations for the multi-phase system, equation (4.8) is considered and phase saturations S_α, phase velocity $\mathbf{v}_\alpha$, and phase density ϱ_α are introduced. Furthermore, to take the porous medium into account, the storage term is extended by porosity ϕ. This yields a mass balance equation for each phase α:

$$\frac{\partial \left(\phi \, S_\alpha \varrho_\alpha \right)}{\partial t} + \nabla \cdot \left(\varrho_\alpha \mathbf{v}_\alpha \right) = 0. \tag{4.21}$$

As explained above, Darcy's Law is taken into account to compute the phase velocity instead of using the full balance equation of momentum. With the extended version of Darcy's Law (equation (2.29)) equation (4.21) yields the multi-phase differential equation for flow of several phases α without sinks or sources:

$$\frac{\partial \left(\phi \, S_\alpha \varrho_\alpha \right)}{\partial t} - \nabla \cdot \left(\varrho_\alpha \frac{k_{\mathrm{r}\alpha}}{\mu_\alpha} \mathbf{K} \left(\nabla p_\alpha - \varrho_\alpha \mathbf{g} \right) \right) = 0. \tag{4.22}$$

Balance over components

To describe the two-phase two-component system CO_2-water (or brine), it is useful to formulate balance equations of the components within the different phases. In this way, the mass transfer of the components between the phases is included in the balance equations and does not have to be described by extra terms. The concentration of the components within the phases is expressed with mass fractions (X_α^{C}) and the amount of a component in the system is calculated by adding the content in the phases. Two components in the system

yield two partial differential equations for the components C in the phases α:

$$\underbrace{\phi\frac{\partial(\sum_\alpha \varrho_\alpha X_\alpha^{\mathrm{C}} S_\alpha)}{\partial t}}_{\text{storage}}$$

$$-\underbrace{\sum_\alpha \nabla \cdot \left\{\frac{k_{\mathrm{r}\alpha}}{\mu_\alpha}\varrho_\alpha X_\alpha^{\mathrm{C}}\mathbf{K}(\nabla p_\alpha - \varrho_\alpha\mathbf{g})\right\}}_{\text{advective transport}}$$

$$-\underbrace{\nabla \cdot \left\{D_{\mathrm{pm}}^{\mathrm{C}}\varrho_{\mathrm{b}}\nabla X_{\mathrm{b}}^{\mathrm{C}}\right\}}_{\text{diffusive transport}}$$

$$-\underbrace{q^{\mathrm{C}}}_{\text{source/sink}} = 0 \qquad \mathrm{C} \in \{\mathrm{w},\mathrm{CO2}\},\ \alpha \in \{\mathrm{b},\mathrm{CO2}\}. \tag{4.23}$$

Note that α refers to the water-rich phase (brine, b) and to the carbon dioxide-rich phase (CO2) while the components (C) are water (w) and CO_2. As explained above, the salt is not considered as a separate component, but is taken into account with respect to fluid properties and dissolution (cf. Section 3.1.1). Beside the storage and the advective transport term considered in equation (4.22), equation (4.23) takes into account diffusive transport in the water phase (cf. Section 2.5.3) and a term for sources and sinks. Note that the storage term in equation (4.22) should yield

$$\frac{\partial\left(\phi\, S_\alpha \varrho_\alpha\right)}{\partial t} = \phi\frac{\partial(S_\alpha\varrho_\alpha)}{\partial t} + S_\alpha\varrho_\alpha\underbrace{\frac{\partial\phi}{\partial t}}_{=0} \tag{4.24}$$

but porosity ϕ is considered a constant and, as $\partial\phi/\partial t = 0$, this term can be disregarded. This means that no mass storage due to a change of the matrix is taken into account, i.e. the porous medium is rigid.

4.1.3   Energy balance equation

For the formulation of the energy balance equations for a multi-phase system local thermal equilibrium is assumed, i.e. all fluid phases and the porous medium have the same temperature at one point of the system (cf. Section 2.6.2). On this assumption, it is possible to set up one energy equation for the whole system instead of considering all phases separately.

The storage term in equation (4.20) splits up into energy storage within the fluids and within the porous medium. As for the mass balance equations, phase saturations, phase densities, porosity as well as specific internal energies for the phases are introduced. The sum over

the phases α yields the internal energy stored within the fluids. Note that the internal energy of the phases u_α depends on composition, i.e. the concentrations of the different components in the phases. The specific heat capacity of the porous medium c_s multiplied by the temperature corresponds to the internal energy of the matrix.

Heat conduction is taken into account by using the local heat conductivity for the porous medium and fluids λ_{pm} at the considered domain location under consideration. It depends on the heat conductivities of the matrix and the fluids as well as on porosity and saturations (cf. Sections 2.5.5, 3.4).

Furthermore, convective energy transport (thermal convection) is taken into account considering advective and diffusive movement of the fluids. Finally, after the addition of a term for sources and sinks, the multi-phase multi-component energy balance equation results in

$$\underbrace{\phi \frac{\partial \left(\sum_\alpha \varrho_\alpha u_\alpha S_\alpha\right)}{\partial t} + (1 - \phi)\frac{\partial(\varrho_{\mathrm{s}} c_{\mathrm{s}} T)}{\partial t}}_{\text{storage}}$$

$$-\underbrace{\nabla \cdot (\lambda_{\mathrm{pm}} \nabla T)}_{\text{heat conduction}}$$

$$-\underbrace{\sum_\alpha \nabla \cdot \left\{ \frac{k_{\mathrm{r}\alpha}}{\mu_\alpha} \varrho_\alpha h_\alpha \mathbf{K} \left(\nabla p_\alpha - \varrho_\alpha \mathbf{g}\right) \right\}}_{\text{heat transport due to advection}}$$

$$-\underbrace{\sum_{\mathrm{C}} \nabla \cdot \left\{ D_{\mathrm{pm}}^{\mathrm{C}} \varrho_{\mathrm{b}} h_{\mathrm{b}}^{\mathrm{C}} \nabla X_{\mathrm{b}}^{\mathrm{C}} \right\}}_{\text{heat transport due to diffusion}} - \underbrace{q^h}_{\text{source/sink}} = 0. \tag{4.25}$$

4.1.4 Complementary conditions for the balance equations

To solve the three balance equations with three primary unknowns, the following closure relationships are necessary:

- The sum of the saturations adds up to one:

$$\sum_\alpha S_\alpha = 1. \tag{4.26}$$

- The sum of the pressure of the wetting phase and the capillary pressure yields the pressure of the non-wetting phase:

$$p_{\mathrm{w}} + p_{\mathrm{c}} = p_{\mathrm{CO2}}. \tag{4.27}$$

61

- The sum of the mass fractions in one phase adds up to one:

$$\sum_{\mathrm{C}} X_{\alpha}^{\mathrm{C}} = 1. \tag{4.28}$$

4.1.5 Adaptive choice of primary variables

Applying Gibbs' phase rule (cf. Section 2.6.3) shows that the non-isothermal two-phase two-component system needs three independent state variables to be solved. This corresponds to the system of three partial differential equations (4.23) and (4.25) which can be solved using three unknowns called *primary variables*. With these it must be possible to determine all secondary variables that are sought in the equations.

One set of primary variables does not permit us to describe every possible state of the physical system. As an illustration, consider a system where both phases, water and CO_2, are present. The primary variables water saturation (S_{w}), CO_2 pressure (p_{CO2}) and temperature (T) allow the equations to be solved yielding results for all quantities needed. One of the secondary variables is the amount of dissolved CO_2 in the water-rich phase. If the conditions in the system change and leave a state without a free CO_2 phase, the amount of dissolved CO_2 mass in the water cannot be determined with the set of primary variables mentioned above. The primary variable S_{w} (which is 1.0 in this case) is changed to the amount of dissolved CO_2 ($X_{\mathrm{w}}^{\mathrm{CO2}}$) to fix this problem.

The different phase states with the corresponding primary variables and substitution criteria are listed in Table 4.1. The substitutions from "both phases" to "water phase" and "CO_2 phase" are conducted when $S_{\mathrm{w}} \geq 1.0$ and $S_{\mathrm{w}} \leq 0.0$, respectively. Here, the phase state "water phase" refers to the presence of only a single water-rich phase. Analogously, the term "CO_2 phase" means the presence of only a CO_2-rich phase.

Table 4.1: Primary variables and substitution criteria

phase state	present ph.	primary variables	water phase appears	gas phase appears
Both phases	w, CO_2	S_{w}, p_{CO2}, T	–	–
Brine phase	w	$X_{\mathrm{w}}^{\mathrm{CO2}}$, p_{CO2}, T	–	$X_{\mathrm{w}}^{\mathrm{CO2}} \geq (X_{\mathrm{w}}^{\mathrm{CO2}})_{\mathrm{max}}$
CO_2-rich ph.	CO_2	$X_{\mathrm{CO2}}^{\mathrm{w}}$, p_{CO2}, T	$X_{\mathrm{CO2}}^{\mathrm{w}} \geq (X_{\mathrm{CO2}}^{\mathrm{w}})_{\mathrm{max}}$	–

4.1.6 Initial and boundary conditions

Equations (4.23) and (4.25) describe a transient flow problem and therefore need initial and boundary conditions for the solution procedure. The *initial conditions* set values for the primary variables for every location of the model domain at the beginning of the simulation t_0.

Boundary conditions give values or fluxes for the boundaries of the system for the whole time under consideration. Two kinds of boundary conditions are available in the numerical simulator MUFTE-UG (cf. 1.3):

- The *Dirichlet boundary condition* sets a value for the considered primary variable at the boundary, e.g. a constant pressure or temperature.

- The *Neumann boundary condition* gives a flux over a boundary of the system, e.g. a mass flux or an energy flux.

Both boundary conditions can vary over time, e.g. a mass flux over a boundary can increase and decrease with time or a hydraulic head can change.

4.2 Numerical model

In this section, the numerical solution methods for the non-linear system of partial differential equations are explained. A fully implicit Euler scheme is used for the time discretization (Section 4.2.1). For the space discretization, the BOX method is utilized (Section 4.2.2). The linearization and the solution of the resulting set of linear equations using the Newton-Raphson method is discussed in Section 4.2.3.

4.2.1 Time discretization

For the time discretization a *fully implicit Euler scheme* is applied to the storage terms of the equations. It is a finite difference method of first order and yields for the time derivative of an unknown u

$$\frac{\partial u}{\partial t} \approx \frac{u^{t+\Delta t} - u^t}{\Delta t} = f(u^{t+\Delta t}) \tag{4.29}$$

with time step Δt. This approach gives a right hand side $f(u^{t+\Delta t})$ that depends on the unknown at the new time level.

The implicit Euler scheme is unconditionally stable and can be applied to complex problems such as of multi-phase flow in porous media (HELMIG (1997) [52], BASTIAN & HELMIG (1999) [14]). However, numerical diffusion is introduced into the system by time discretization as the investigation of a Taylor series expansion of HELMIG (1993) [49] has shown. This problem is reduced by an adaptive time-stepping scheme, which is explained further in Section 4.2.3.

4.2.2   Space discretization

For the space discretization of equations (4.23) and (4.25), the BOX method is used (e.g. BASTIAN (1999) [13], HELMIG (1997) [52]). It belongs to the subdomain collocation methods and can also be classified as a node-centered finite volume method based on the Galerkin finite element method. The advantages of the BOX method are that it can be used for unstructured grids and that it is locally (and therefore globally) mass conservative. In the following, the BOX method is derived for the mass balance equations applying the *method of weighted residuals* (e.g. CELIA & GRAY (1992) [23]). The energy balance equation is discretized analogously.

First, a finite element mesh is constructed that splits the model domain into a number of elements. These elements can be, for example, triangles and rectangles in two dimensions or tetrahedra and hexahedra in three dimensions. The points at which the element edges are intersect are called the nodes of the grid. Now, a secondary finite volume mesh is constructed by connecting the midpoints of the element edges with the barycenters of the elements. Figure 4.1 shows an example of a finite element and a secondary mesh. An element of the finite volume mesh is called *box*, *patch*, or *control volume* and always belongs to one node of the primary grid. One finite element contains parts of several boxes called *sub control volumes*. At the *integration points*, the fluxes are approximated; they lie on the edges (faces) of the sub control volumes, half way between midpoint of the element side and barycenter of the element.

The spatial distribution of an unknown u in the model domain Ω is required for the solution of the equations. To achieve this, discrete values of the unknown $\hat{u}$ are assigned to the nodes of the finite element mesh and interpolated between the nodes. The interpolation is carried out using a *basis function* N_j for every node j (also known as ansatz function, interpolation function, or shape function). The approximated values of the unknown $\tilde{u}$ are then found by

$$\tilde{u} = \sum_{j=1}^{n} \hat{u}_j \cdot N_j \tag{4.30}$$

64
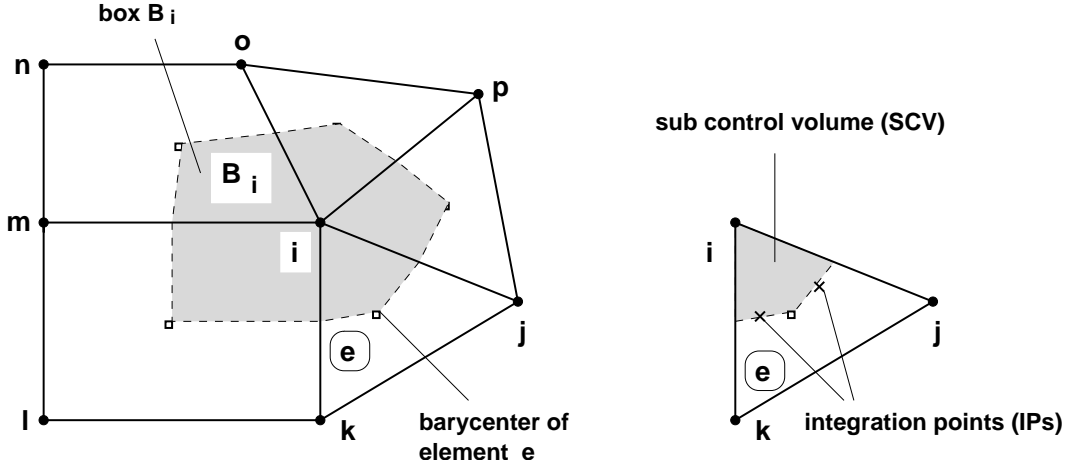
Figure 4.1: Finite element and finite volume mesh.

where n is the number of nodes in the model domain. For the basis functions, C^0-Lagrange polynomials are used. C^0 means that a function is continuous but not necessarily continuously differentiable. As shown in Figure 4.2 for the one-dimensional case, the values of N_j are always 1 for node j and 0 for every other node.
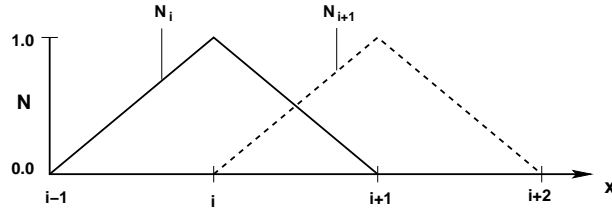
Figure 4.2: Basis function.

Applying this approximation procedure to the unknowns of equations (4.23) and (4.25) yields

$$\tilde{S}_{\mathrm{w}} = \sum_{j=1}^{n} \hat{S}_{\mathrm{w}j} \cdot N_j, \quad \tilde{p}_{\mathrm{CO2}} = \sum_{j=1}^{n} \hat{p}_{\mathrm{CO2},j} \cdot N_j, \quad \tilde{X}_{\alpha}^{\mathrm{C}} = \sum_{j=1}^{n} \hat{X}_{\alpha,j}^{\mathrm{C}} \cdot N_j, \quad \tilde{T} = \sum_{j=1}^{n} \hat{T}_j \cdot N_j. \quad (4.31)$$

The approximation of a gradient is computed by

$$\nabla \tilde{u} = \sum_{j \in \eta_i} (\hat{u}_j - \hat{u}_i) \nabla N_j. \quad (4.32)$$

Any location that the gradient is to be calculated for is part of a sub control volume that belongs to a node i. η_i is the set of neighboring nodes of node i. In Figure 4.1 the neighboring

nodes are j, k, m, o and p. Nodes l and n do not contribute, because they are not connected with node i. Only the nodes whose basis functions are $\neq 0$ at this location contribute to the calculation of the gradient.

Inserting the approximations (4.30) - (4.32) into equation (4.23) yields a residuum ε, because the equations are no longer exact. When the principle of orthogonality is applied, the residuum is weighted using the weighting functions (test functions) W_i so that ε becomes 0 over the entire domain Ω (e.g. CHUNG (2002) [25]):

$$\int_\Omega W_i \cdot \varepsilon \, d\Omega \overset{!}{=} 0. \tag{4.33}$$

The choice of the weighting functions can be carried out in various ways and yields different numerical methods based on the method of weighted residuals (e.g. CELIA & GRAY (1992) [23]). For the BOX method, a weighting function is chosen that is piecewise constant:

$$W_i = \begin{cases} 1 & \text{if } x \in B_i \\ 0 & \text{if } x \notin B_i \end{cases}$$

where B_i is the control volume (box) at node i. Note that the gradient of the weighting function always becomes 0, $\nabla W_i = 0$ with this approach. Figure 4.3 illustrates the weighting function used for the BOX method.
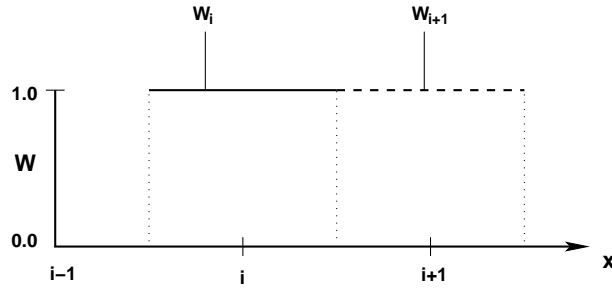

Figure 4.3: Weighting function.

Introducing the weighting function and integrating equation (4.23) over the entire model

domain Ω yields the weak form of the mass balance equation (e.g. CHUNG (2002) [25]):

$$
\underbrace{\int_\Omega W_i\, \phi \frac{\partial (\sum_\alpha \varrho_\alpha X_\alpha^C S_\alpha)}{\partial t} d\Omega}_{\text{I}}
$$

$$
\underbrace{-\int_\Omega W_i \sum_\alpha \nabla \cdot \left\{ \frac{k_{r\alpha}}{\mu_\alpha} \varrho_\alpha X_\alpha^C \mathbf{K}(\nabla p_\alpha - \varrho_\alpha \mathbf{g}) \right\} d\Omega}_{\text{II}}
$$

$$
\underbrace{-\int_\Omega W_i \nabla \cdot \left\{ D_{\text{pm}}^C \varrho_b \nabla X_b^C \right\} d\Omega}_{\text{III}}
$$

$$
\underbrace{-\int_\Omega W_i\, q^C d\Omega = 0}_{\text{IV}} \qquad C \in \{w, CO2\},\ \alpha \in \{b, CO2\}. \tag{4.34}
$$

For simplicity's sake, equation (4.34) is split up in terms I-IV, which are discussed separately.

Term I, storage: To find a numerical approximation of the storage term, first the time discretization described in Section 4.2.1 is introduced. Then equations (4.31) and (4.32) are inserted. Finally, the integral over the domain Ω is approximated by a sum over the neighboring nodes of the one considered. These derivations are carried out for one control volume, i.e. one node i.

$$
\int_\Omega W_i\, \phi \frac{\partial (\sum_\alpha \varrho_\alpha X_\alpha^C S_\alpha)}{\partial t} d\Omega
$$

$$
\approx \sum_{j \in \eta_i} W_i\, \phi \frac{1}{\Delta t} N_j \left\{ \left[\sum_\alpha \varrho_\alpha X_\alpha^C \hat{S}_\alpha \right]_j^{t+\Delta t} - \left[\sum_\alpha \varrho_\alpha X_\alpha^C \hat{S}_\alpha \right]_j^t \right\}
$$

$$
= \sum_{j \in \eta_i} M_{ij}\, \phi \frac{1}{\Delta t} \left\{ \left[\sum_\alpha \varrho_\alpha X_\alpha^C \hat{S}_\alpha \right]_j^{t+\Delta t} - \left[\sum_\alpha \varrho_\alpha X_\alpha^C \hat{S}_\alpha \right]_j^t \right\}. \tag{4.35}
$$

t is the current time level, Δt the time step that yields the new time, and η_i the set of neighboring nodes to i. The mass matrix is defined as

$$
M_{ij} = \int_\Omega W_i N_j\, d\Omega. \tag{4.36}
$$

It describes the influence of the neighboring nodes on node i in the region where the weighting function is greater than zero. In other words, M_{ij} specifies the intersection $N_j > 0 \cap W_i > 0$

for every node i. Introducing a *mass lumping technique* all entries of the mass matrix are assigned to its main diagonal (HUBER & HELMIG(1999) [55]). The use of the lumped mass matrix counteracts the appearance of non-physical oscillations of the solution (CELIA & BINNING (1992) [22]). Physically, mass lumping can be interpreted as concentrating the mass of a control volume at the node. The mass matrix then yields

$$
M_{ij} = \begin{cases} \int\limits_{\Omega} W_i \, d\Omega = \int\limits_{\Omega} N_i \, d\Omega = V_i & \text{for } i = j \\ 0 & \text{for } i \neq j \end{cases} .
$$

Term II, advective transport: For the discretized form of the advective term the product rule and the Green-Gaussian integral rule (equation (4.6)) are applied:

$$
\begin{aligned}
\int\limits_{\Omega} W_i \nabla \cdot \mathbf{F} \, d\Omega &= \int\limits_{\Omega} \nabla \cdot (W_i \cdot \mathbf{F}) \, d\Omega - \int\limits_{\Omega} (\nabla W_i) \cdot \mathbf{F} \, d\Omega \\
&= \oint\limits_{\Gamma} (W_i \cdot \mathbf{F}) \cdot \mathbf{n} \, d\Gamma - \int\limits_{\Omega} (\nabla W_i) \cdot \mathbf{F} \, d\Omega
\end{aligned} \tag{4.37}
$$

with $\oint\limits_{\Gamma}$ as the surface integral of domain Ω. As $\nabla W_i = \mathbf{0}$, the second term disappears and only the surface integral remains. The definitions of equations (4.31) and (4.32) and the total potential of phase α at node i is

$$
\hat{\Psi}_{\alpha i} := \hat{p}_{\alpha i} - \varrho_{\alpha i} \, g \, \hat{z}_i \tag{4.38}
$$

with $\hat{z}_i$ as the geodetic height of node i. Furthermore, the mobility of phase α, $\lambda_\alpha = k_{r\alpha}/\mu_\alpha$

and the time discretization are introduced. This yields the advection part of the equations:

$$\int_\Omega W_i \nabla \cdot \mathbf{F}\, d\Omega$$

$$= \int_\Omega W_i \sum_\alpha \nabla \cdot \left\{ \frac{k_{r\alpha}}{\mu_\alpha} \varrho_\alpha X_\alpha^{\mathrm{C}} \mathbf{K}(\nabla p_\alpha - \varrho_\alpha \mathbf{g}) \right\} d\Omega$$

$$\approx \int_\Omega W_i \sum_\alpha \nabla \cdot \left\{ \lambda_\alpha \varrho_\alpha X_\alpha^{\mathrm{C}} \mathbf{K} \left(\sum_{j \in \eta_i} (\hat{p}_{\alpha j} - \hat{p}_{\alpha i}) - \varrho_\alpha g \sum_{j \in \eta_i} (\hat{z}_{\alpha j} - \hat{z}_{\alpha i}) \right) \nabla N_j \right\} d\Omega$$

$$= \int_\Omega W_i \sum_\alpha \nabla \cdot \left\{ \lambda_\alpha \varrho_\alpha X_\alpha^{\mathrm{C}} \mathbf{K} \sum_{j \in \eta_i} (\hat{\Psi}_{\alpha j} - \hat{\Psi}_{\alpha i}) \nabla N_j \right\} d\Omega$$

$$= \oint_\Gamma W_i \sum_\alpha \left\{ \lambda_\alpha \varrho_\alpha X_\alpha^{\mathrm{C}} \mathbf{K} \sum_{j \in \eta_i} (\hat{\Psi}_{\alpha j} - \hat{\Psi}_{\alpha i}) \nabla N_j \right\} \cdot \mathbf{n}\, d\Gamma$$

$$= \sum_{l \in E_i} \sum_{j \in \eta_i} \sum_\alpha (\lambda_\alpha^l \varrho_\alpha X_\alpha^{\mathrm{C}})_{upw}^{t+\Delta t} \oint_{\Gamma_i} \mathbf{K}^l (\hat{\Psi}_{\alpha j} - \hat{\Psi}_{\alpha i})^{t+\Delta t} \nabla N_j \cdot \mathbf{n}\, d\Gamma$$

$$= \sum_{l \in E_i} \sum_{j \in \eta_i} \sum_\alpha (\lambda_\alpha^l \varrho_\alpha X_\alpha^{\mathrm{C}})_{upw}^{t+\Delta t} \left(\mathbf{K}^l (\hat{\Psi}_{\alpha j} - \hat{\Psi}_{\alpha i})^{t+\Delta t} \nabla N_{j,IP} \cdot \mathbf{n}_{IP} \right) \cdot A_{IP}. \qquad (4.39)$$

E_i is the set of elements connected to node i, l is the element considered. $\nabla N_{j,IP}$ denotes the gradient of the basis function at the integration point and $\mathbf{n}_{IP}$ the vector perpendicular to the sub control volume face of the integration point. The flux is approximated using the midpoint rule, i.e. flow velocity is computed at the integration point and considered constant for the cross-section of flow. Thus, flow velocity at the integration point multiplied by the cross-sectional area of the corresponding sub control volume face (A_{IP}) yields the flux. This procedure corresponds to the mass lumping technique using finite element methods (BASTIAN (1999) [13]).

To receive stable, non-oscillating solutions, a fully upwinding technique is applied (HELMIG (1997) [52]). This means the coefficients for the advective flux term are evaluated at the upstream node (subscript upw) which is found using the total potential:

$$upw(i,j) = \left\{ \begin{array}{l} i \text{ for } (\Psi_{\alpha j} - \Psi_{\alpha i}) \leq 0 \\ j \text{ for } (\Psi_{\alpha j} - \Psi_{\alpha i}) > 0 \end{array} \right. .$$

Term III, diffusive transport: For the diffusive transport term the same changes are

69

carried out as for the advective term. Thus, the discretized equation yields

$$\sum_{l \in E_i} \sum_{j \in \eta_i} (D_{\mathrm{pm}}^{\mathrm{C}} \varrho_{\mathrm{b}})_{ij}^{t+\Delta t} \oint_{\Gamma_i} (X_{\mathrm{b},j}^{\mathrm{C}} - X_{\mathrm{b},i}^{\mathrm{C}})^{t+\Delta t} \nabla N_j \cdot \mathbf{n} \, d\Gamma \tag{4.40}$$

$$= \sum_{l \in E_i} \sum_{j \in \eta_i} (D_{\mathrm{pm}}^{\mathrm{C}} \varrho_{\mathrm{b}})_{ij}^{t+\Delta t} \left((X_{\mathrm{b},j}^{\mathrm{C}} - X_{\mathrm{b},i}^{\mathrm{C}})^{t+\Delta t} \nabla N_{j,IP} \cdot \mathbf{n}_{IP} \right) \cdot A_{IP}. \tag{4.41}$$

Here, the coefficients are computed by arithmetic averaging of the values at nodes i and j.

Term IV, source/sink: The source/sink term yields

$$(V_i q_i^{\mathrm{C}})^{t+\Delta t}. \tag{4.42}$$

Summing up terms I-IV yields the mass balance equations of the two-phase two-component system discretized with the BOX method:

$$\sum_{j \in \eta_i} M_{ij} \phi \frac{1}{\Delta t} \left\{ \left[\sum_\alpha \varrho_\alpha X_\alpha^{\mathrm{C}} \hat{S}_\alpha \right]_j^{t+\Delta t} - \left[\sum_\alpha \varrho_\alpha X_\alpha^{\mathrm{C}} \hat{S}_\alpha \right]_j^{t} \right\}$$

$$- \sum_{l \in E_i} \sum_{j \in \eta_i} \sum_\alpha (\lambda_\alpha^l \varrho_\alpha X_\alpha^{\mathrm{C}})_{upw}^{t+\Delta t} \left(\mathbf{K}^l (\hat{\Psi}_{\alpha j} - \hat{\Psi}_{\alpha i})^{t+\Delta t} \nabla N_{j,IP} \cdot \mathbf{n}_{IP} \right) \cdot A_{IP}$$

$$- \sum_{l \in E_i} \sum_{j \in \eta_i} (D_{\mathrm{pm}}^{\mathrm{C}} \varrho_{\mathrm{b}})_{ij}^{t+\Delta t} \left((X_{\mathrm{b},j}^{\mathrm{C}} - X_{\mathrm{b},i}^{\mathrm{C}})^{t+\Delta t} \nabla N_{j,IP} \cdot \mathbf{n}_{IP} \right) \cdot A_{IP}$$

$$- (V_i q_i^{\mathrm{C}})^{t+\Delta t} = 0, \quad \forall i, \mathrm{C} \in \{\mathrm{w}, \mathrm{CO2}\}, \alpha \in \{\mathrm{b}, \mathrm{CO2}\}. \tag{4.43}$$

The numerical scheme is mass conservative as fluxes are locally balanced over a control volume, i.e. the mass flow over the control volume face of node i changes the mass stored in the volume that is assigned to node i.

4.2.3 Solution of the discretized equations

Equations (4.23) and (4.25) yield a non-linear system of three coupled partial differential equations. These are discretized as shown in Section 4.2 and result in a set of 3 non-linear algebraic equations per node. To solve this system it is necessary to linearize the equations before the resulting linear set of equations can be solved. This is done with the *Newton-Raphson method*, which is an iterative root-finding algorithm (e.g. FAIRES & BURDEN (1994) [36]). The set of equations can be written as

$$\mathbf{F}(\mathbf{x}) = \mathbf{0} \tag{4.44}$$

where $\mathbf{x}$ is the vector of primary variables. Note that the primary variables do not have to be the same but can change as described in Section 4.1.5. To solve equation (4.44) for the unknowns $\mathbf{x}$, a Taylor series expansion neglecting higher-order terms is used, resulting in:

$$\mathbf{F}(\mathbf{x}^{t+\Delta t,m+1}) \approx \mathbf{F}(\mathbf{x}^{t+\Delta t,m}) + \left(\frac{\partial \mathbf{F}}{\partial \mathbf{x}}\right)_{t+\Delta t,m} \cdot (\mathbf{x}^{t+\Delta t,m+1} - \mathbf{x}^{t+\Delta t,m}). \qquad (4.45)$$

Here, $t + \Delta t$ denotes the time level that the solution is computed for, m is the counter of non-linear iterations. Equation (4.45) has to yield $\mathbf{0}$ (a root has to be found); thus, it can be rewritten as

$$\mathbf{J}(\mathbf{x}^{t+\Delta t,m})\mathbf{u} = -\mathbf{F}(\mathbf{x}^{t+\Delta t,m+1}) \qquad (4.46)$$

with $\mathbf{J} = \partial \mathbf{F}/\partial \mathbf{x}$ being the Jacobian matrix and $\mathbf{u} = \mathbf{x}^{t+\Delta t,m+1} - \mathbf{x}^{t+\Delta t,m}$ the correction of the solution vector. $\mathbf{F}(\mathbf{x}^{t+\Delta t,m+1})$ denotes the defect term at time level $t + \Delta t$ and iteration step $m + 1$.

The linearization is the part of the procedure in which the Jacobian matrix is set up. The Jacobian matrix describes the change of each function of $\mathbf{F}(\mathbf{x}) = (f_1, f_2, ..., f_n)$ due to changes in the different unknowns $\mathbf{x} = (x_1, x_2, ..., x_n)$ and therefore yields a $(n \times n)$-matrix. It is evaluated using numerical differentiation. The coefficients J_{ij} are computed as follows:

$$\begin{aligned} J_{ij} &= \frac{\partial f_i^{k+1,m}}{\partial x_j} \\ &\approx \frac{f_i(..., x_{j-1}, x_j + \Delta x_j, x_{j+1}, ...) - f_i(..., x_{j-1}, x_j - \Delta x_j, x_{j+1}, ...)}{2\Delta x_j} \end{aligned} \qquad (4.47)$$

where x_j is a component of the solution vector and $\Delta x_j = \delta \cdot x_j$ a small increment, for example, $\delta = 10^{-8}$. The resulting set of linear equations can be solved with common linear solvers.

The iterative procedure of the Newton-Raphson method is made clear in the following pseudo-code:

Choose $\mathbf{x}^{t+\Delta t,0}$; set $m = 0$;

while $((||\mathbf{F}(\mathbf{x}^{t+\Delta t,m})||_2 \,/\, ||\mathbf{F}(\mathbf{x}^{t+\Delta t,0})||_2 > \varepsilon_{nl}) \wedge (||\mathbf{F}(\mathbf{x}^{t+\Delta t,m})||_2 > abs_{nl}))$

{

   Solve $\mathbf{J}(\mathbf{x}^{t+\Delta t,m})\mathbf{u} = -\mathbf{F}(\mathbf{x}^{t+\Delta t,m})$

     with accuracy ε_{lin} resp. abs_{lin};

   $\mathbf{x}^{t+\Delta t,m+1} = \mathbf{x}^{t+\Delta t,m} + \eta\mathbf{u}$;

   Compute new defect: $\mathbf{F}(\mathbf{x}^{t+\Delta t,m+1})$

   $m = m + 1$;

}.

Here, $||\cdot||_2$ is the Euclidean vector norm and $||\mathbf{F}(\mathbf{x}^{t+\Delta t,m})||_2$ / $||\mathbf{F}(\mathbf{x}^{t+\Delta t,0})||_2$ the convergence rate. ε_{nl} and ε_{lin} give the accuracy criteria of the non-linear and the linear convergence rate, respectively. abs_{nl} and abs_{lin} are the non-linear and the linear stopping criteria for the respective solver if the defect falls below these values.

The damping factor $\eta = (1/2)^q$ scales the correction of the solution vector and is chosen such that the defect is improved from one iteration step to the following:

$$||\mathbf{F}(\mathbf{x}^{k+1,m+1})||_2 \leq \left[1 - \frac{1}{4}\left(\frac{1}{2}\right)^q\right] ||\mathbf{F}(\mathbf{x}^{k+1,m})||_2. \tag{4.48}$$

This method is called *line search*, $q \in \{0, 1, ..., n_{ls}\}$ is the line search step that runs up to its maximum number n_{ls} which is chosen between 4 and 6. If a defect reduction can be achieved within the line search, the next iteration step can start. If this is not the case, a time step reduction is applied (cf. BASTIAN (1999) [13]).

For the solution of the Jacobian system, sophisticated linear solving methods are applied, e.g. the bi-conjugated gradient method (Bi-CGSTAB) (e.g. MEISTER (1999) [71]) or the multi-grid method (e.g. HACKBUSCH (1985) [46]). For the detailed implementation into MUFTE-UG, the reader is referred to BASTIAN (1999) [13]. The use of the adaptive choice of primary variables (cf. Section 4.1.5) together with the multi-grid method is explained by CLASS ET AL. (2002) [29, 28].

Chapter 5

Principle studies, simulations

In this chapter, various simulations are carried out, demonstrating the model capabilities. The examples do not refer to real geological formations, but are set up to illustrate the occurring processes. In this way, a basic understanding of the behavior of CO_2 in the subsurface can be gained. However, the chosen parameters are assumed to be realistic.

The first example (Section 5.2) considers the propagation of a CO_2 plume in the subsurface on a short time scale. The advection and buoyancy away from the injection point and the migration behavior of the carbon dioxide encountering layers of low permeability are investigated. The long-term behavior of CO_2 in the storage formation on a time scale of 100 years is addressed by the second example (Section 5.3). Formation of fingers occurs, caused by density differences in the formation brine due to dissolved CO_2. This causes density driven convection and downward movement of the brine phase. As this phenomenon depends on the discretization of the numerical model, a further example is set up to study this effect (Section 5.3.4). The last example investigates the non-isothermal effects of the migrating CO_2 caused by evaporation and Joule-Thomson cooling.

5.1 Model preparation

Initial and boundary conditions

The mathematical problem described in Section 4.1 has to be fed with initial and boundary conditions in order to be solved (cf. 4.1.6). The following conditions are assumed when modeling CO_2 sequestration in deep saline aquifers:

- **Increasing salinity with depth:** The salinity can reach high values of up to $350\,\text{kg/m}^3$ (X_b^S=0.27, ADAMS & BACHU (2002) [7]) and affects the properties of the

pore fluid significantly (cf. Section 3.3). To take the changing salinity into account, a linear salinity profile with no salt content at the top and high salinity at the bottom is usually assumed. If the relevant processes occur at great depths, it is often sufficient to assume a constant salinity.

- **Geothermal gradient:** The average temperature rise with increasing depth is expressed by the geothermal gradient. In many cases, a geothermal gradient of $30\,°C/km$ can be assumed. However, it can reach values of up to $60\,°C/km$ and more (e.g. FYFE ET AL. (1978) [40]).

- **Hydrostatic pressure distribution:** In an undisturbed system, fully saturated conditions are assumed everywhere below the water table which typically lies only a few meters below the surface. This leads to hydrostatic pressure at any depth of the formation, depending on the height of the overlying water column and the water density. The water density itself depends on pressure, temperature (geothermal gradient), and salinity.

The boundary conditions have to represent the natural state of the system under consideration at all times of the simulation, i.e. they have to be far enough from the modeled processes not to have an influence on them.

5.2 CO$_2$ plume evolution in the subsurface

This first example investigates the carbon dioxide injection into the geological formation and its propagation in the subsurface. It is set up to study the main transport processes that drive the CO_2 migration on the short time scale, namely

- advection and

- buoyancy.

5.2.1 Model setup

Figure 5.1 shows the model domain of the example. Homogeneous properties of the formation in horizontal direction are assumed. Therefore, the CO_2 plume will develop radially symmetrically around the injection well and it is sufficient to model only a sector of a cylindrical domain. For this example, a domain is chosen with a length of $10000\,m$ and a height of $100\,m$. The top of the domain is $800\,m$ below the surface of the earth.
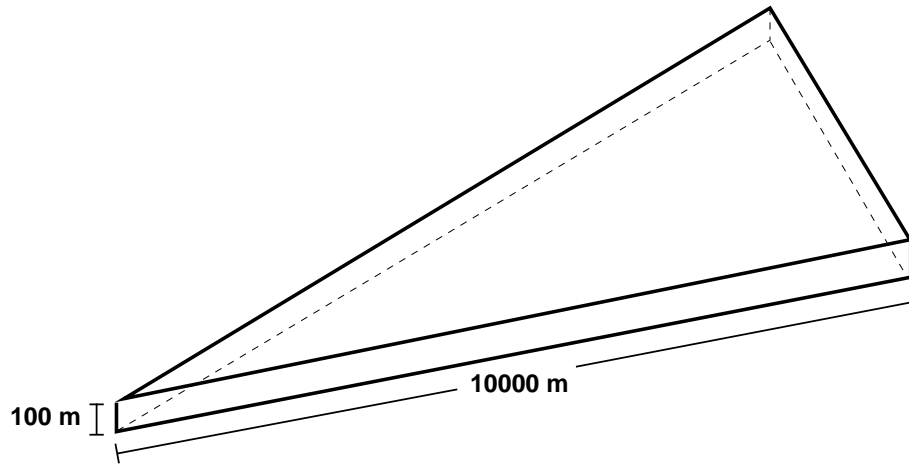
Figure 5.1: CO$_2$ plume evolution: model domain.

The permeability distribution throughout the model domain is shown in Figure 5.2. Two layers of low permeability separate the different sections of the storage reservoir. There is a difference of two orders of magnitude between the layers of high and low permeability. For more details on the model setup, the reader is referred to Appendix D.
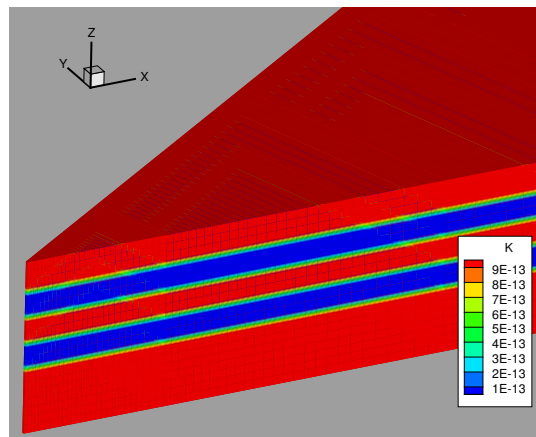
Figure 5.2: CO$_2$ plume evolution: permeability distribution.

The CO$_2$ is injected from the left side of the domain, where the injection well is given with a diameter of 2 m. A CO$_2$ mass flux of 0.02 kg/s is injected over the lower 20 m of the injection well for a period of 1 year. Top, bottom, and sides of the model domain do not allow flow across (no-flow boundaries). Hydrostatic pressure conditions are applied to the far end of the domain.

75

5.2.2 Simulation results

Figures 5.3 and 5.4 show the CO_2 saturations in the subsurface after 3 and 12 months, and after 2 and 10 years, respectively. The results after 3 months show horizontal and vertical CO_2 migration away from the injection well. Some carbon dioxide reaches the first layer of lower permeability and starts to pool up and to spread horizontally. The horizontal extension of the CO_2 plume after three months is 152 m.

After 12 months some CO_2 has already passed through the first layer of low permeability and has reached the second one. Here, the same effect of pooling up and lateral spreading can be observed. Underneath the first layer of low permeability, the lateral migration continues. A distance of 231 m lies between the injection well and the front of the plume after a simulation time of 12 months.

The CO_2 injection stops after one year, but the migration continues for some time. After 2 and 10 years the CO_2 plume has reached an extension of 245 m and 275 m, respectively (cf. Figure 5.4). It is still moving, though at decreasing velocity. Note that the CO_2 leaves a trace of residual saturation at every location it passes.
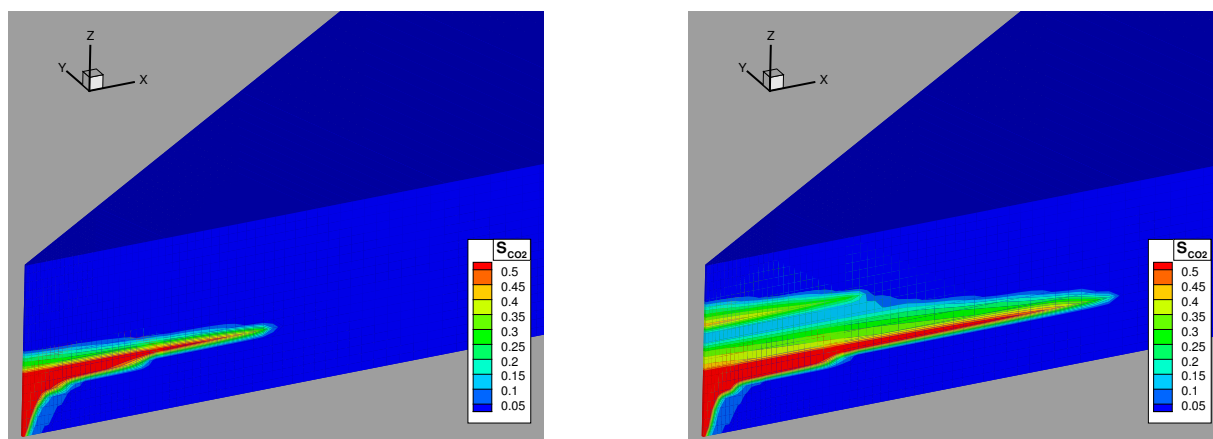
Figure 5.3: CO_2 plume evolution: CO_2 saturation after 3 and 12 months.

5.2.3 Discussion

The pressure gradients are the main driving force in the direct vicinity of the injection well. As the injection area extends over a depth of 20 m and a constant flux is assigned over this boundary, the pressure gradient mainly points in horizontal direction (except the top and bottom of the injection area). The further the CO_2 migrates away from the injection
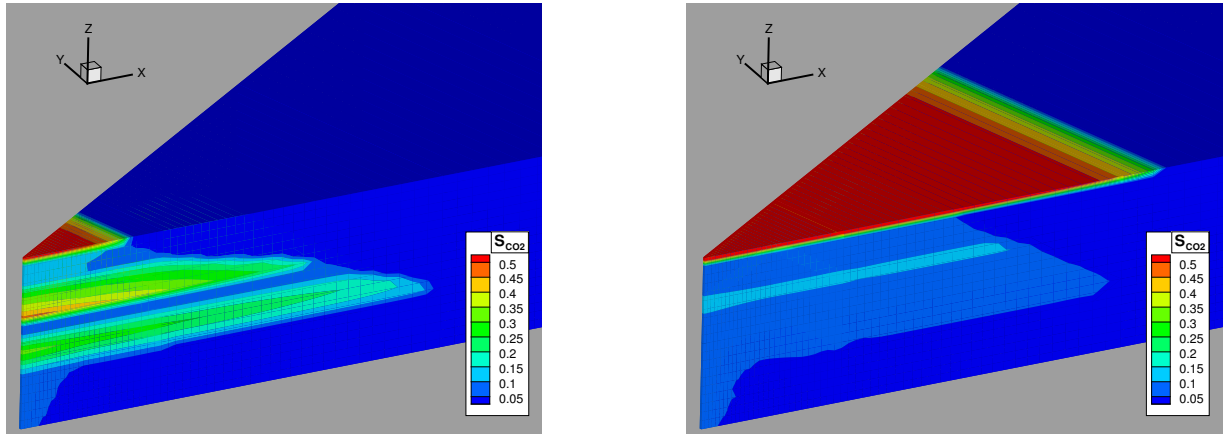
Figure 5.4: CO_2 plume evolution: CO_2 saturation after 2 and 10 years.

point the weaker become the advective driving forces and the greater gets the influence of buoyancy on the flow direction.

The layers of low permeability reduce the vertical CO_2 velocity significantly. Furthermore, the carbon dioxide has to overcome the entry pressure of the material of low permeability to enter this layer. Thus, more CO_2 reaches the layer from below than can be transported in the vertical direction. Pooling-up and horizontal migration occur. Note that the entry behavior of the CO_2 into the low-permeable layer depends strongly on the discretization. Detailed investigations of this topic have not been carried out in this work, but can be found, e.g., in JAKOBS [60].

The CO_2 movement in the subsurface continues for several years, because pressure and density gradients are still present. Once the carbon dioxide saturation drops to residual saturation, the CO_2 will not move due to advective and buoyancy forces. Then, it can only dissolve in the water and be transported diffusively.

5.3 Long-term effects

CO_2 is transported away from the injection well by advective processes and buoyancy (cf. Section 5.2). When reaching residual saturation the carbon dioxide is only transported by diffusion within the brine phase. Diffusive transport is very slow, thus, in this example a long time scale has to be taken into account. As CO_2 has to be stored safely in the subsurface for a long period of time, it is necessary to investigate this long-term behavior of the carbon dioxide in the geological formation.

The processes studied in these simulations are

- dissolution of CO_2 in the brine phase,

- diffusive transport of carbon dioxide in the brine phase,

- convective brine flow induced by density differences due to dissolved CO_2.

5.3.1 Model setup

Figure 5.5 shows the model setup of the simulation. A two-dimensional domain with a width of $3000\,m$ and a height of $1000\,m$ is chosen. The model domain contains two different geological formations $\Omega 1$ at the top and bottom and $\Omega 2$ in between. $\Omega 1$ can be considered the storage formations while $\Omega 2$ is a thick layer of low permeability that prevents the carbon dioxide from rising towards the surface (note that rock properties are not necessarily realistic, but the simulation is mainly set up to study the afore-mentioned processes). A limited amount of CO_2 mass is injected into the domain from the bottom boundary (Figure 5.5). Details of the model setup are given in Appendix D.
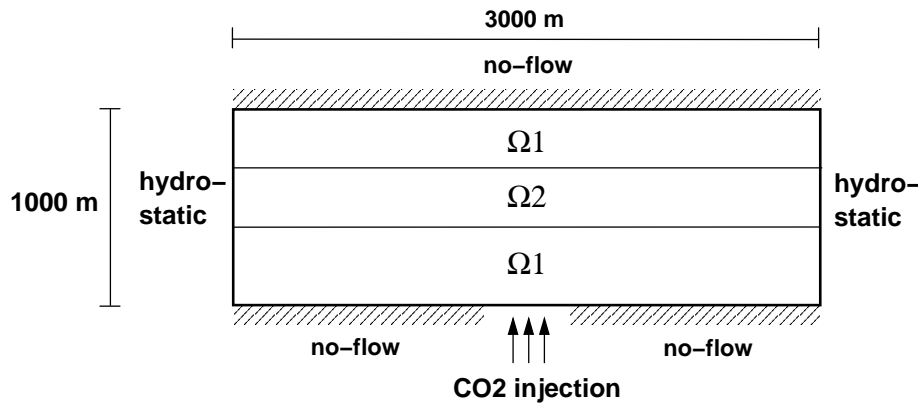
Figure 5.5: Long-term CO_2 storage: model setup.

5.3.2 Simulation results

The plume evolution after 1 year is illustrated in Figure 5.6, which shows carbon dioxide saturations. CO_2 enters the domain from below and migrates upwards until it hits the layer of low permeability. It penetrates the layer, but quickly stops moving, because residual saturation is reached and no more CO_2 flows into the domain.

When the CO_2 saturations after 1, 10, 50, and 100 years are compared (Figures 5.6, 5.7, 5.8, and 5.9), it becomes obvious that saturations decrease over time. As no flow of the CO_2

phase can occur, the change of saturation has to be caused by dissolution in the resident brine and diffusive transport.
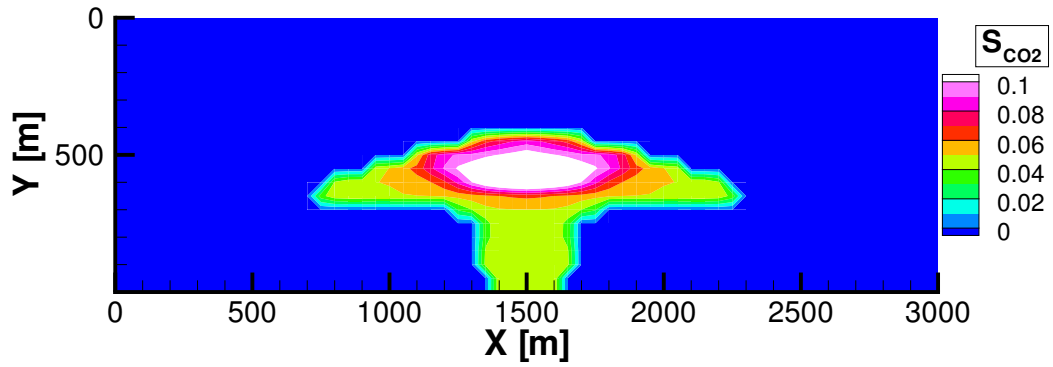
Figure 5.6: Long-term CO_2 storage: CO_2 saturation after 1 year.
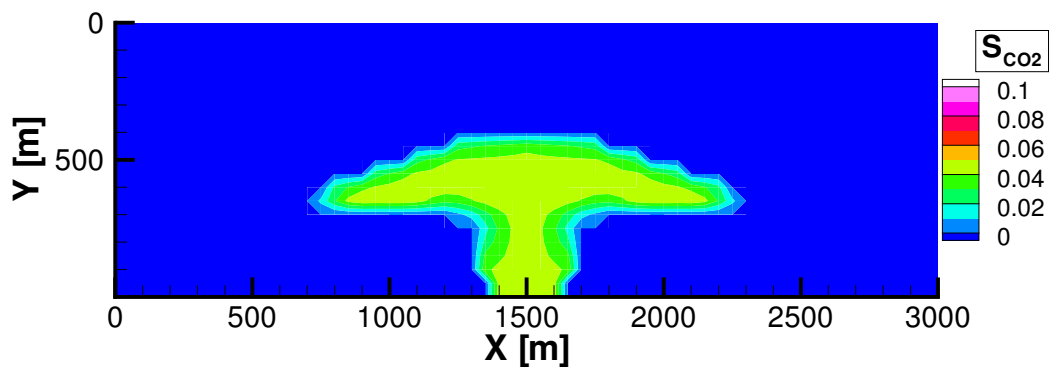
Figure 5.7: Long-term CO_2 storage: CO_2 saturation after 10 years.
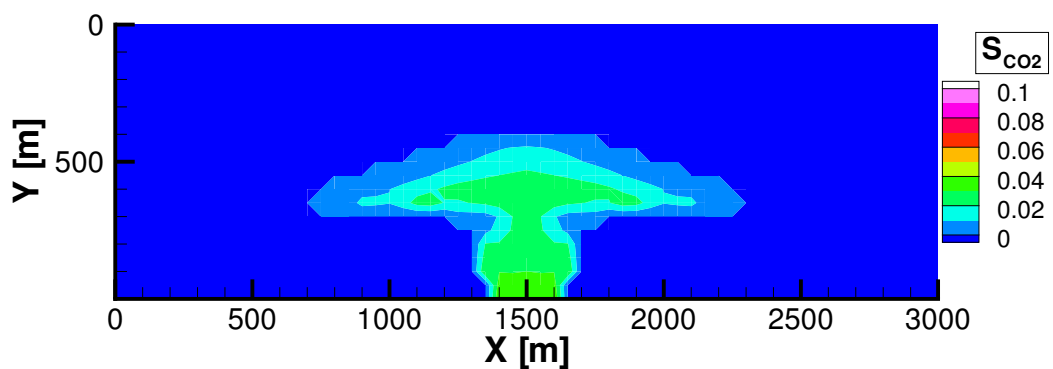
Figure 5.8: Long-term CO_2 storage: CO_2 saturation after 50 years.
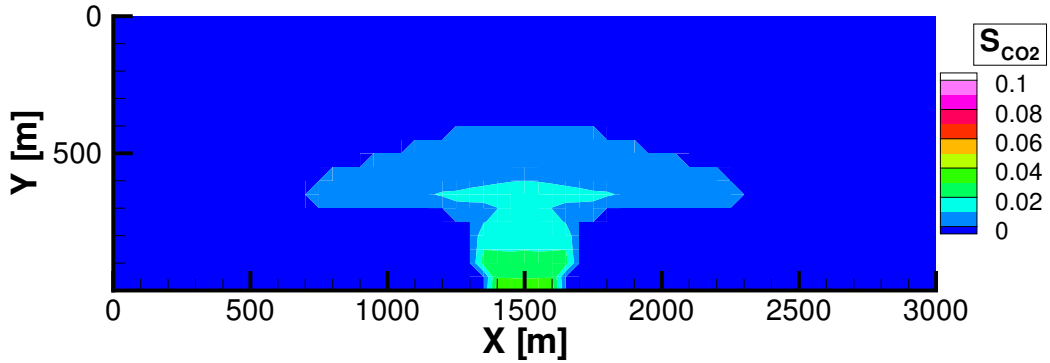
Figure 5.9: Long-term CO_2 storage: CO_2 saturation after 100 years.

Figures 5.10, 5.11, 5.12, and 5.13 show CO_2 dissolved in the brine phase after a simulation time of 1, 10, 50, and 100 years, respectively. After 1 year, the distribution of dissolved carbon dioxide looks very similar to the CO_2 saturation. At a simulated time of 10 years, the dissolved CO_2 plume has extended slightly and starts to form small fingers that point downwards at both ends of the symmetrically shaped plume. The results for the dissolved carbon dioxide after 50 and 100 years clearly show that it is sinking down and accumulating at the bottom of the model domain.
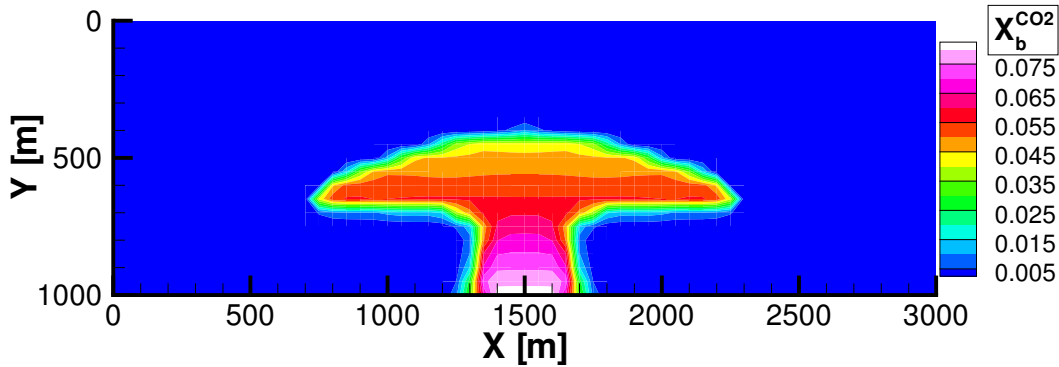
Figure 5.10: Long-term CO_2 storage: CO_2 mass fraction in brine after 1 year.

5.3.3   Discussion

Due to advection and buoyancy, the injected CO_2 rises towards the surface and then pools up at $\Omega 2$. Some CO_2 infiltrates the layer of low permeability, but residual saturation is reached quickly, because only a small amount of carbon dioxide enters the domain. As soon as residual saturation is reached, advective and buoyancy forces cannot cause CO_2 movement.
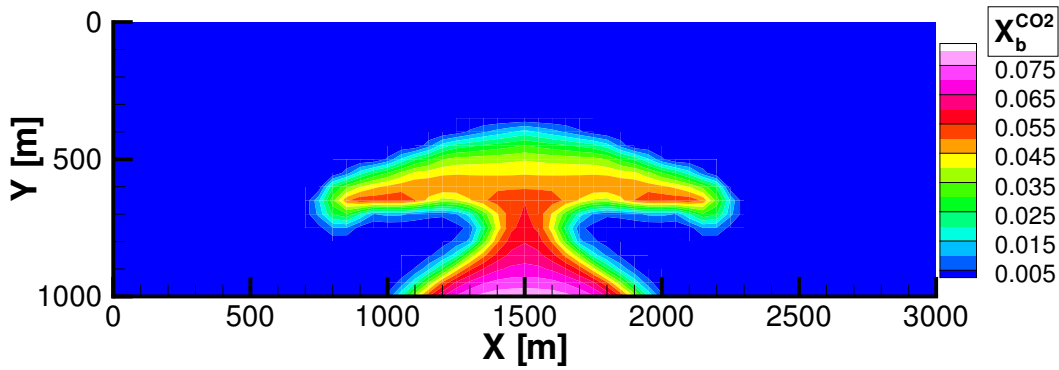
Figure 5.11: Long-term CO_2 storage: CO_2 mass fraction in brine after 10 years.
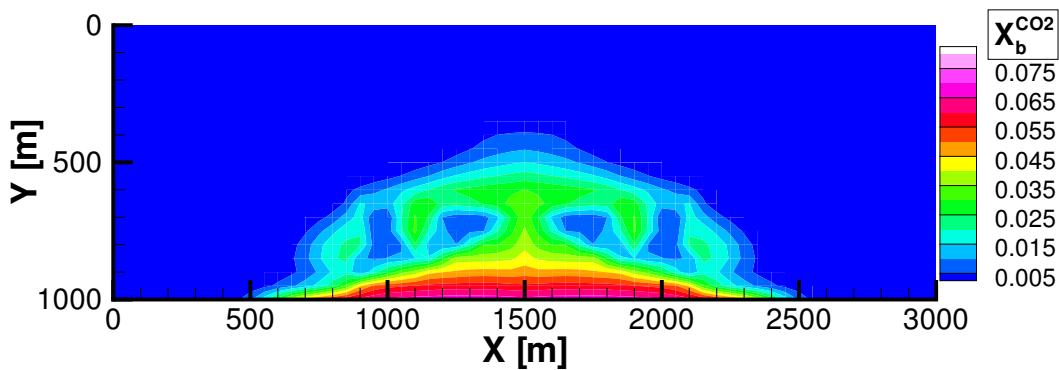
Figure 5.12: Long-term CO_2 storage: CO_2 mass fraction in brine after 50 years.

The CO_2 dissolves in the water and is transported away diffusively from its source, the CO_2 as a phase.

Another effect becomes obvious, namely the brine density change due to dissolved CO_2 (cf. Section 3.3.1). The higher the CO_2 content, the higher brine density; therefore, brine with dissolved carbon dioxide is heavier than the surrounding "fresh" brine. The instable layering (heavier brine over lighter brine) is maintained until a small perturbation disturbs the system and triggers downward fingering of the CO_2-saturated brine. This flow is caused by density differences and is thus considered density driven convection. It causes the dissolved carbon dioxide to sink downwards and to pool up at the bottom of the model domain (Figures 5.12 and 5.13). The number of fingers that form in the numerical model influences the amount of dissolved CO_2 in brine and depends on the discretization of the model domain. This phenomena is investigated more in detail in Section 5.3.4.

The effect of an increased brine density due to dissolved carbon dioxide is positive for the
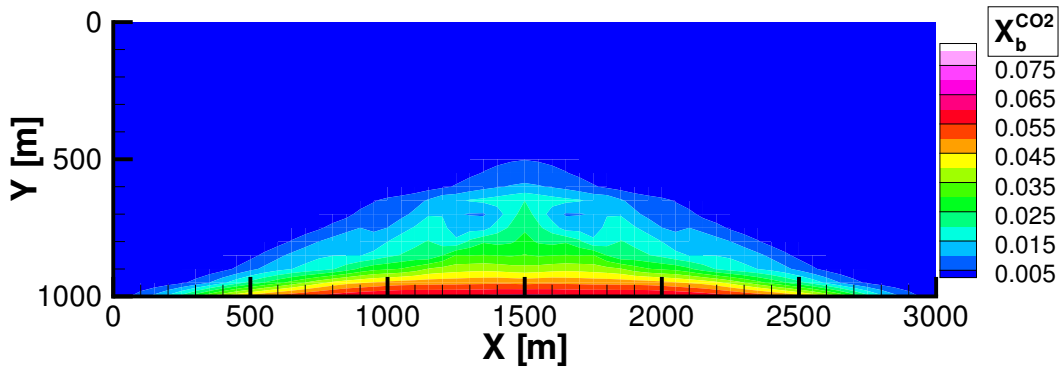
Figure 5.13: Long-term CO_2 storage: CO_2 mass fraction in brine after 100 years.

secure CO_2 storage in the subsurface. The density driven brine convection causes more carbon dioxide to dissolve and the CO_2 saturation decreases faster than it would without this effect. This becomes clear when comparing Figures 5.14 and 5.15: Figure 5.14 shows the CO_2 saturation after a simulation time of 100 years taking into account the increased brine density due to dissolved carbon dioxide. In Figure 5.15, the same result is shown, the only difference being that dissolved CO_2 does not influence brine density here. Thus, only diffusion in the brine phase can transport the CO_2 away from the plume and the carbon dioxide saturations are still higher after 100 years.

Another positive effect for the long-term CO_2 sequestration is that the dissolved CO_2 sinks downwards and therefore is not likely to migrate into regions of lower pressures where it might form its own phase. This improves the safety with respect to CO_2 rising towards the surface.

In this example, the CO_2 phase completely dissolves in the brine within a few hundred years. It will take a lot longer to dissolve the entire CO_2 plume when significant amounts of carbon dioxide are injected into an aquifer. However, the effects shown in this simulation are likely to occur and to enhance long-term CO_2 storage.

5.3.4 Influence of discretization on the simulation results

The long-term dissolution behavior of carbon dioxide in brine during CO_2 sequestration has been studied by LINDEBERG & WESSEL (1997) [67] and ENNIS-KING & PATERSON (2003) [35]. In Section 5.3, it is shown that the dissolution of CO_2 in the water-rich phase increases brine density. The instable layering of higher-density brine above lower-density brine is disturbed and a downward flow of higher-density brine with dissolved CO_2 occurs in fingers. The shape and number of the fingers that form in the simulations depend on the
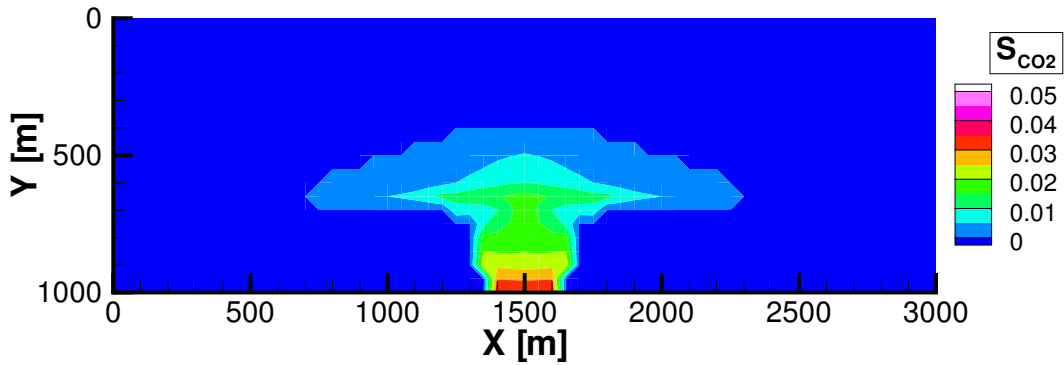
Figure 5.14: Long-term CO_2 storage: CO_2 saturation after 100 years with density effect due to dissolved CO_2.
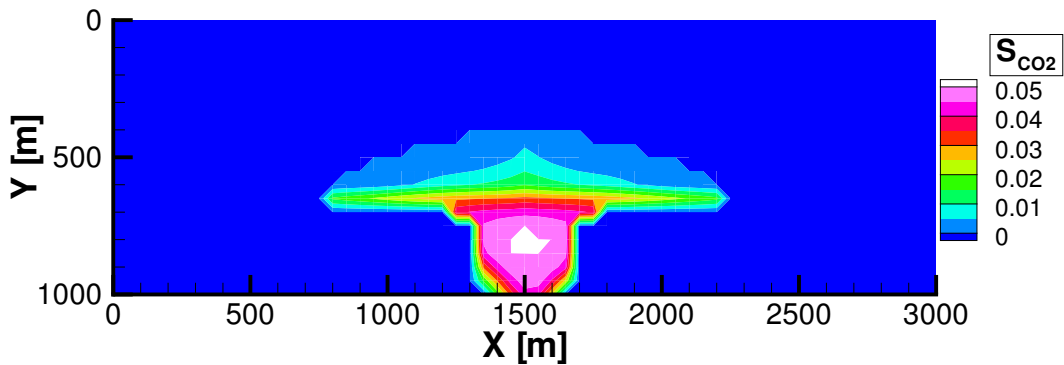
Figure 5.15: Long-term CO_2 storage: CO_2 saturation after 100 years without density effect due to dissolved CO_2.

discretization of the model domain. The present example therefore focuses on the following details:

- Effect of discretization on the formation of fingers of CO_2 saturated brine.

- Influence of different finger formations on the amount of dissolved CO_2 in the system.

Model setup: Figure 5.16 sketches the two-dimensional model domain which has an area of 50 m x 20 m. No flow is possible across the left, right, and bottom boundaries. A constant CO_2 saturation of 5 % and a pressure of 80 bar is given at the upper boundary. The initial conditions within the domain are 5 % CO_2 saturation in the upper 5 m and hydrostatic pressure distribution throughout the domain. Below a depth of 5 meters from the top boundary, no CO_2 is present.

This setup mimics a small part of a CO_2 plume which is trapped at residual saturation underneath a cap-rock. The investigated flow processes take place in vertical direction, so it is sufficient to model only a small horizontal section. On the other hand, the horizontal extension may not be too small, because the horizontal discretization influences the formation of fingers and thus the vertical migration.
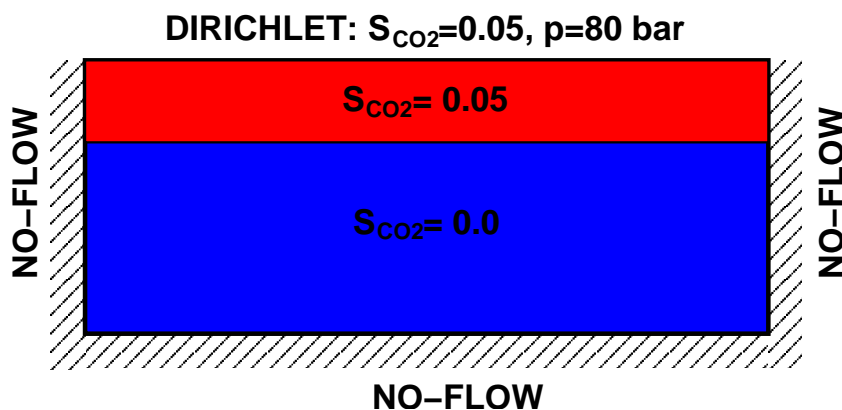
Figure 5.16: Fingering caused by density differences, influence of discretization: homogeneous model domain, initial and boundary conditions.

Simulation results and discussion: Figures 5.17, 5.18, and 5.19 show the results for the dissolved CO_2 concentration after a simulation time of 2 years for horizontal discretization lengths of 2.5 m, 1.25 m, and 0.3125 m, respectively. Every node of the mesh can produce a small perturbation that causes downward flow to start and fingers to form. This is due to numerical errors (round-off, solver accuracy etc.) occuring at the node, that cannot be dampened by counter-acting physical processes. The number of fingers increases with the number of nodes in a horizontal plane.

Figure 5.20 (page 87) depicts the CO_2 mass in the system and its distribution in the phases over time. While the mass in the CO_2 phase slowly decreases, the total mass as well as the CO_2 dissolved in brine increase over time. This is because a constant CO_2 saturation is given at the upper boundary. Therefore, more CO_2 mass flows into the system as the initial CO_2 in phase slowly dissolves and carbon dioxide saturation decreases.

The influence of discretization on the CO_2 mass dissolved in the brine phase is shown in Figure 5.21 (page 88). With the fine grid, it becomes clear that significantly more CO_2 is dissolved. The reason for this is the increasing number of fingers that cause enhanced convective downward flow. As more CO_2 is transported away from its source (the region of CO_2 in phase) more carbon dioxide can dissolve at the interface between the two-phase region (CO_2 and brine) and the one-phase zone (only brine). The length of the interface between
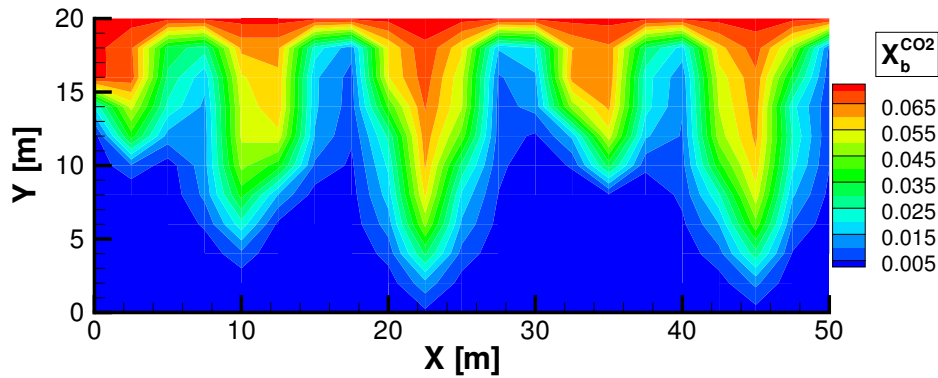
Figure 5.17: Fingering caused by density differences, influence of discretization: $\Delta h = 2.5\,\text{m}$.
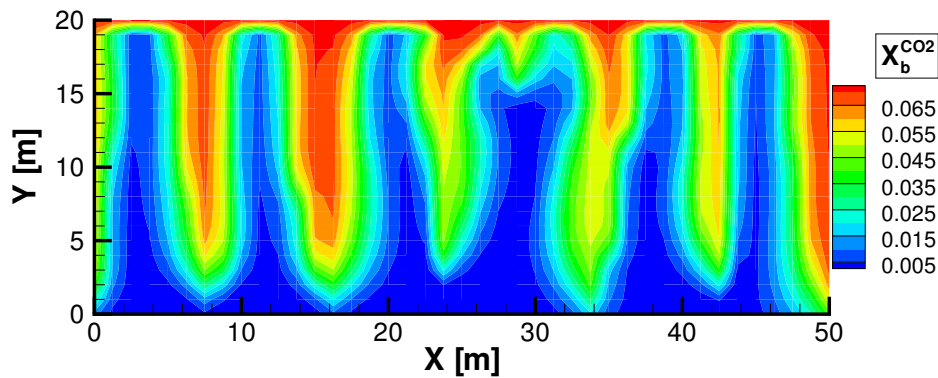
Figure 5.18: Fingering caused by density differences, influence of discretization: $\Delta h = 1.25\,\text{m}$.

brine with high CO_2 concentration and brine with low CO_2 concentration also increases with the number of fingers causing a slightly increasing influence on the diffusion process.

The simulations presented here can only be interpreted as a preliminary approach to the problem. Many more investigations have to be carried out to understand the role of enhanced CO_2 dissolution caused by convective mixing. Key issues that have to be addressed in this context are:

- What is the real number and size of the fingers that occur during convective mixing? Can they be represented by a numerical model?

- How does the dimensionality of the model used here influence the fingers? It is very likely that the formation of the fingers looks different in a three-dimensional model. This will also affect the dissolution rate of the CO_2.
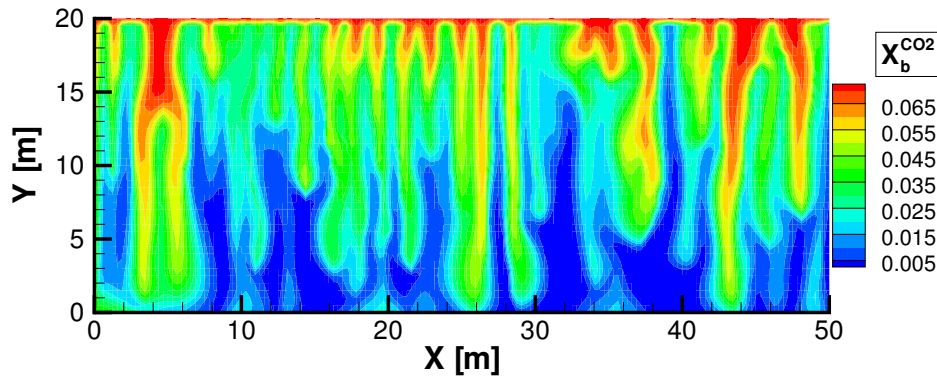
Figure 5.19: Fingering caused by density differences, influence of discretization: $\Delta h = 0.3125\,\text{m}$.

- What is the influence of heterogeneities on the formation of fingers?

- What is the long-term effect of the afore-mentioned aspects on the dissolution behavior of large amounts of carbon dioxide in the subsurface (time until total dissolution etc.)?

These questions go far beyond the scope of this work. However, the present studies have shown that the discretization influences the simulation results concerning the long-term dissolution of CO_2 in a brine aquifer. When grids that are too coarse are used, the amount of dissolved carbon dioxide is rather underestimated. This corresponds to a conservative approach with respect to the safe long-term storage of CO_2 sequestration.

5.4   Non-isothermal effects

This problem is set up to study the non-isothermal effects of the carbon dioxide close to the well and during its upward migration. A cooling of the CO_2 is expected caused by

- expansion (Joule-Thomson cooling) and

- evaporation.

Cooling due to expansion takes place for most real fluids when they expand adiabatically, i.e. the pressure is reduced and there is no heat transfer to the system. This effect is known as Joule-Thomson cooling.

When evaporating from the liquid to the gaseous state of aggregation, the carbon dioxide needs to take up a significant amount of energy. This is the latent heat of evaporation and it can be supplied by the surroundings so that a local temperature reduction takes place.
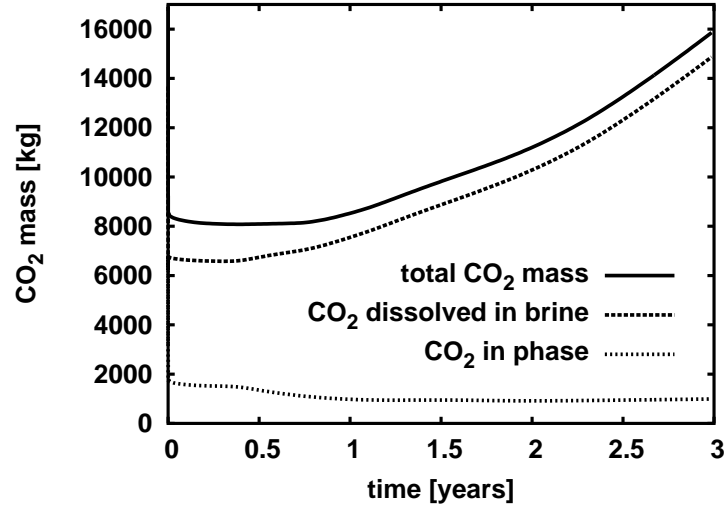
Figure 5.20: Fingering caused by density differences, CO_2 mass distribution: total CO_2 in the system, CO_2 in phase, and dissolved CO_2.

5.4.1 Model setup

The two-dimensional model domain with an area of $500\,\mathrm{m}$ x $500\,\mathrm{m}$ is shown in Figure 5.22. CO_2 is injected from the lower left side at a rate of $1.25\,\mathrm{kg/s}$ with a constant temperature of $37\,^\circ\mathrm{C}$. The injection point lies at a depth of approximately $900\,\mathrm{m}$ below the surface; therefore, the CO_2 enters the domain in supercritical state. No-flow boundary conditions are assigned to the left and the top of the model domain. Hydrostatic pressure and constant temperature is set at the right and the bottom boundary. The initial temperature is $37\,^\circ\mathrm{C}$. The properties of the porous medium are homogeneous and isotropic throughout the entire model domain.

5.4.2 Simulation results

The CO_2 is injected into the model domain and migrates upwards due to buoyancy forces. Figure 5.23 (left) shows the CO_2 saturation after a simulation time of one month. There are areas of increased CO_2 saturation around the injection point and below the top boundary where the carbon dioxide is pooling up. The temperature plot (Figure 5.23) shows a cooling in the regions where CO_2 is present and a slight warming at the injection point. A small area of stronger cooling effects can be observed at the left boundary between 310 and $330\,\mathrm{m}$ above the bottom of the domain (corresponding to 670 to $690\,\mathrm{m}$ below the surface). While the cooling causes temperature decreases of $\Delta T = 2\,^\circ\mathrm{C}$, the heating at the injection point is less than $\Delta T = 0.5\,^\circ\mathrm{C}$.
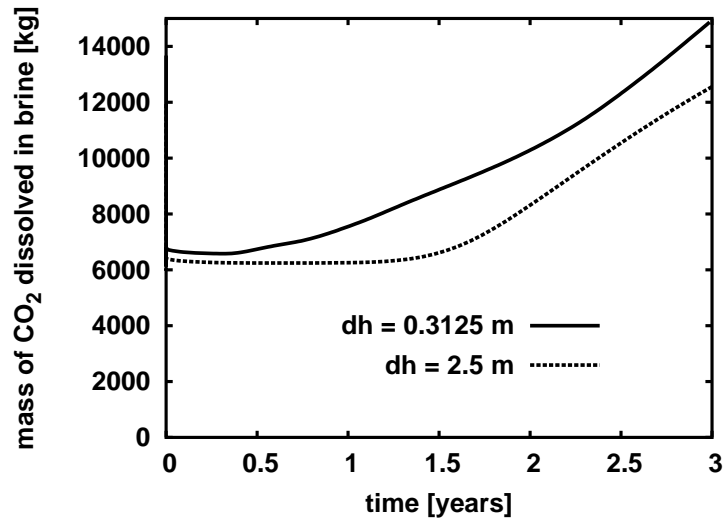
Figure 5.21: Fingering caused by density differences, CO_2 dissolved in water: comparison of simulation results between coarse and fine grid.

5.4.3 Discussion

The CO_2 expands as it enters the domain because it flows in the direction of lower pressures. As explained above, the expansion causes the Joule-Thomson effect, i.e. a cooling of the CO_2. Even though the process under consideration is not adiabatic (heat conduction also takes place), the cooling due to expansion is significant, because the Joule-Thomson effect takes place a lot faster than the heat conduction.

Further cooling occurs in the region where the CO_2 evaporates from the supercritical to the gaseous phase. Again, temperature reduction due to evaporation takes less time than heat conduction needs to equilibrate the cooling.

The small area close to the injection point which warms up can be explained as an artifact caused by the model. As a constant CO_2 flux is forced into the model domain, the pressure close to the injection point rises. The CO_2 is compressed after entering the domain and then heats up due to the volume decrease. As the CO_2 flux can only occur from higher to lower pressures, this heating is not realistic. Since this effect only happens close to the injection point and does not influence most of the model domain, no more thought was given to this problem.

The example discussed above shows that non-isothermal effects occur during CO_2 migration in the subsurface. The cooling effects observed in the simulation result in only relatively small temperature changes. This might make the non-isothermal effects seem negligible.
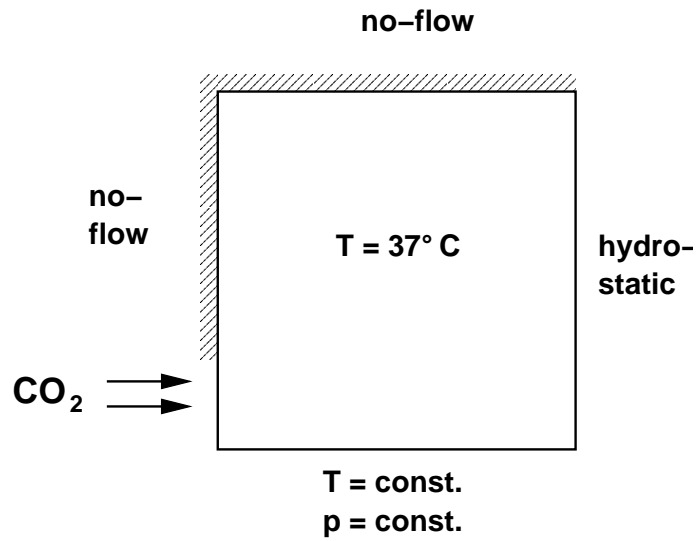
Figure 5.22: Non-isothermal effects: model domain, initial and boundary conditions.

However, further investigations have to be carried out in this context, especially with regard to CO_2 leakage in fractures or faults in areas close to the surface of the earth. In this case, cooling effects might play an important role and change the physics of the subsurface flow significantly.
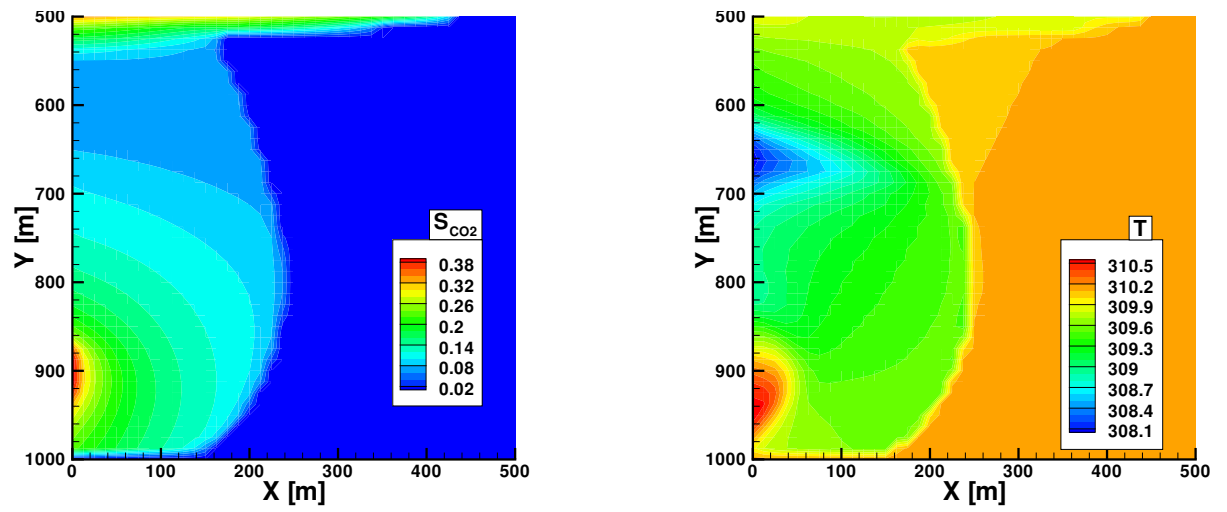
Figure 5.23: Non-isothermal effects: CO_2 saturation and temperature after 1 month.

Chapter 6

Summary and conclusions

The change in the global climate caused by the emission of greenhouse gases is discussed and becomes more and more acknowledged within the scientific community. The most important climate-effective gas is CO_2, because it is emitted into the atmosphere in very large quantities. Carbon dioxide sequestration in deep geological formations is considered as a technology for mitigating these emissions and thus the change in the global climate. The feasibility of applying this method to large quantities of CO_2 has to be investigated with all available scientific means.

One important aspect of CO_2 sequestration is the carbon dioxide flow and transport within the rock used as a storage formation. Questions regarding the evolution of the CO_2 plume in the subsurface, its long-term behavior, non-isothermal effects, geochemical reactions or geomechanical effects have to be answered. One way of addressing these issues is the mathematical description of the processes that occur in the subsurface and the numerical solution of the resulting complex equations.

In this study, a numerical model for the investigation of non-isothermal multi-phase flow and transport processes of CO_2 and brine in a porous medium is developed. The physical fundamentals used for the model are described in Chapter 2. Chapter 3 explains the application of the theory to the model and the approaches used for the description of the physical properties needed. The mathematical model and its numerical implementation are described in Chapter 4. Chapter 5 gives the description of the simulations carried out. These simulations give insight into the processes that occur when CO_2 is stored in geological formations.

Model characteristics: The main characteristics of the model developed in this study are the following:

- A two-phase two-component approach is applied considering a CO_2-rich and a water-rich phase. The latter is usually referred to as the brine phase, because it contains

high amounts of dissolved salts. This approach allows for exchange of the components CO_2 and water between the phases.

- Pure CO_2 fluid properties are taken into account as functions of temperature and pressure for sub- and supercritical conditions. Brine fluid properties are considered as functions of temperature, pressure, salinity, and the amount of dissolved CO_2.

- The dissolution of CO_2 in the brine phase is taken into account depending on temperature, pressure, and salinity. Dissolved water in the CO_2-rich phase can also be taken into account by the model. It is neglected in the simulations, however, because the change of CO_2 fluid properties due to dissolved water is not considered.

- The rock matrix is taken into account via the porosity and permeability of the porous medium.

- The interactions between the fluids and the porous medium are considered using capillary pressures and relative permeabilities as functions of the fluid saturations.

- Two mass balance equations for the components are formulated. On the assumption of local thermal equilibrium, one energy balance equation is used to describe the heat transport within the fluids and the porous medium. The flow and transport processes taken into account by the model are advection, buoyancy, and diffusion in the brine phase.

- The BOX-method is applied for the spatial discretization of the equations of the mathematical model. A fully implicit Euler scheme is used for the time discretization.

- A Newton-Raphson algorithm is applied to handle the non-linearities of the system of the discretized equations.

Simulation results: The model is applied to three examples to demonstrate its capabilities. The principle studies are set up to study the flow and transport of CO_2 in the subsurface on different time scales and addressing different phenomena. The main insights gained from the simulations are summarized below:

- The carbon dioxide migration in the subsurface is driven by pressure gradients and buoyancy forces when considering short periods of months and years. The density of CO_2 is lower than that of brine, therefore, it flows upwards. The geological properties of the storage formation strongly influence the plume evolution of the carbon dioxide. When propagating in the subsurface, the CO_2 leaves behind a trace of the carbon

dioxide phase at residual saturation (residual trapping). This trapping mechanism plays an important role for the long-term storage.

- The CO_2 plume stops propagating in the storage formation when residual carbon dioxide saturation is reached. The CO_2 can then only be displaced by dissolution in the brine phase and diffusive transport or transport with the brine phase.

  An important effect is the increasing brine density as a result of dissolved CO_2. This causes the CO_2-saturated brine to sink downwards as its density is higher than the density of brine without CO_2. The displacement process of low-density brine by sinking high-density brine occurs in flow fingers, because initially an instable layering can be observed.

- Expansion and evaporation of CO_2 in the storage formation can cause non-isothermal effects, namely a cooling of the system. The cooling effects observed in the simulations in this work are rather small. However, when other subsurface conditions are considered they might be more important.

Further research work: As a follow-up to this study, many things remain to be done as research continues in the field of CO_2 sequestration. At this point, only the research areas related to the modeling are mentioned.

- Dissolved water in the CO_2 phase and its effect on the fluid properties of carbon dioxide has to be included in order to improve the model. Furthermore, other flue gas constituents, e.g. H_2S, NO_x, should be included, because it is unlikely that pure CO_2 will be injected into the storage formation.

- Non-isothermal effects are to be investigated for other model scenarios, especially for the case in which CO_2 leaks from the storage reservoir and migrates up to the surface of the earth. Depending on flow rates along the leakage paths and the duration of the CO_2 migration, significant cooling effects might occur.

- Realistic capillary pressure-saturation relationships for the system CO_2-brine have to be found and implemented in the models. In this context, it is important to study the entry behavior of carbon dioxide into the cap-rock.

- Realistic relative permeability-saturation relationships for the system CO_2-brine have not been available in past years. Recent experimental results have to be implemented in the models to study their influence on the simulation results (BENNION & BACHU (2005) [19]). An important issue here is the consideration of realistic residual CO_2 saturations.

- CO_2 viscosity is significantly lower than brine viscosity. Therefore, viscous fingering can be expected when carbon dioxide is injected into a brine-saturated formation. The forming of CO_2 fingers and the influence on the plume propagation in the subsurface are to be investigated.

- Several technical aspects have to be addressed before large-scale applications of the model presented here can be realized. One important issue in this context is an improved grid generation in order to enable the conversion of a geological model into a grid which can be used by the numerical code. Furthermore, parallelization of the simulation program is a feature that has to be used intensively.

The model presented in this study contributes to the basic understanding of how CO_2 sequestration in geological formations works. Beside the principle examples introduced in Chapter 5, the model can be applied to real storage formations and provide considerable information about the feasibility of this technology (e.g. injectivity of a storage formation, maximum injection pressures at given conditions etc.). Even though a great deal of work remains to be done until the processes occurring during CO_2 sequestration are completely understood, this study gives a comprehensive basis.

Bibliography

[1] CO2SINK - In-Situ R&D Laboratory for Geological Storage of CO_2,
http://www.co2sink.org/.

[2] GESTCO - Geological Storage of CO_2: Assessing European Potential for Geological
Storage of CO_2 from Fossil Fuel Combustion,
http://www.eurogeosurveys.org/projects/GestcoWeb/index.html.

[3] NASCENT - Natural Analogues for the Storage of CO_2 in the Geological Environment,
http://www.bgs.ac.uk/nascent/home.html.

[4] SACS - Saline Aquifer CO_2 Storage,
http://www.iku.sintef.no/projects/IK23430000/.

[5] The Sleipner Project,
http://www.statoil.com/STATOILCOM/SVG00990.NSF/web/sleipneren?opendocument.

[6] Weyburn CO_2 EOR-Project,
http://www.co2captureandstorage.info/project_specific.php4?project_id=97.

[7] Adams, J. and Bachu, S. Equations of state for basin geofluids: algorithm review and
intercomparison for brines. *Geofluids*, 2:257–271, 2002.

[8] Adrian, T., Wendland, M., Hasse, H., and Maurer, G. High-pressure multiphase
behaviour of ternary systems carbon dioxide-water-polar solvent: review and modeling
with the Peng-Robinson equation of state. *Journal of Supercritical Fluids*, 12:185–221,
1998.

[9] Agustsson, H. and Grinestaff, G. A Study of IOR by CO_2 Injection in the Gullfaks
Field, Offshore Norway. *Society of Petroleum Engineers*, SPE 89338, 2003.

[10] Atkins, P. *Physikalische Chemie.* VCH Verlagsgesellschaft, 2001.

[11] Aziz, K. and Settari, A. *Petroleum Reservoir Simulation.* Elsevier Applied Science, 1979.

[12] Baehr, H. D. and Stephan, K. *Wärme- und Stoffübertragung.* Springer Verlag, 1998.

[13] Bastian, P. Numerical Computation of Multiphase Flows in Porous Media. Habilitation, Christian-Albrechts-Universität Kiel, 1999.

[14] Bastian, P. and Helmig, R. Efficient Fully-Coupled Solution Techniques for Two Phase Flow in Porous Media. Parallel Multigrid Solution and Large Scale Computations. *Adv. Water Resour.*, 23:199–216, 1999.

[15] Bastian, P., Birken, K., Johannsen, K., Lang, S., Eckstein, K., Neuss, N., Rentz-Reichert, H., and Wieners, C. UG - A Flexible Software Toolbox for Solving Partial Differential Equations. Computing and Visualization in Science, 1(1), S. 27-40, 1997.

[16] Battistelli, A., Calore, C., and Pruess, K. The Simulator TOUGH2/EWASG for Modelling Geothermal Reservoirs with Brines and Non-condensible Gas. *Geothermics*, 26,4:437–464, 1997.

[17] Batzle, M. and Wang, Z. Seismic Properties of Pore Fluids. *Geophysics*, 57:1396–1408, 1992.

[18] Bear, J. *Dynamics of Fluids in Porous Media.* Elsevier, New York, 1972.

[19] Bennion, B. and Bachu, S. Relative Permeability Characteristics for Supercritical CO_2 Displacing Water in a Variety of Potential Sequestration Zones in the Western Canada Sedimentary Basin. *Society of Petroleum Engineers*, SPE 95547, 2005.

[20] Brooks, A. N. and Corey, A. T. Hydraulic Properties of Porous Media. In *Hydrol. Pap.* Fort Collins, Colorado State University, 1964.

[21] Burdine, N. Relative Permeability Calculations from Pore-Size Distribution Data. Research report, Petroleum Transactions, AIME, 1953.

[22] Celia, M. and Binning, P. A Mass Conservative Numerical Solution for Two-Phase Flow in Porous Media With Application to Unsaturated Flow. *Water Resources Research*, 28:2819–2828, 1992.

[23] Celia, M. and Gray, G. *Numerical Methods for Differential Equations.* Prentice Hall, 1992.

[24] Christensen, N. and Holloway, S. Geological Storage of CO_2 from Combustion of Fossil Fuel. Research report, European Union Fifth Framework Programme for Research & Development, Project No. ENK6-CT-1999-00010, Summary Report, 2003.

[25] Chung, T. *Computational Fluid Dynamics*. Cambridge University Press, 2002.

[26] Cirpka, O. A. and Kitanidis, P. K. Characterization of mixing and dilution in heterogeneous aquifers by means of local temporal moments. *Water Resources Research*, 36(5):1221–1236, 2000.

[27] Class, H. *Theorie und numerische Modellierung nichtisothermer Mehrphasenprozesse in NAPL-kontaminierten porösen Medien*. Dissertation, Technische Universität Braunschweig, 2000. Mitteilungsheft Nr. 105, Institut für Wasserbau, Universität Stuttgart.

[28] Class, H. and Helmig, R. Numerical simulation of non-isothermal multiphase multicomponent processes in porous media. - 2. applications for the injection of steam and air. *Adv. Water Resour.*, 25:551–564, 2002.

[29] Class, H., Helmig, R., and Bastian, P. Numerical simulation of non-isothermal multiphase multicomponent processes in porous media. - 1. an efficient solution technique. *Adv. Water Resour.*, 25:533–550, 2002.

[30] Clauser, C. *Numerical Simulation of Reactive Flow in Hot Aquifers, SHEMAT and Processing SHEMAT*. Springer, 2003.

[31] Dahle, H., Celia, M., and Hassanizadeh, S. Bundle of tubes model for calculating dynamic effects in the capillary pressure-saturation relationship. In Das, D. and Hassanizadeh, S., Ed., *Upscaling Multiphase Flow in Porous Media*, S. 5–22. Springer, 2005.

[32] Daubert, T. E. and Danner, R. P. *Physical and thermodynamic properties of pure chemicals: data compilation*. Design Institute for Physical Property Data, 1989.

[33] Duan, Z. and Sun, R. An Improved Model Calculating CO_2 Solubility in Pure Water and Aqueous NaCl Solutions from 273 to 533 K and from 0 to 2000 bar. *Chem. Geol.*, 193:257–271, 2003.

[34] Ebigbo, A. Thermal Effects of Carbon Dioxide Sequestration in the Subsurface. Diplomarbeit, Institut für Wasserbau, Universität Stuttgart, 2005.

[35] Ennis-King, J. and Paterson, L. Role of Convective Mixing in the Long-Term Storage of Carbon Dioxide in Deep Saline Aquifers. *Society of Petroleum Engineers*, SPE 84344, 2003.

[36] Faires, J. D. and Burden, R. L. *Numerische Methoden*. Spektrum Akademischer Verlag, 1994.

[37] Falta, R., Pruess, K., Javandel, I., and Witherspoon, P. Numerical Modeling of Steam Injection for the Removal of Nonaqueous Phase Liquids From the Subsurface. 1. Numerical Formulation. *Water Resour. Res.*, 28,2:433–449, 1992.

[38] Falta, R., Pruess, K., Javandel, I., and Witherspoon, P. Numerical Modeling of Steam Injection for the Removal of Nonaqueous Phase Liquids From the Subsurface. 2. Code Validation and Application. *Water Resour. Res.*, 28,2:451–465, 1992.

[39] Fenghour, A., Wakeham, W., and Vesovic, V. The Viscosity of Carbon Dioxide. *J. Phys. Chem. Ref. Data*, 27(1):31–44, 1998.

[40] Fyfe, W., Price, N., and Thompson, A. *Fluids in the Earth's Crust*. Elsevier Scientific Publication Company, 1978.

[41] Garcia, J. Density of Aqueous Solutions of CO_2. Research report, LBNL Report 49023, Lawrence Berkeley National Laboratory, Berkeley, CA, U.S.A., 2001.

[42] Garcia, J. E. *Fluid Dynamics of Carbon Dioxide Disposal into Saline Aquifers*. Dissertation, Lawrence Berkeley National Laboratory, University of California, 2003.

[43] Gasda, S., Bachu, S., and Celia, M. The Potential for CO2 Leakage from Storage Sites in Geological Media: Analysis of Well Distribution in Mature Sedimentary Basins. *submitted to Environmental Geology*, 2004.

[44] van Genuchten, M. A Closed-Form Equation for Predicting the Hydraulic Conductivity of Unsaturated Soils. *Soil Sci. Soc. Am. J.*, 44:892–898, 1980.

[45] Gmehling, J. and Kolbe, B. *Thermodynamik*. VCH Verlag Weinheim, 1992.

[46] Hackbusch, W. *Multi-Grid Methods and Applications*. Springer Verlag Berlin, 1985.

[47] Hattenbach, R., Wilson, M., and Brown, K. Capture of Carbon Dioxide from Coal Combustion and its Utilization for Enhanced Oil Recovery. In Eliasson, B., Riemer, P., and Wokaun, A., Ed., *Greenhouse Gas Control Technologies*, Interlaken, Switzerland, August 30-October 2, 1998. 4th International Conference on Greenhouse Gas Control Technologies (GHGT-4).

[48] Hazen, A. Some Physical Properties of Sands and Gravels with Special Reference to their Use in Infiltration. *Ann. Rep. State Board of Health Mass.*, 24:541–556, 1892.

[49] Helmig, R. *Theorie und Numerik der Mehrphasenströmungen in geklüftet-porösen Medien.* Dissertation, Institut für Strömungsmechanik und Elektronisches Rechnen im Bauwesen, Universität Hannover, Bericht Nr. 34, 1993.

[50] Helmig, R. and Class, H. *Grundlagen der Hydromechanik.* Shaker Verlag Aachen, 2005.

[51] Helmig, R., Class, H., Huber, R., Sheta, H., Ewing, R., Hinkelmann, R., Jakobs, H., and Bastian, P. Architecture of the Modular Program System MUFTE-UG for Simulating Multiphase Flow and Transport Processes in Heterogeneous Porous Media. *Mathematische Geologie*, 2:123–131, 1998.

[52] Helmig, R. *Multiphase Flow and Transport Processes in the Subsurface.* Springer, 1997.

[53] Helmig, Rainer und Huber, R. Comparison of galerkin-type discretization techniques for two-phase flow in heterogeneous porous media. Forschungsbericht, Universität Stuttgart, SFB 404, Bericht 96/11, 1996.

[54] Houghton, J. *Global Warming.* Cambridge University Press, 1997.

[55] Huber, R. and Helmig, R. Multiphase Flow in Heterogeneous Porous Media: A Classical Finite Element Method versus an Implicit Pressure - Explicit Saturation-based Mixed Finite Element - Finite Volume Approach. *International Journal for Numerical Methods in Fluids*, 29:899–920, 1999.

[56] Huber, R. *Immiscible and Compositional Multiphase Flow and Transport in Heterogeneous Porous Media: Modelling Formulation, and Numerical Simulation.* Dissertation, Technische Universität Braunschweig, Institut für Computeranwendungen im Bauingenieurwesen, 1999.

[57] Huron, M.-J. and Vidal, J. New Mixing Rules in Simple Equations of State for Representing Vapour-Liquid Equilibria of Strongly Non-Ideal Mixtures. *Fluid Phase Equil.*, 3:255–271, 1979.

[58] IAPWS (The International Association for the Properties of Water and Steam). Release on the IAPWS Industrial Formulation 1997 for the Thermodynamic Properties of Water and Steam. http://www.iapws.org/, 1997.

[59] Intergovernmental Panel on Climate Change (IPCC). Climate Change 2001: The Scientific Basis. Cambridge University Press, http://www.grida.no/climate/ipcc_tar/wg1/index.htm, 2001.

[60] Jakobs, H. *Simulation nicht-isothermer Gas-Wasser-Prozesse in komplexen Kluft-Matrix-Systemen*. Dissertation, Institut für Wasserbau, Universität Stuttgart, 2004.

[61] Jessen, K., Sam-Olibale, L., Kovscek, A., and Orr, F. Increasing CO_2 Storage in Oil Recovery. First National Conference on Carbon Sequestration, Washington, DC, May 14-17, 2001.

[62] Kaszuba, J., Janecky, D., and Snow, M. Carbon dioxide reaction processes in a model brine aquifer at 200°C and 200 bars: implication for geologic sequestration of carbon. *Applied Geochemistry*, 18:1065–1080, 2003.

[63] Keeling, C. and Whorf, T. Atmospheric CO_2 records from sites in the SIO air sampling network. In Trends: A Compendium of Data on Global Change. Carbon Dioxide Information Analysis Center, Oak Ridge National Laboratory, U.S. Department of Energy, Oak Ridge, Tenn., U.S.A. http://cdiac.esd.ornl.gov/trends/co2/sio-mlo.htm, 2005.

[64] Kinzelbach, W. *Numerische Methoden zur Modellierung des Transports von Schadstoffen im Grundwasser*. R. Oldenbourg Verlag, München, Wien, 1987.

[65] Lenhard, R., Parker, J., and Mishra, S. On the Correspondence between Brooks-Corey and Van Genuchten models. *Journal of Irrigation and Drainage Engineering*, 115(4):744–751, 1989.

[66] Lindeberg, E. Escape of CO_2 from Aquifers. *Energy Convers. Mgmt.*, 38:235–240, 1997.

[67] Lindeberg, E. and Wessel-Berg, D. Vertical Convection in an Aquifer Column under a Gas Cap of CO_2. *Energy and Conversion Managment*, 38:229–234, 1997.

[68] Lüdecke, C. and Lüdecke, D. *Thermodynamik*. Springer, 2000.

[69] Mader, D. Molekulardynamische Simulationen nanoskaliger Strömungsvorgänge. Diplomarbeit, Institut für Technische Thermodynamik und Thermische Verfahrenstechnik, Universität Stuttgart, 2004.

[70] Manthey, S., Hassanizadeh, S., and Helmig, R. Macro-scale dynamic effects in homogeneous and heterogenous porous media. *Transport in Porous Media*, 58:121–145, 2005.

[71] Meister, A. *Numerik linearer Gleichungssysteme.* Vieweg Verlag Braunschweig, 1999.

[72] Melhem, G. A., Saini, R., and Goodwin, B. M. A Modified Peng-Robinson Equation of State. *Fluid Phase Equil.*, 47:189–237, 1989.

[73] Meschede, D. *Gerthsen Physik.* Springer, 2004.

[74] Michaelides, E. Thermodynamic properties of geothermal fluids. *Geothermal Resources Council Transactions*, 5:361–364, 1981.

[75] Millington, R. and Quirk, J. Permeability of Porous Solids. *Trans. Faraday Soc.*, 57:1200–1207, 1961.

[76] Mualem, Y. A New Model for Predicting the Hydraulic Conductivity of Unsaturated Porous Media. *Water Resour. Res.*, 12:513–522, 1976.

[77] Nordbotten, J., Celia, M., and Bachu, S. Analytical Solutions for Leakage Rates through Abandoned Wells. *Water Resources Research*, W04204, 2004.

[78] Nordbotten, J., Celia, M., and Bachu, S. Injection and Storage of CO_2 in Deep Saline Aquifers: Analytical Solution for CO_2 Plume Evolution During Injection. *Transport in Porous Media*, 58(3):339–360, 2005.

[79] Nordbotten, J., Celia, M., Bachu, S., and Dahle, H. Semi-Analytical Solution for CO_2 Leakage through an Abandoned Well. *Environmental Science and Technology*, 39(2):602–611, 2005.

[80] Oldenburg, C. and Benson, S. CO_2 Injection for Enhanced Gas Production and Carbon Sequestration. *Society of Petroleum Engineers*, SPE 74367, 2002.

[81] Panday, S., Forsyth, P., Falta, R., Wu, Y., and Huyakorn, P. Considerations for robust compositional simulations of subsurface nonaqueous phase liquid contamination and remediation. *Water Resour. Res.*, 31(5):1273–1289, 1995.

[82] Peaceman, D. *Fundamentals of Numerical Reservoir Engineering.* Elsevier Applied Science, 1977.

[83] Peng, D.-Y. and Robinson, D. B. A New Two-Constant Equation of State. *Ind. Eng. Chem. Fundam.*, 15:59–64, 1976.

[84] Pfennig, A. *Thermodynamik der Gemische.* Springer, 2004.

[85] Poling, B., Prausnitz, J., and O'Connel, J. *The Properties of Gases and Liquids.* McGraw-Hill, Inc., 2001.

[86] Pruess, K. Thermal Effects During CO2 Leakage from a Geologic Storage Reservoir. *Lawrence Berkeley National Laboratory Report LBNL-55913*, 2004.

[87] Pruess, K., Bielinski, A., Ennis-King, J., Fabriol, R., Le Gallo, Y., Garcia, J., Jessen, K., Kovscek, T., Law, D.-S., Lichtner, P., Oldenburg, C., Pawar, R., Rutqvist, J., Steefel, C., Travis, B., Tsang, C.-F., White, S., and Xu, T. Code Intercomparison Builds Confidence in Numerical Models for Geologic Disposal of CO2. In *Gale, J. and Kaya, Y. (Editors): GHGT-6 Conference Proceedings: Greenhouse Gas Control Technologies*, S. 463–470, 2003.

[88] Pruess, K. and Garcia, J. Multiphase Flow Dynamics during CO2 Injection into Saline Aquifers. *Environmental Geology*, 42:282–295, 2002.

[89] Scheffer, F. and Schachtschabel, P. *Lehrbuch der Bodenkunde.* Enke, 1992.

[90] Shaughnessy, E. J., Katz, I. M., and Schaffer, J. P. *Introduction to Fluid Mechanics.* Oxford University Press, 2005.

[91] She, H. and Sleep, B. The Effect of Temperature on Capillary Pressure-Saturation Relationships for air-water and perchloroethylene-water systems. *Water Resour. Res.*, 34(10):2587–2597, 1998.

[92] Sheta, H. *Simulation von Mehrphasenvorgängen in porösen Medien unter Einbeziehung von Hysterese-Effekten.* Dissertation, Universität Stuttgart, 1999.

[93] Society of Petroleum Engineers (SPE). CO_2 Flooding. SPE Reprint Series, 1999.

[94] Society of Petroleum Engineers (SPE). Practical Aspects of CO_2 Flooding. SPE Monograph Series, 2002.

[95] Somerton, W., El-Shaarani, A., and Mobarak, S. High Temperature Behaviour of Rocks Associated with Geothermal Type Reservoirs. *Society of Petroleum Engineers*, Paper SPE-4897 presented at 48th Annual California Regional Meeting of the Society of Petroleum Engineers, 1974.

[96] Span, R. and Wagner, W. A New Equation of State for Carbon Dioxide Covering the Fluid Region from the Triple–Point Temperature to 1100 K at Pressures up to 800 MPa. *J. Phys. Chem. Ref. Data*, 25(6):1509–1596, 1996.

[97] Spycher, N., Pruess, K., and Ennis-King, J. CO_2-H_2O Mixtures in the Geological Sequestration of CO_2. I. Assessment and Calculation of Mutual Solubilities from 12 to 100°C and Up to 600 Bar. *Geochim. et Cosmochim. Acta*, 67(16):3015–3031, 2003.

[98] Streit, J. and Hillis, R. Estimating Fault Stability and Sustainable Fluid Pressures for Underground Storage of CO_2 in Porous Rock. *Energy*, 29:1445–1456, 2004.

[99] Umweltbundesamt. *Daten zur Umwelt*. Erich Schmidt Verlag, 2001.

[100] Van Der Waals, J. D. *Over de continuiteit van den gas- en vloeistoftoestand*. Dissertation, Sijthoff, Leiden, 1873.

[101] Wagner, W. and Pruss, A. The IAPWS Formulation 1995 for the Thermodynamic Properties of Ordinary Water Substance for General and Scientific Use. *Jour. Phys. Chem. Ref. Data*, 31(2):387–535, 2002002.

[102] Watson, M., Zwingmann, N., Lemon, N., and Tingate, P. Onshore Otway Basin Carbon Dioxide Accumulations: CO_2-induced Diagenesis in Natural Analogous for Underground Storage of Greenhouse Gas. *The APPEA Journal*, S. 637–653, 2003.

[103] Wendland, M. *Hochdruckmehrphasengleichgewichte in ternären Gemischen aus Kohlendioxid, Wasser und einem organischen Lösungsmittel*. Dissertation, Universität Kaiserslautern, 1994.

[104] Xu, T., Apps, J., and Pruess, K. Reactive Geochemical Transport Simulation to Study Mineral Trapping for CO_2 Disposal in Deep Saline Arenaceous Aquifers. *Lawrence Berkeley National Laboratory Report LBNL–50089*, 2002.

Appendix A

Salinities

There are several possibilities to express the salt content in brine. Some of them are listed here:

- **Molality:** molality is given by the ratio of the number of moles of salt n_{salt} and the mass of the solvent water m_w:

$$\text{molality: } \frac{n_{\text{salt}}}{m_w} \qquad [\text{mol salt/kg solvent}] \tag{A.1}$$

- **Mass fraction** S: the mass fraction of salt in brine m_s relates the salt mass to the total mass of the solution:

$$S = \frac{m_s}{m_s + m_w} \qquad [\text{kg salt/kg solution}] \tag{A.2}$$

- **Salinity in per mill** s:

$$s = \frac{m_s}{m_w} \cdot 1000 \qquad [\text{kg salt/kg solvent} \cdot 1000] = [\text{‰}] \tag{A.3}$$

- **Concentration** c: the concentration is defined as the ratio between the salt mass and the volume of the solution:

$$c = \frac{m_s}{V_{\text{solution}}} \qquad [\text{kg salt/m}^3 \text{ solution}] \tag{A.4}$$

Appendix B

Peng-Robinson cubic equation of state

B.1   Thermal behavior of pure CO_2

As shown in Section 2.1.5 the cubic equation of state suggested by PENG & ROBINSON (1976) [83] is given by

$$Z = \frac{pv}{RT} = \frac{v}{v-b} - \frac{a(T)v}{RT[v(v+b)+b(v-b)]} \tag{B.1}$$

or

$$p = \frac{RT}{v-b} - \frac{a(T)}{v(v+b)+b(v-b)}. \tag{B.2}$$

The parameters a and b are defined via critical temperature and pressure of the substance:

$$a = 0.45724 \frac{R^2 T_{\mathrm{crit}}^2}{p_{\mathrm{crit}}} \tag{B.3}$$

$$b = 0.0778 \frac{R T_{\mathrm{crit}}}{p_{\mathrm{crit}}} \tag{B.4}$$

where b is the minimum volume that one mole of CO_2 molecules can occupy and accounts for the repulsive molecular forces. The attractive forces between the molecules is taken into account by parameter a. It is described as a function of temperature considering $\alpha(T)$ and the acentric factor ω:

$$a(T) = a\,\alpha(T) \tag{B.5}$$

$$\alpha(T) = [1 + (0.37464 + 1.54226\,\omega - 0.26992\,\omega^2)(1 - T_r^{0.5})]^2 \tag{B.6}$$

The acentric factor is defined by

$$\omega = -1.0 - \log(p_{\mathrm{sat}}(0.7 \cdot T_{\mathrm{crit}})/P_{\mathrm{crit}}) \tag{B.7}$$

106

where p_{sat} is the vapor pressure of the substance. The acentric factor ω is a third parameter that makes the equation of state better applicable to non-spherical and polar molecules (cf. e.g. GMEHLING & KOLBE [45]).

Following the investigations of WENDLAND (1994) [103] for the binary system carbon dioxide-water, a modified version of the Peng-Robinson equation after MELHEM ET AL. (1989) [72] is used in this work. In contrast to other approaches, they have the advantage that they consider an extrapolation of α to supercritical temperatures. It is proposed

$$\alpha(T) = \exp\left[m(1 - T_r) + n(1 - \sqrt{T_r})^2\right] \tag{B.8}$$

where m and n are two parameters specific to the substance. These parameters replace the acentric factor ω of the original equation and are available for several pure substances.

Following the application of the parameters shown in Table B.1 to the Peng-Robinson cubic equation of state modified by Melhem et al., it is possible to obtain the thermal behavior of CO_2. The results for the behavior of gaseous, liquid, and supercritical CO_2 are depicted in Figure 2.3 (page 16).

Table B.1: Parameters for pure CO_2 using the modified Peng-Robinson cubic equation of state after MELHEM ET AL. (1989) [72].

p_{crit}	73.8 bar
T_{crit}	304.2 K
m	0.6877
n	0.3813

B.2 Thermal behavior of the mixture CO_2 + water

In Section 2.1.5, a linear and a quadratic mixing rule are used to find the Van-der-Waals parameters of a mixture (equations (2.5) and (2.6)). PENG & ROBINSON (1976) [83] extended this approach and obtain the following equations:

$$a_{mix} = \sum_{i=1}^{N}\sum_{j=1}^{N} x_i x_j \sqrt{a_i a_j}(1 - K_{i,j}) \tag{B.9}$$

$$b_{mix} = \sum_{i=1}^{N} x_i b_i. \tag{B.10}$$

In these equations, Peng and Robinson introduce the binary interaction parameter $K_{i,j}$ for the computation of a. This parameter accounts for unlike molecular interactions, so that $K_{i,j}(i = j) = 0$ and $K_{i,j}(i \neq j) = K_{j,i}$. Therefore, a binary system has one interaction parameter.

To describe the phase equilibria of the two-component system CO_2-water, the suggestions given by ADRIAN ET AL. (1998) [8] and WENDLAND (1994) [103] are used. As described above (Appendix B.1) the modified Peng-Robinson equation of state after MELHEM ET AL. (1989) [72] is applied. Furthermore, a mixing rule proposed by HURON & VIDAL (1979) [57] is considered, because it gives a very good representation of experimental values especially of dissolved CO_2 in the water phase. The Huron-Vidal mixing rule requires two parameters $k_{1,2}$ and $l_{1,2}$, which are given in Table B.2. For more detailed studies of the mixing rules, the reader is referred to the work of WENDLAND (1994) [103] or to the original publication of HURON & VIDAL (1979) [57].

Table B.2: Parameters for the Peng-Robinson cubic equation of state for the system CO_2-water (after WENDLAND (1994) [103]).

CO_2	p_{crit}	73.8 bar
	T_{crit}	304.2 K
	m	0.6877
	n	0.3813
water	p_{crit}	220.5 bar
	T_{crit}	647.3 K
	m	0.8893
	n	0.0151
mixture	$k_{1,2} = k_{2,1}$	0.2333
	$l_{1,2} = l_{2,1}$	0.0814

In Section 2.1.5, Figure 2.4 shows qualitatively the results of this cubic equation of state for the system CO_2-water in a pressure-composition diagram. Figures 3.2 and 3.5 (Section 3.1.2) present solubilities depending on pressure as a result of the application of this equation of state.

Appendix C

Relevant transport processes during CO$_2$ sequestration

This section of the Appendix will give some examples to improve the understanding of the flow processes taking place in the subsurface during CO$_2$ sequestration.

C.1 Advection

To get an idea of the CO$_2$ flow velocities that occur in the subsurface due to advection a simple approach that is based on the principle of continuity of mass is chosen. The flow velocity is equal to the ratio of the volumetric injection rate Q_{vol} and the cross-sectional area of the flow A:

$$\mathbf{v} = \frac{Q_{\mathrm{vol}}}{A}. \tag{C.1}$$

On the assumption of a vertical line source and neglecting buoyancy forces the plume will develop around the injection line in a cylindrical shape. Then, the cross-sectional area of the surface of the CO$_2$ plume can be estimated to be

$$A = 2\pi r \cdot m \cdot S_{\mathrm{CO2}} \cdot \phi. \tag{C.2}$$

$2\pi r$ is the perimeter of the plume at a distance r from the injection well, m the thickness of the storage formation, S_{CO2} the average CO$_2$ saturation within the plume and ϕ the porosity.

As an example, the following values are inserted; the results are shown for various distances from the injection well in Table C.1.

$p_{\mathrm{init}} \quad = 100\,\mathrm{bar} \qquad \text{(initial injection pressure)},$

T_{init} $= 37\,°\text{C}$ (initial formation temperature),

ϱ_{CO2} $= 683\,\text{kg/m}^3$ (CO_2 density at initial conditions),

Q_{mass} $= 100\,\text{kg/s}$ (CO_2 mass injection rate),

Q_{vol} $= 0.1464\,\text{m}^3/\text{s}$ (CO_2 volumetric injection rate),

m $= 100\,\text{m}$,

S_{CO2} $= 0.2$,

ϕ $= 0.25$.

Table C.1: Values for advective flow at various distances r from the injection well.

distance from injection well [m]	flow velocity [m/s]	flow velocity [m/d]
1	$4.66 \cdot 10^{-3}$	403
100	$4.66 \cdot 10^{-5}$	4.03
1000	$4.66 \cdot 10^{-6}$	0.403

Note that these velocities already refer to the seepage velocity (cf. Section 2.6.1) as porosity is taken into account.

C.2   Buoyancy

This example refers to CO_2 rising in formation brine due to buoyancy forces. The multi-phase version of Darcy's Law is

$$\mathbf{v}_\alpha = -\frac{k_{r\alpha}}{\mu_\alpha}\mathbf{K}(\nabla p_\alpha - \varrho_\alpha \mathbf{g}). \tag{C.3}$$

As only forces caused by gravity which only acts in the z-direction are to be considered, the pressure gradient in x- and y-direction is assumed to be zero: $\frac{\partial p}{\partial x} = \frac{\partial p}{\partial y} = 0$. The pressure gradient in z-direction can then be expressed by

$$\nabla p = \frac{\partial p}{\partial z} = \varrho_w g \tag{C.4}$$

where ϱ_w is the density of the formation fluid water (or brine) and g the gravity constant. This assumption and the application of equation (C.3) to the CO_2 flow velocity yields

$$\mathbf{v}_{\text{CO2}} = -\frac{k_{r\text{CO2}}}{\mu_{\text{CO2}}}\mathbf{K}(\varrho_w - \varrho_{\text{CO2}})\mathbf{g}. \tag{C.5}$$

To estimate the resulting velocity the following numbers are inserted:

$$
\begin{aligned}
k_{\mathrm{rCO2}} \quad &= 0.2, \\
\mu_{\mathrm{CO2}} \quad &= 5.0 \cdot 10^{-5}\,\mathrm{Pa\ s}, \\
K \quad &= 1.0 \cdot 10^{-12}\,\mathrm{m^2}, \\
\varrho_{\mathrm{w}} - \varrho_{\mathrm{CO2}} \quad &= 400\,\mathrm{kg/m^3}\ \text{(supercritical CO$_2$ and water)}, \\
g \quad &= 9.81\,\mathrm{m/s^2}.
\end{aligned}
$$

This results in a CO_2 flow velocity of

$$
\mathbf{v}_{\mathrm{CO2}} = 1.6 \cdot 10^{-5}\,\mathrm{m/s}. \tag{C.6}
$$

Changing the density difference to the one between gaseous CO_2 and water $(\varrho_{\mathrm{w}} - \varrho_{\mathrm{CO2}} = 1000\,\mathrm{kg/m^3})$, CO_2 flow velocity can go up to

$$
\mathbf{v}_{\mathrm{CO2}} = 3.9 \cdot 10^{-5}\,\mathrm{m/s}. \tag{C.7}
$$

This velocity does not represent the actual particle speed (cf. Section 2.6.1). The seepage velocity has to be computed resulting in an even faster fluid movement and earlier arrival times.

C.3 Diffusion

The diffusion coefficient D can be estimated as the square of a typical transportation length l divided by a typical time t

$$
D = \frac{l^2}{t}. \tag{C.8}
$$

Considering a constant CO_2 source (e.g. a CO_2 plume that is trapped underneath a cap-rock) at a depth of $1000\,\mathrm{m}$ and a diffusion coefficient of $D = 2.0 \cdot 10^{-9}\,\mathrm{m^2/s}$. Then the time for purely diffusive transport to the surface of the earth is computed by

$$
t = \frac{l^2}{D} = \frac{(1000\,\mathrm{m})^2}{2.0 \cdot 10^{-9}\,\mathrm{m^2/s}} = 5 \cdot 10^{14}\,\mathrm{s} \approx 16\,\mathrm{Mio\ a}. \tag{C.9}
$$

Appendix D

Details of simulation setup

This sections gives details of the model setups that were used to conduct the simulations described in Chapter 5. The parameters, boundary and initial conditions are listed in a table for each problem.

- **CO$_2$ plume evolution (Section 5.2):** Tab. D.1 (page 113).

- **Long-term effects (Section 5.3):** Tab. D.2 (page 114).

- **Non-isothermal effects (Section 5.4):** Tab. D.3 (page 115).

Table D.1: CO_2 plume evolution: model setup.

Parameters		
Parameter	storage reservoir	low-permeable layers
porosity	0.2	0.2
permeability $\mathbf{K}$	$1.0 \cdot 10^{-12} \, \text{m}^2$	$1.0 \cdot 10^{-14} \, \text{m}^2$
residual water saturation	0.2	0.2
residual CO_2 saturation	0.05	0.05
p_c-S_w relationship	Brooks & Corey	Brooks & Corey
entry pressure	$1000 \, \text{Pa}$	$10000 \, \text{Pa}$
λ	2.0	2.0
salinity	0.25	0.25
diffusion coefficient $\mathbf{D}_b^{\text{CO2}}$	$2.0 \cdot 10^{-9} \, \text{m}^2/\text{s}$	$2.0 \cdot 10^{-9} \, \text{m}^2/\text{s}$

Boundary conditions					
boundary	type	variable	value	unit	comment
far side	Dirichlet	X_b^{CO2}	$1.0 \cdot 10^{-9}$		
	Dirichlet	p_{CO2}	$p_\text{atm} + 8.0 \cdot 10^6 + \varrho_\text{b} g z$	Pa	hydrostatic pressure
	Dirichlet	T	$34 + 0.03 \cdot z$	°C	geothermal gradient
left, right,	Neumann	$\dot{q}_\text{w}$	0.0	kg/m²s	no-flow (water)
top, bottom	Neumann	$\dot{q}_{\text{CO2}}$	0.0	kg/m²s	no-flow (CO_2)
	Neumann	$\dot{q}_\text{h}$	0.0	J/m²s	no-flow (heat)
injection	Neumann	$\dot{q}_\text{w}$	0.0	kg/(m² s)	no-flow (water)
	Neumann	$\dot{q}_{\text{CO2}}$	0.02	kg/(m² s)	if (time < 1 year)
	Neumann	$\dot{q}_\text{h}$	-3560.0	J/(m² s)	if (time < 1 year)

Initial conditions					
boundary	variable		value	unit	comment
initial condition	S_w		1.0		full saturation
	X_b^{CO2}		$1.0 \cdot 10^{-9}$		
	p_{CO2}		$p_\text{atm} + 8.0 \cdot 10^6 + \varrho_\text{b} g z$	Pa	hydrostatic pressure
	T		$34 + 0.03 \cdot z$	°C	geothermal gradient
	phase state		water phase		

Table D.2: Long-term effects: model setup.

Parameters		
Parameter	$\Omega 1$	$\Omega 2$
porosity	0.2	0.1
permeability $\mathbf{K}$	$1.0 \cdot 10^{-12}\,\mathrm{m}^2$	$1.0 \cdot 10^{-14}\,\mathrm{m}^2$
residual water saturation	0.2	0.2
residual CO_2 saturation	0.05	0.05
p_c-S_w relationship	Brooks & Corey	Brooks & Corey
entry pressure	$1000\,\mathrm{Pa}$	$10000\,\mathrm{Pa}$
λ	2.0	2.0
salinity	0.25	0.25
diffusion coefficient $\mathbf{D}_b^{CO2}$	$2.0 \cdot 10^{-9}\,\mathrm{m}^2/\mathrm{s}$	$2.0 \cdot 10^{-9}\,\mathrm{m}^2/\mathrm{s}$

Boundary conditions					
boundary	type	variable	value	unit	comment
left, right	Dirichlet	X_b^{CO2}	$1.0 \cdot 10^{-9}$		
	Dirichlet	p_{CO2}	$p_\mathrm{atm} + 5.0 \cdot 10^6 + \varrho_\mathrm{b} g z$	Pa	hydrostatic pressure
	Dirichlet	T	$25 + 0.03 \cdot z$	°C	geothermal gradient
top, bottom	Neumann	$\dot{q}_\mathrm{w}$	0.0	kg/m^{2}s	no-flow (water)
	Neumann	$\dot{q}_{CO2}$	0.0	kg/m^{2}s	no-flow (CO_2)
	Neumann	$\dot{q}_\mathrm{h}$	0.0	J/m^{2}s	no-flow (heat)
injection	Neumann	$\dot{q}_\mathrm{w}$	0.0	kg/m^{2}s	no-flow (water)
	Neumann	$\dot{q}_{CO2}$	0.02	kg/m^{2}s	if (time < 40 days)
	Neumann	$\dot{q}_\mathrm{h}$	-3560.0	J/m^{2}s	if (time < 40 days)

Initial conditions				
boundary	variable	value	unit	comment
initial condition	S_w	1.0		full saturation
	X_b^{CO2}	$1.0 \cdot 10^{-9}$		
	p_{CO2}	$p_\mathrm{atm} + 5.0 \cdot 10^6 + \varrho_\mathrm{b} g z$	Pa	hydrostatic pressure
	T	$25 + 0.03 \cdot z$	°C	geothermal gradient
	phase state	water phase		

Table D.3: Non-isothermal effects: model setup.

Parameters	
Parameter	value in model domain
porosity	0.2
permeability $\mathbf{K}$	$1.0 \cdot 10^{-12}\,\mathrm{m}^2$
residual water saturation	0.2
residual CO_2 saturation	0.05
p_c-S_w relationship	Brooks & Corey
entry pressure	$1000\,\mathrm{Pa}$
λ	2.0
salinity	0.25
diffusion coefficient $\mathbf{D}_b^{CO2}$	$2.0 \cdot 10^{-9}\,\mathrm{m}^2/\mathrm{s}$

Boundary conditions					
boundary	type	variable	value	unit	comment
right	Dirichlet	X_b^{CO2}	$1.0 \cdot 10^{-9}$		
	Dirichlet	p_CO2	$p_\mathrm{atm} + 5.0 \cdot 10^6 + \varrho_\mathrm{b}gz$	Pa	hydrostatic pressure
	Dirichlet	T	37	°C	
bottom	Dirichlet	X_b^{CO2}	$1.0 \cdot 10^{-9}$		
	Dirichlet	p_CO2	$1.09 \cdot 10^7$	Pa	hydrostatic pressure
	Dirichlet	T	37	°C	
left, top	Neumann	$\dot{q}_\mathrm{w}$	0.0	kg/m²s	no-flow (water)
	Neumann	$\dot{q}_\mathrm{CO2}$	0.0	kg/m²s	no-flow (CO_2)
	Neumann	$\dot{q}_\mathrm{h}$	0.0	J/m²s	no-flow (heat)
injection	Neumann	$\dot{q}_\mathrm{w}$	0.0	kg/m²s	no-flow (water)
injection	Neumann	$\dot{q}_\mathrm{CO2}$	0.02	kg/m²s	
injection	T_CO2	Dirichlet	37	°C	

Initial conditions				
boundary	variable	value	unit	comment
initial condition	S_w	1.0		full saturation
initial condition	X_b^{CO2}	$1.0 \cdot 10^{-9}$		
initial condition	p_CO2	$p_\mathrm{atm} + 5.0 \cdot 10^6 + \varrho_\mathrm{b}gz$	Pa	hydrostatic pressure
initial condition	T	37	°C	
initial condition	phase state	water phase		

Lebenslauf Andreas Bielinski

Andreas Bielinski
Alexanderstrasse 29
70184 Stuttgart
Tel.: 0711/685-4667
e-mail: andreas.bielinski@iws.uni-stuttgart.de

Geboren: 11. Januar 1973 in Gehrden

Ausbildung

1979-92	Grundschule und Gymnasium in Burgdorf, Abitur 1992.
1989-90	Ein Jahr als Austauschschüler in den U.S.A.
1995-2001	Studium der Geoökologie an der TU Braunschweig, Diplom 2001.
1992-93	Zivildienst mit behinderten Kindern in der Lebenshilfe Burgdorf.
1993-94	Reise durch Lateinamerika zum Kennenlernen der Kultur und Erlernen der Sprache (10 Monate).

Berufliche Tätigkeit

seit 2001	Wissenschaftlicher Mitarbeiter am Institut für Wasserbau, Lehrstuhl für Hydromechanik und Hydrosystemmodellierung, Universität Stuttgart.